Nanochemistry on Si(100): Surface Biofunctionalization by Amino-containing Bifunctional Molecules, and Shape Control of Copper Core-Shell Nanoparticles

by

Abdullah Radi

A thesis
presented to the University of Waterloo
in fulfillment of the
thesis requirement for the degree of
Master of Science
in
Chemistry

Waterloo, Ontario, Canada, 2009

AUTHOR'S DECLARATION

I herby declare that I am the sole author of this thesis. This is a true copy of the thesis, including my required final version, as accepted by the examiners.
I understand that my thesis may be made electronically available to the public.

Abstract

The present research involves two projects: a surface science study of the room-temperature adsorption and thermal evolution of allylamine and ethanolamine on Si(100)2×1, studied by using temperature-dependent X-ray photoelectron spectroscopy (XPS) and thermal desorption spectrometry (TDS), as well as Density Functional Theory (DFT) calculations; and a materials science study on the shape control of copper nanoparticles (Cu NPs) deposited on H-terminated Si(100) substrate with an extended size regime of 5-400 nm, by using a simple, one-step electrochemical method. The Cu NPs of three primary shapes were characterized with scanning-electron microscopy (SEM), glancing-incidence X-ray diffraction (GIXRD) and XPS.

In the first surface science study, the presence of broad N 1s XPS features at 398.9-399.1 eV, corresponding to N–Si bonds, indicates N–H dissociative adsorption for both allylamine and ethanolamine on Si(100)2×1. For allylamine, the presence of C 1s features at 284.6 eV and 286.2 eV, corresponding to C=C and C−N, respectively, and the absence of the Si−C feature expected at 283.5 eV show that the reactions involving the ethenyl group such as the [2+2] C=C cycloaddition or those producing the [N, C, C] tridentate adstructures do not occur at room temperature. For ethanolamine, the O 1s feature at 533.1 eV indicates the formation of Si−O bond and O−H dissociation, which confirms an [O, N] bidentate adstructure and excludes the N−H and O−H dissociation unidentate structures. These XPS data are consistent with the N−H unidentate, and N−H and O−H double dissociation [O, N] bidentate adstructures for allylamine and ethanolamine, respectively, as predicted by the DFT calculations. TDS and temperature-dependent XPS data further show the desorption of propene and ethylene at 580 K and of acetylene at 700 K for allylamine and the desorption of ethylene at 615 K for ethanolamine, while the lack of N- or O-containing desorbates suggests that the dissociated N and O species are likely bonded to multiple surface Si atoms or diffused into the bulk at elevated temperatures (as confirmed by the corresponding temperature-dependent XPS spectra). Unlike the multidentate allyl alcohol and allylamine adstructures that have been found to be not favored kinetically, the present [O, N] bidentate ethanolamine adstructure appears to be kinetically favored on Si(100)2×1.

In the second materials science study, Cu NPs of three primary shapes have been deposited on H-terminated Si(100) by a simple, one-step electrochemical method. By precisely

manipulating the electrolyte concentration [$CuSO_4 \cdot 5H_2O$] below their respective critical values, cubic, cuboctahedral, and octahedral Cu NPs of ranges of average sizes and number densities can be easily obtained by varying the deposition time. Combined GIXRD and depth-profiling XPS studies show that these Cu NPs have a crystalline core-shell structure, with a face-centered cubic metallic Cu core and a simple cubic Cu_2O shell with a CuO outerlayer. The shape control of Cu NPs can be understood in terms of a progressive growth model under different kinetic conditions as dictated by different [$CuSO_4 \cdot 5H_2O$] concentration regimes. The two studies in the present work lay the foundation for future investigation of surface biofunctionalization of these fascinating Cu NPs with different shapes and therefore different surface chemistries as controlled by the relative amounts of the (100) and (111) facets, and their boundaries.

Acknowledgements

I would like to thank my supervisor Professor Tong Leung, who made the present thesis possible by giving me the opportunity to do my M.Sc. degree in his research group, and for his support during the last two years. In particular, I am thankful to his great patience and all the time he spent to teach me how to present the data and improve my thesis. I would like to thank all the professors who helped and supported me, including the present committee members Dr. Dale Henneke and Dr. P.N. Roy, the former member Dr. Eric Prouzet, and also Dr. Marcel Nooijen and Dr. Michael Chong for their precious advice and scientific discussions.

I would like to express my thanks to all my colleagues who vastly shared their knowledge and experience with me to be able to do research in two different fields during the short period of my work. I am thankful to Dr. Maryam Ebrahimi, who efficiently trained me on the UHV system, gave me confidence to run the surface science project, and provided all the valuable discussions during collecting, analyzing and presenting the data. I would also like to thank Dr. Youngku Sohn and Dr. Debabrata Pradhan, whose collaboration made me able to run the materials science project, particularly for all their help in electrochemistry and nanoscience. I would like to thank the former member of the group Dr. Michel Thiam and all the present members of WATLab. My big thank-you goes to my best friend and my teacher, Dr. Jake Fisher, who helped and advised me as a brother in most of the challenging situations.

I would like to appreciate the great help of the administrative coordinator of the Department of Chemistry, Mrs. Cathy van Esch, who made my life so easy by her very organized way of managing the paper-work. I am grateful to all the members of the Machine Shop and the Electronics Shop, who always did their best to facilitate my research project. I am thankful to all my friends that we spent joyful time together.

Finally, I would like to thank all the members of my family for their permanent support in my life, specially my parents who always believed in me.

Dedication

To my father and my mother

Table of Contents

List of Figures

List of Tables

Chapter 1

Introduction

1.1 Background and Motivation

The ultimate goal of the present research is to develop new understanding for biofunctionalization of metallic nanoparticles grown on a semiconductive support with organic molecules for potential medical and electronic applications. This type of research can be divided into several stages, each involving different studies that provide specific results to build toward the final goal. In particular, a materials science study is needed to grow well-defined metallic nanoparticles on a substrate with controllable morphology and chemical composition, in order to facilitate a study of their surface chemistry involving different facets and defects. Surface functionalization of the facets of these metallic nanoparticles is expected to be challenging. To gain some insight, a precursor study of the reactivity and selectivity of the corresponding single-crystal surfaces of the metal would be very helpful. In addition, the effect of the supporting substrate on the growth dynamics of the nanoparticles, along with the selectivity and reactivity toward the organic material used for the functionalization is crucial to enabling detailed comparison of results in different parts of the research and to illustrating the effect of the substrate on the entire functionalization process at the nanoscale.

Our choice for the supporting substrate was p-type single crystal Si(100), which is known to be the most commonly used semiconducting surface in modern industry,[1−5] and the nanoparticles of interest will be the important transition metal copper.[4,6−13] Multi-functional organic molecules, with their large variety and configurations and their tolerance toward engineering, form a versatile class of candidates to add chemical functionality to the nanosurfaces.[3,14,15] Among these multifunctional organic materials, molecules with two functional groups (or bifunctional molecules) have attracted much recent attention, because one functional group can be used to anchor the molecule to the surface while the other group can be used to form a new reaction site. This approach of surface functionalization can therefore be used to modify the surface reactivity and selectivity of the substrate, in effect creating a new surface with desirable chemistry for specific targeted applications.[16−19]

The present work will concentrate on the first two parts, involving the study of nanochemistry on the surface of Si(100) through two projects: a surface science project of

biofunctionalization of the Si(100)2×1 substrate surface with amino-containing bifunctional molecules, and a materials science project of controlling the shape of (and hence the amounts of different facets of) electrochemically deposited copper core-shell nanoparticles on a H-terminated Si(100) surface. In the future, further research will be needed to study the surface biofunctionalization of Cu single-crystal surfaces, and to pursue the final objective of functionalizing Cu nanoparticles grown on the surface of Si(100) and their resulting chemistry.

1.1.1 Structure of Si(100) (pristine and H-terminated) surfaces

Silicon has a diamond cubic crystal structure with space group (Fd-3m, 277).[20] Bulk Si has sp^3 hybridization with the atoms binding to one another through directional covalent bonds of 2.35 Å (elemental semiconductor).[21] Our single-crystal surface of interest results as the Si crystal is terminated along the (100) low Miller index plane. Along the area of termination, the silicon bonds break and produce two highly reactive dangling bonds for each surface atom (Figure 1a).

Under ambient condition, it is more likely that the highly reacted surface will be contaminated, especially with oxygen in a layer of insulating oxide. When the surface is H-terminated via hydrofluoric acid,[22] this layer can be removed and the hydrogen atoms saturate the dangling bonds maintaining the sp^3 hybridization of a relaxed 1×1 surface. As a result the temporary protective layer of H atoms, the surface remains uncontaminated and relatively conductive for the electrodeposition purposes (Figure 1.1b).

Under ultra-high-vacuum (UHV) conditions the clean Si(100) surface atoms bind to one another (in pairs) to reduce the surface free energy with bonds partially covalent partially ionic (compound semiconductor)[21] through a reconstruction process. Two surface atoms will bind by a strong σ and weak π bonds forming an asymmetric buckled dimer which dynamically tilts at room temperature.[23–25] Partial charge transfer from the buckled down atom to the buckled up atom occurs, giving the dimer atoms their electrophile-nucleophile nature on the 2×1 surface (Figure 1.1c).[24]

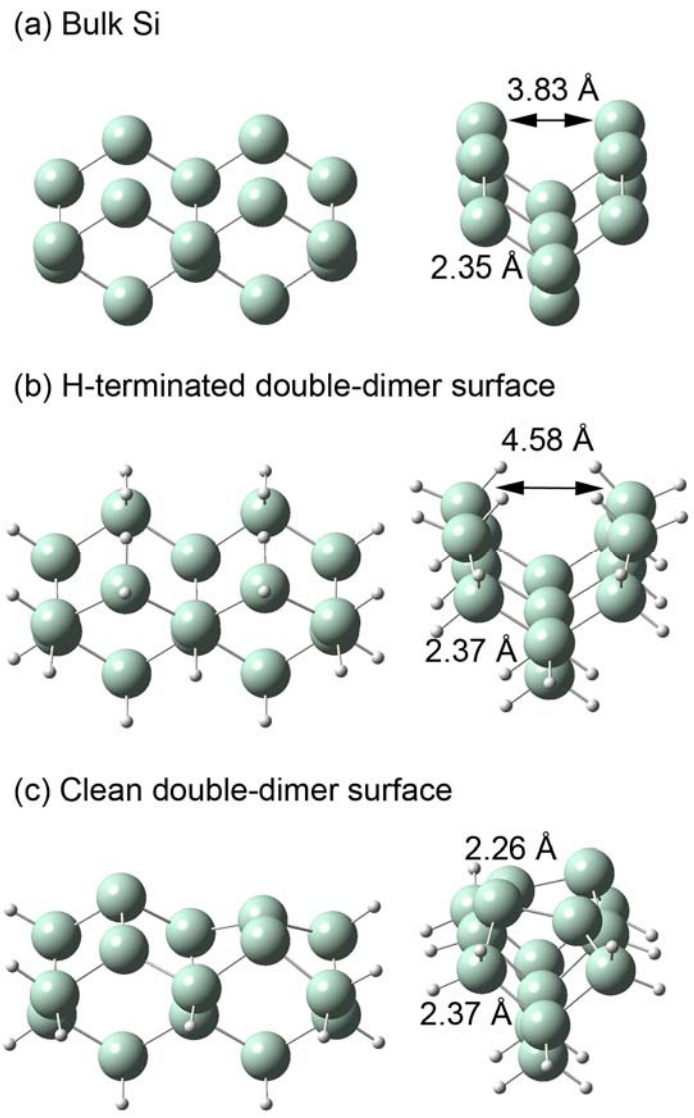

Figure 1.1 Geometries of (a) a bulk Si structure, (b) a model H-terminated Si(100)1×1 surface and (c) a model Si(100)2×1 reconstructed surface simulated by the double-dimer $Si_{15}H_{20}$ and $Si_{15}H_{16}$ clusters, respectively, as obtained by Density Functional Theory (DFT) calculations with B3LYP functional and 6-31++G(d,p) basis set.

1.1.2 Reactions of ethenyl-, amino-, and hydroxyl-containing bifunctional organic molecules on Si(100)2×1

The reactions of ethenyl, amino and hydroxyl-containing molecules with the 2×1 surface occurs on the dimer Si(100) atoms through different mechanisms and pathways. Usually, ethenyl group was found to undergo a [2+2] cycloaddition reaction with the Si=Si of the 2×1 surface at room temperature, forming a four member ring structure.[26−29] It should be noted that the symmetry forbidden [2+2] cycloaddition reaction[30] is allowed on the 2×1 surface due to the buckled nature of the dimer pair. Earlier reported studies found that the amino- and hydroxyl-containing molecules react through the heteroatom with the dimer electrophilic atom forming a dative bond. This preliminary step is followed by dissociating a hydrogen atom from the group, which will binds to the other nucleophilic atom, while the first atom undergoes further reactions.[31−41] It was found that for the 2×1 surface functionalization by the amino-containing molecule, N−H dissociative adsorption is the primary process, forming Si−N bond and a chemisorbed hydrogen.[23−25,38−40] Like the amino-containing molecules, the hydroxyl-containing molecules were found to react with the 2×1 surface through O−H dissociative adsorption and the formation of Si−O with a chemisorbed hydrogen.[30−32,37,41]

In earlier studies on the surface chemistry of bifunctional molecules on Si(100)2×1 surface, Ebrahimi et al. showed that different molecules bind to the surface through the hydroxyl,[84] carbonyl[84] and carboxyl[42] groups, keeping the ethenyl group (reference group) intact. In the surface science study of this research, we chose to extend this study to include the amino group and to provide an inter-comparison of the ethenyl, amino and hydroxyl groups in bifunctional molecules.

1.1.3 Electrochemical deposition of nanoparticles on H-terminated Si(100) surface.

The deposition of metals on that surface of p-type silicon occurs via the valence band, and the metal nucleates progressively forming 3D islands due to the weak interaction with the semiconducting surface.[43] Deposition of Cu nanoparticles on different surfaces have been widely studied and reported in literature.[35,44−59] In particular, several studies have been

conducted to investigate the deposition of copper nanoparticles on the different single crystal surfaces of Si(100) and Si(111).[29,56–58] Furthermore, other studies investigated controlling the shape of the deposited Cu nanoparticles on different surfaces.[22,23,54,60,61]

To date, no experimental study of controlling the shape of the electrodeposited copper nanoparticles on silicon surface has been reported. In our research we introduce a one-step method of depositing Cu nanoparticles of definite shapes on the H-terminated surface of Si(100), along with controlling their size and number density.

1.2 Overview of the Characterization Techniques

1.2.1 X-ray photoelectron spectroscopy (XPS)

XPS is a widely used surface sensitive characterization technique. It depends on the photoelectric phenomenon, discovered by Einstein, after which Siegbahn developed XPS into a method that he called Electron Spectroscopy for the Chemical Analysis (ESCA).[62] In XPS, a photon of energy $h\nu$ is incident upon a surface, and penetrates in the electronic shells of the atom inducing the emission of a core shell electron. The photoelectron then escapes the atom if the energy of the photon is higher than the binding energy (BE) of that electron and the excess energy will be converted to kinetic energy (KE) that can be detected by the spectrometer. This transformation of energy can be illustrated according to the well known Einstein photoelectric equation $BE = h\nu - KE$.[63]

The core shell electron is a good probe for the changes in the chemical environment, because it does not interfere with the reaction of the atoms, but it is affected by the changes in charge distribution of the outer electronic level as a result of different reactions through the valence electrons.[64] The oxidation state of the atoms and/or their electronegativity affects the BE of the photoelectrons causing chemical shifts that can be detected, giving further insight about the corresponding chemical environment.[65]

In the present work, XPS was used as the main characterization technique for both studies in two different systems. In the surface science project, XPS was used to observe any chemical shifts in the C 1s, N 1s, O 1s BEs resulting from different chemical environments as the molecules were rearranged on the surface upon adsorption. Following that, the sample was flash-annealed to different temperatures and each time re-cooled to room-temperature, after

which XPS spectra were recorded (a procedure known as temperature-dependent XPS). This helps in the study of thermal evolution of the adsorbates on the 2×1 surface. In the materials science project, XPS was used to detect Cu 2p and O 1s features which corresponding to various constituents of the nanoparticle as electrodeposited on a H-Si(100) surface. In order to analyze different constituents of the nanoparticles, the samples were sputtered down by Ar ions in specific steps with XPS recorded at each step (a procedure known as depth-profiling XPS). This allows us to decipher the constituents of the nanoparticles from the outer shells to the inner core.

1.2.2 Surface characterization tool

To study the thermal evolution of an adsorbate on a surface, thermal desorption spectrometry TDS, also known as temperature-programmed desorption (TPD), is used to qualitatively determine the nature of the desorption products from a surface exposed to a molecule. The TDS results give insight into the relative strengths of the different bonds of the adsorbate on the surface and illustrate their preferred evolution pathways as a function of temperature. In TDS, the adsorbate-covered surface is annealed while the desorbed species are detected in real time with a mass spectrometer.[62]

For the surface science project, TDS was combined with temperature-dependent XPS data to analyze the nature of the desorbates and the composition of the remaining species on the surface, as a function of annealing temperature which lead to better understanding of the possible desorption pathways.

1.2.3 Materials science characterization tools

Scanning-electron microscopy (SEM) is a type of microscopy that depends on electrons to probe the surface topography, which gives the microscope a magnification power of almost 200 times any normal microscope. The secondary electron imaging mode is the most used method in SEM and the resulted images clearly reveals the surface topography of the samples at a resolution of better than 5 nm.[66] The SEM images help to clarify the morphology and the number density of particles on a surface.

Generally, X-ray diffraction crystallography (XRD) is a technique used to determine the crystalline structure of a bulk material (single crystal or powder) depending on the well known

Bragg's law.[67] By using glancing-incidence XRD (GIXRD), this technique becomes compatible with probing the surface and near-surface regions with much smaller amount of material (thin films and nanoparticles). In GIXRD, the beam is fixed at an angle smaller than the critical angle of the total reflection (glancing-incidence). This makes the X-ray beam strike the surface at a small incident angle, at which part of the beam is reflected and the other propagates parallel to the surface with a penetration depth of few nanometers that can be increased by increasing the incidence angle. Both the reflected and the propagated portions of the X-ray will be diffracted by the sample and interfere then they can be detected.

In the materials science project, SEM was used to investigate the morphology (shape and size) and number density of the Cu nanoparticles electrodeposited on H-terminated Si(100), while GIXRD, with a small incidence angle of 0.1°, was used to determine the crystal structure of the nanoparticles different constituents.

1.3 Experimental Setup

1.3.1 Biofunctionalization of Si(100)2×1 under UHV condition

The experimental setup and procedure for the surface science project have been described in detail elsewhere.[68] Briefly, a home-built, ultrahigh vacuum dual-chamber system with base pressure better than 1×10^{-10} Torr was used (Figure 1.2). The upper sample preparation chamber was equipped with an ion-sputtering gun for sample cleaning and a four-grid retarding field optics for characterizing the surface morphology by low energy electron diffraction and surface cleanliness by Auger electron spectroscopy, as well as a gas handling system for sample dosing. The lower analysis chamber housed facilities for XPS and TDS analysis. In particular, an XPS electron spectrometer (VG Scientific CLAM-2), consisting of a hemispherical analyzer of 100 mm mean radius and a triple-channeltron detector, was used to analyze photoelectrons excited by unmonochromatic Al K_α radiation (at 1486.6 eV photon energy) delivered by a twin-anode X-ray source. A differentially pumped 1-300 amu quadrupole mass spectrometer (VG Quadrupole SXP Elite) was used to provide TDS measurements of mass fragments thermally desorbed from the sample. A home-built programmable proportional–integral–differential temperature controller was employed to provide a linear sample heating rate of 2 K s^{-1}.[69]

A 10×14 mm^2 Si sample was cut from a single-side polished, p-type (B-doped) Si(100) wafer (0.4 mm thick) with a resistivity of 0.0080-0.0095 Ω cm (Virginia Semiconductors). The sample was first solvent-cleaned and hydrogen terminated by using a standard RCA method under ambient condition.[22] The sample was then mounted on the sample manipulater mechanically by using Ta clamps at both ends, with a type-K thermocouple (wrapped in a Ta foil) securely fastened onto the front face at one end of the sample.[69] Detailed descriptions of the sample mounting and preparation procedures were given in our early work.[70] Briefly, the surface was cleaned in the preparation chamber by repeated cycles of Ar ion sputtering for 30 m (at an Ar gas pressure of 4×10^{-5} Torr, 20 mA emission current, and 1.5-2 keV ion beam energy) followed by annealing to 900 K for 5 m by passing a direct current through the sample. The sample was flash-annealed to 1100 K for 20 s to obtain the 2×1 reconstructed surface. The cleanliness of the surface was verified by the sharpness of the low energy electron diffraction (LEED) patterns and the lack of contaminant XPS features (e.g. C 1s and O 1s).

Allylamine and ethanolamine (99.9% purity), colorless liquids, were purchased from Sigma-Aldrich and were degassed by several freeze-pump-thaw cycles before exposure to the clean Si(100)2×1 surface. The exposure of the chemical was controlled by backfilling the sample preparation chamber to an appropriate exposure pressure (typically 1×10^{-6} Torr, as monitored by an uncalibrated ionization gauge) using a variable leak valve for a preselected time duration. All exposures were performed at room temperature and reported in units of Langmuir (1 L = 1×10^{-6} Torr sec). Unless stated otherwise, a saturation exposure has been used for both temperature-dependent XPS and TDS experiments.

XPS spectra were collected with an acceptance angle of ±4° at normal emission from the Si sample and a constant pass energy of 50 eV, giving an effective energy resolution of 1.4 eV full-width-at-half-maximum (FWHM) for the Si 2p photopeak. The binding energy (BE) scale of the XPS spectra has been calibrated to the Si 2p feature of the bulk at 99.3 eV. After appropriate background subtraction (using the Shirley background), individual XPS spectral components could be fitted with Gaussian-Lorentzian lineshapes by using the CasaXPS software. For temperature-dependent XPS experiments, the sample was flash-annealed to the preselected temperature and allowed to cool back to room temperature before collecting the XPS spectra. TDS profiles were obtained from the sample, after carefully positioned at 1 mm from the orifice (2 mm dia.) of the differentially pumped housing of the mass spectrometer to ensure that the

detected mass fragments originated only from the Si sample.[70] Due to the spatial separation between the thermocouple position and the sampling position viewed by the mass spectrometer, the temperature scale was calibrated by using the temperature of the desorption maximum for recombinative H_2 desorption from Si monohydrides (780 K).[71] The uncertainty of determining the desorption temperature was estimated to be ± 30 K.

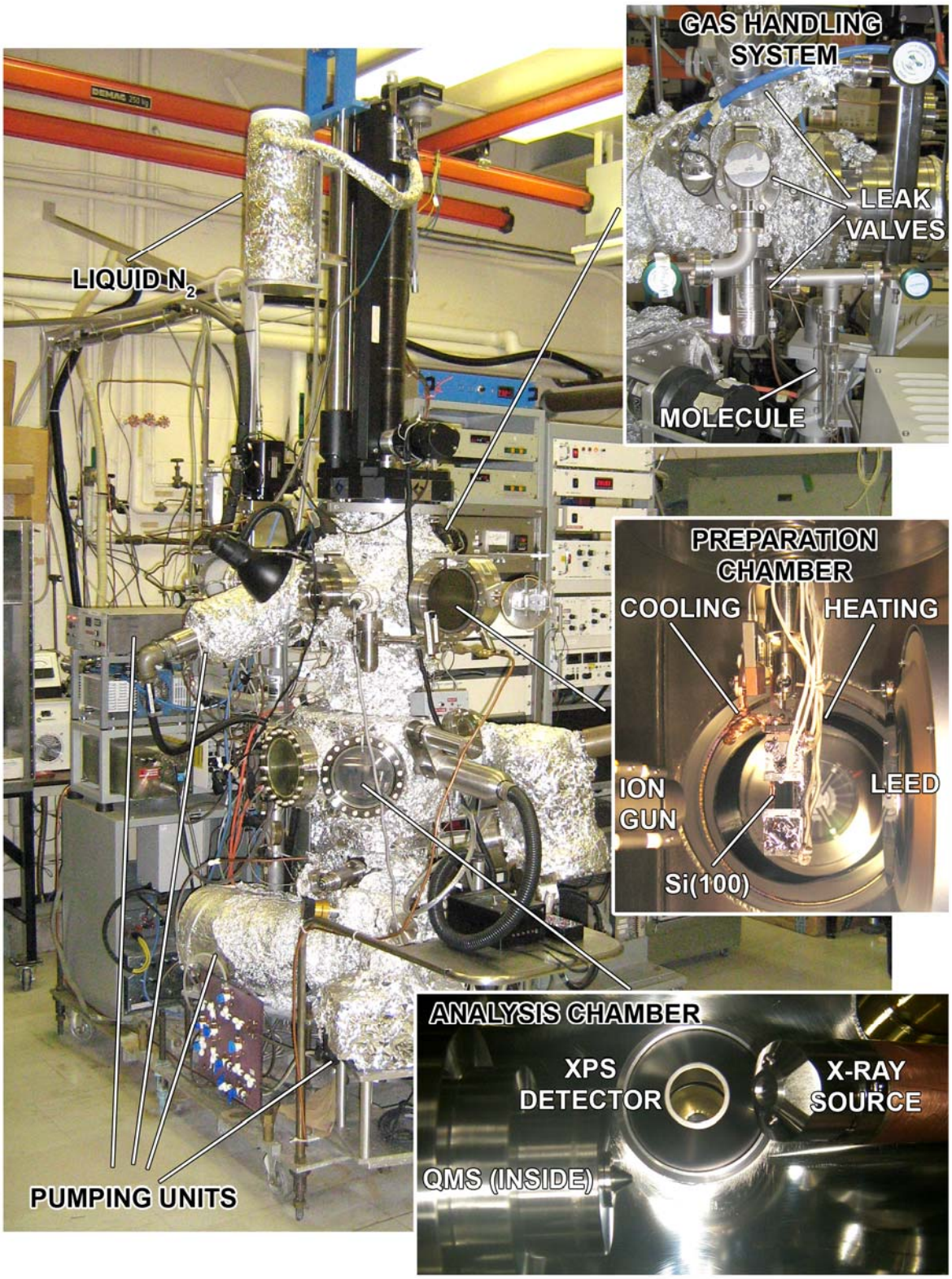

Figure 1.2 Photograph of the dual chamber UHV system used for the surface science study.

1.3.2 Electrochemical deposition of Cu on H-terminated on p-type Si(100)

For the materials science study, single-side polished B-doped Si(100) wafers (0.40 mm thick) with a resistivity of 1.0-1.5 mΩ·cm were cut into 15×2.5 mm^2 rectangular chips. The Si chips were cleaned and H-terminated by using a standard RCA method.[22] A potentio/galvanostat electrochemical workstation (CHI Instrument 660A) with a three-electrode cell (with Ag/AgCl, a platinum wire and the Si chip as the reference, counter and working electrodes, respectively) was used for all the electrodeposition experiments (Figure 1.3). Copper nanocrystals were deposited on the H-terminated Si(100) chips at room temperature in an aqueous Cu electrolyte solution for a preselected amount of deposition time by amperometry potentiostatically at a constant potential of −1.0 V (with respect to the Ag/AgCl reference electrode). The Cu electrolyte solution consisted of a preselected concentration of $CuSO_4 \cdot 5H_2O$ and a fixed concentration [10 mM (1 mM = 1×10^{-3} M)] of $NaClO_4$ used as the supporting electrolyte.[53,72] The electrolyte solution was appropriately deoxygenated by nitrogen bubbling for at least 20 m prior to use.[53] Two deposition parameters were used to produce Cu nanoparticles (NPs) with different shapes, sizes and number densities. In particular, the Cu electrolyte concentration [$CuSO_4 \cdot 5H_2O$] of 5, 10, 50, 100, 200 and 500 mM and the deposition time of 0.1, 0.5, 1, 2, 3, 4, 5, 6, 10, and 20 s were varied in a systematic fashion. The resulting Cu NPs were thoroughly rinsed with Millipore water (with a resistively of 18.2 MΩ·cm) and dried for at least 24 h in a nitrogen purged drying box prior to characterization.

Scanning electron microscopy (SEM) with a LEO FESEM 1530 microscope was used to determine the shape, size and number density of the Cu NPs electrodeposited on the Si(100) chip. The crystal structure of the Cu NPs was further characterized with GIXRD using a PANalytical X'Pert Pro MRD diffractometer with Cu Kα radiation (1.54 Å) at an incidence angle of 0.1°. The chemical composition of the Cu NPs was analysed by XPS as a function of sputtering depth (depth profiling) using a Thermo-VG Scientific ESCALab 250 Microprobe with a monochromatic Al Kα source (1486.6 eV), capable of an overall energy resolution of 0.4-0.5 eV full width at half-maximum (FWHM). Sputtering was performed by rasterring a 3.0 keV Ar^+ ion beam over a 3×3 mm^2 area of the sample at a typical sample current density of 102 nA/mm^2.

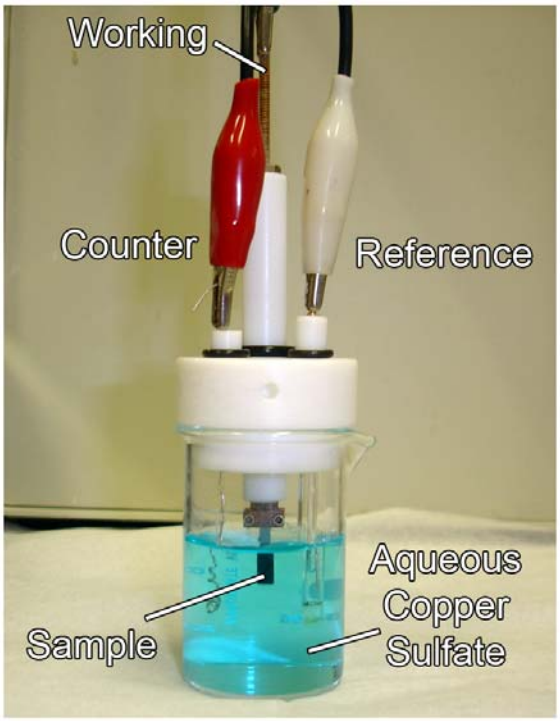

Figure 1.3 Photograph of the three-electrode cell (with a Ag/AgCl reference electrode, a platinum wire counter electrode, and the Si chip as the working electrode) used for the electrodeposition of copper nanoparticles on H-terminated Si(100) in an aqueous $CuSO_4 \cdot 5H_2O$ solution.

1.4 Computational Details

For the surface science project, electronic structure calculations were performed using the Density Functional Theory (DFT) with B3LYP functional[73] by using the Gaussian 03 package.[74] The hybrid B3LYP functional, consisting of Becke's 3-parameter gradient-corrected exchange functional[75] and the Lee-Yang-Parr correlation functional,[76] has been found to provide generally good agreement with the experimental data for the adsorption of many molecular systems on Si(100)2×1.[69,77,78] Moderately sized basis sets, including 6-31G(d), 6-31+G(d), 6-31++G(d), and 6-31++G(d,p), have been used in the present work and were found to give similar optimized geometries, with the larger basis set providing a lower total energy. To simulate the Si surface structure, the cluster model has often been used, with the one-dimer cluster (Si_9H_{12})[79] giving poorer comparison with the experimental bond lengths and tilting angles[80] than the double-dimer cluster ($Si_{15}H_{16}$),[4,81,82] and higher-order dimer clusters.[83] While higher-order dimer clusters

generally give better results, significant increase in the computational effort and time is required. In the present work, we employed the double-dimer cluster to model the Si(100)2×1 surface, because the double-dimer cluster offers a good compromise between accuracy and computational time, while facilitating observation of the dimer buckling effect and investigation of other phenomena related to inter-dimer interactions, which cannot be studied by using just a single-dimer cluster.[34] To obtain an initial guess for the $Si_{15}H_{16}$ cluster, we used a new procedure by first constructing the bulk structure from experimental crystallographic data[20,80] for the Si space group (Fd–3m 227) in the Diamond3 crystallographic freeware, and then followed by adding the terminal H atoms and refining the positions of the dimer atoms based on the experimental crystallographic data of the surface[33] in GaussView. The resulting cluster structure was then fully optimized with Gaussian 03. The present procedure can be easily extended to higher-order dimer clusters.

Furthermore, we also introduced a more systematic method of obtaining the equilibrium geometry of the free chain-like organic molecules (allylamine and ethanolamine), before allowing them to become adsorbates on the surface, by first calculating the total energy as a function of the dihedral angle. By scanning the dihedral angle of the four backbone atoms of allylamine (N⇾C–C⇽C) and ethanolamine (N⇾C–C⇽O), using a small basis set [6-31G(d)] over 360° in 1° steps, we could obtain not only all the local minima for the staggered and eclipsed conformer geometries but also the transition states, which eliminated the risk of missing the true local minimum in the structural optimization procedure. Once the local minima were found with the smaller basis set, they could be used for further optimization by using a larger basis set to provide a more refined geometry. The optimized conformer structures were then combined with that of the $Si_{15}H_{16}$ cluster to be fully optimized, without any geometrical constraint, to obtain the adsorbate-substrate configurations (ASCs). The corresponding adsorption energy, ΔE, was estimated by the difference between the total energy for the optimized structures of the ASCs and the sum of the total energies of a free conformer and the $Si_{15}H_{16}$ cluster. Frequency calculations were also performed for all of the optimized geometries, in order to assure that the local minima correspond to the equilibrium structures and not transition-state structures. All the total energies were obtained without zero-point correction and no basis set superposition error correction was made to ΔE.

1.5 Objectives and Scope

The present work has two main objectives: surface biofunctionalization of the Si(100)2×1 using amino-containing bifunctional molecules, and surface modification of H-terminated Si(100) with Cu nanoparticles (NPs) of different shapes.

In the surface science study, allylamine and ethanolamine will be used as two examples of bifunctional molecules containing the amino group, as one of the most important functional groups in the biochemical science. Studying biofunctionalization of the 2×1 surface will enable us to draw a conclusion about the relative reactivity of three functional groups (ethenyl, amino and hydroxyl), and it also helps to inter-compare them in these bifunctional molecules, along with an earlier study on allyl alcohol.[84] The observed chemical shifts in the N 1s spectra, together with both O 1s and C 1s XPS results will provide important clues about the plausible geometry of the adstructures at low and high exposures. Together with the temperature-dependent XPS and TDS measurements, these results will help us to develop a more comprehensive picture about the structure of the molecules as adsorbed on the 2×1 surface and their possible thermal evolution pathways. The geometries of the adstructures of both molecules will be also calculated and analyzed by using DFT method. By studying the three functional groups (ethenyl, amino and hydroxyl), it is possible to conclude that the Si(100)2×1 surface is more selective to form N−H and O−H dissociation products from the amino and hydroxyl groups, respectively, than any other possible reaction products, including [2+2] C=C cycloaddtion. No detectable preference between the amino and the hydroxyl groups is also evident.

In the materials science study, Cu NPs will be electrochemically deposited on H-terminated Si(100) using a one-step method in an aqueous $CuSO_4 \cdot 5H_2O$ solution under ambient condition. Studying the electrochemical parameters that affect the shape, size and number density of the resulted Cu NPs will allow us to develop a recipe for growing well defined particles that can be used for future stages of the research. The morphology (shape and size) and the number density, and crystal structures of the Cu NPs will be investigated by SEM and GIXRD, respectively. The results of depth-profiling XPS experiments (in Cu 2p and O 1s regions) will provide a detailed characterization of the chemical composition of the NPs. The present study shows that the $CuSO_4 \cdot 5H_2O$ concentration is a key parameter responsible for shape control, while the deposition time is important for controlling their size and number density.

The remainder of this thesis is organized into two parts. The first part involves the surface science study, in which the biofunctionalization of allylamine and ethanolamine on Si(100)2×1 will be presented in Chapter 2 and Chapter 3, respectively. The second, materials science study, involving the shape control of the electrodeposited Cu NPs on H-terminated Si(100) will be described in Chapter 4. In Chapter 5, we provide a concluding summary of the present results, and offer an outlook for future studies.

Chapter 2

Relative reactivities of amino and ethenyl groups in allylamine on Si(100)2×1: Temperature-dependent X-ray photoemission and thermal desorption studies of a common linker molecule

2.1 Introduction

Chemisorption of an organic molecule on a solid surface has been an important topic in numerous applications. In particular, the surface provides selectivity and catalytic activity in controlling how the molecule binds to the surface, which in turn adds new functionalities to the resulting adsorbate-substrate configuration.[1] These new surface functionalities could lead to better optimized surface properties, elimination of defects or undesirable characteristics, and/or introduction of totally new functions.[2] Si(100)2×1 has been one of the most important substrates in the semiconductor industry. In the generally accepted asymmetric buckled dimer model for the Si(100)2×1 surface, one of the two dangling bonds of a surface atom combines with one other dangling bond of a neighboring atom, forming a strong σ bond, while the remaining dangling bonds of the dimer pair in effect produces a weak π bond.[3] At room temperature, thermal motion causes the resulting dimer to dynamically tilt, creating the buckled dimer.[4] Partial charge transfer from the down-atom to the up-atom of the buckled dimer produces a electrophilic-nucleophilic pair (or a Lewis acid -Lewis base pair),[3] causing asymmetry in the bond lengths and remarkably different site-specific reactivity.[3,5] Like Si, the carbon atom belongs to Group IV, and organic molecules therefore offer natural bonding compatibility with the Si surface and they are widely used for surface functionalization.[6–8] In particular, multifunctional organic molecules are especially interesting, because one functional group can be used to anchor the molecule to a selected site on the surface, while the other functional groups provide different reaction sites for selective chemistry to occur. For example, Zhu et al.[9] used a series of chain-like bifunctional molecules containing amine, silane and pyrenyl groups as interconnects between different oxide surfaces and single-walled carbon nanomaterials, while Voue et al.[10] used grafted *N*-hydroxysuccinimidyl ester on a Ge surface for protein detection. Furthermore, Vieseh et al.[11] deployed bifunctional poly(ethylene glycol) polymer to functionalize the surfaces of Fe nanoparticles to make nanoprobes that recognize glioma cells. Finally, Haick and Cahen illustrated different techniques of using bifunctional organic molecules to connect two different surfaces for applications in molecular electronics.[12]

In order to understand the relative reactivity of simple organic molecules, particularly on the Si(100)2×1 surface, we have recently conducted a series of studies involving bifunctional molecules. By comparing the relative reactivities of several common functional groups including halogen atoms (Br,[13] Cl),[14] hydroxyl (OH),[15] carbonyl (C=O),[15] and carboxylic groups (COOH),[16] to a reference group such as ethenyl group (C=C), we obtain qualitative understanding of factors that control their reactivities on the Si(100)2×1 dimer surface. In the present work, we extend our study on bifunctional organic adsorbates on the 2×1 surface to a popular "linker" molecule,[17−24] allylamine (CH_2=CH−CH_2−NH_2),[25] which contains one of the most important hydrophilic groups in biological and biochemical sciences, the amino group (NH_2). In the studies of protein and DNA adsorption on metal[22,23,26,27] and Si surfaces, [17,24] the ethenyl group was used to attach allylamine to the surface while the amino group provided the reaction site to bind to other biological molecules. The surface functionalization by allylamine through the ethenyl group with a terminal amino group has in effect changed the native surface and enabled biological reactions to occur, further facilitating biomaterial-mediated tissue responses and cell adhesion.[20,27−30]

Several studies of allylamine on Si surfaces have been reported. In particular, Warner et al.,[31] and in separate theoretical study Wang et al.,[2] and Yamada,[17] showed, by using FTIR spectroscopy, that functionalization of Si quantum dots and H-terminated Si(111), respectively, by allylamine led to a hydrophilic surface terminated with NH_2.[17,31] However, a recent DFT calculation on allylamine adsorption on Si(100) by Prayongpan and Greenlief[32] showed N−H dissociative bonding on a modeled 2×1 surface of a single-dimer Si_9H_{12} cluster, in marked contrast to the previous work on Si(111).[17]

To date, no experimental study has been reported for the adsorption of allylamine on Si(100)2×1. Using X-ray photoelectron spectroscopy (XPS) and thermal desorption spectrometry (TDS), we demonstrate N−H dissociative adsorption of allylamine on the 2×1 surface, in contrast to the [2+2] C=C cycloaddition often found for molecules containing an ethenyl group on the 2×1 surface. By following the XPS spectra and desorption profiles as a function of temperature, we also show, for the first time, that the dissociatively adsorbed allylamine undergoes further dissociation to propene, ethylene and acetylene and to a N-containing adspecies below 740 K, the latter of which further evolves to form Si nitride at 825 K, where the hydrophobic Si–N(H)–CH_2CH=CH_2 surface in effect becomes a hydrophilic Si–N(H)

surface upon annealing. Furthermore, using a double-dimer $Si_{15}H_{16}$ cluster to model the (2×1) surface, we provide a more comprehensive description of plausible adsorption structures by Density Functional Theory (DFT) calculations. Despite the more negative calculated adsorption energies found for the multi-dentate adstructures, the unidentate N–H dissociation adspecies is preferred.

2.2 Results and Discussion

2.2.1 DFT computational study of adsorbate-substrate configurations

Figure 2.1 illustrates the changes in the bond length of a Si–Si dimer from the bulk Si structure to the (2×1) surface structure as modeled by the $Si_{15}H_{16}$ cluster structurally optimized by the B3LYP/6-31++G(d,p) calculation. Table 2.1 compares the corresponding total energies for the optimized cluster structure obtained with different basis sets. The bond length (2.27 Å) and the buckling angle (12.6°) for the Si-Si dimer of the optimized $Si_{15}H_{16}$ cluster are found to be close to the experimental values (2.41 Å, 20±3°)[33] and in good accord with previous theoretical study (2.26 Å, 12.2°).[34] It should be noted that increasing the number of dimers beyond the double-dimer (and the number of supporting layers to more than three) has been shown to only improve the agreement of the buckling angle with the experiment slightly.[34] However, the corresponding bond length (2.18 Å) and especially the buckling angle (1.3°) obtained for an optimized single-dimer Si_9H_{12} cluster (not shown) are discernibly worse when compared to the experiment and the double-dimer $Si_{15}H_{16}$ cluster. We therefore do not pursue calculations involving the single-dimer cluster in the present work.

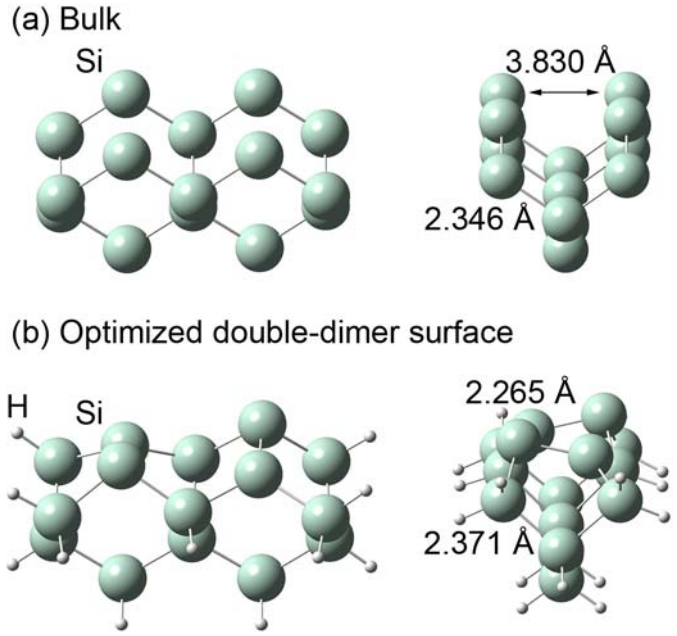

Figure 2.1 Geometries of (a) a bulk Si structure and (b) a model Si(100)2×1 surface simulated by the double-dimer $Si_{15}H_{16}$ cluster obtained by a DFT/B3LYP calculation with the 6-31++G(d,p) basis set.

Figure 2.2a shows the total energies for a free allylamine molecule optimized with a fixed dihedral angle over 0-360° in steps of 1° by a DFT/B3LYP calculation using a smaller basis set of 6-31G(d). This initial calculation identifies the approximate dihedral angles for the local extrema. Using these approximate structures as our initial guess, the equilibrium geometries of these local extrema are further refined with a larger 6-31++G(d,p) basis set without constraint to a fixed dihedral angle. From the calculated energies and frequencies, three local minima at dihedral angles of 126.0°, 236.1° and 353.0° and three respective transition states at 53.9°, 192.3° and 292.7° (each with one negative frequency) are clearly evident (Figure 2.2b). The structures of the two allylamine staggered conformers with dihedral angles of 126.0° (Figure 2.2, Structure A) and 236.1° (Figure 2.2, Structure B) are similar, and they are effectively mirror image of each other. All three conformers, including the eclipsed conformer with a dihedral angle of 353.0° (Figure 2.2, Structure C), differ from one another in dihedral angle by approximately 120°. Table 2.1 compares the total energies for the optimized geometries of the three conformers (at three local minima) for four different basis sets. Not surprisingly, the total

energies of the three conformers are found to be effectively identical within the limitation of the present calculation, i.e. with a difference less than 0.003 hartree (or 7.88 kJ). Furthermore, the small energy barriers among local minima, with at most 0.006 hartree (or 15.75 kJ), suggest that the three conformers are equally probable at room temperature.

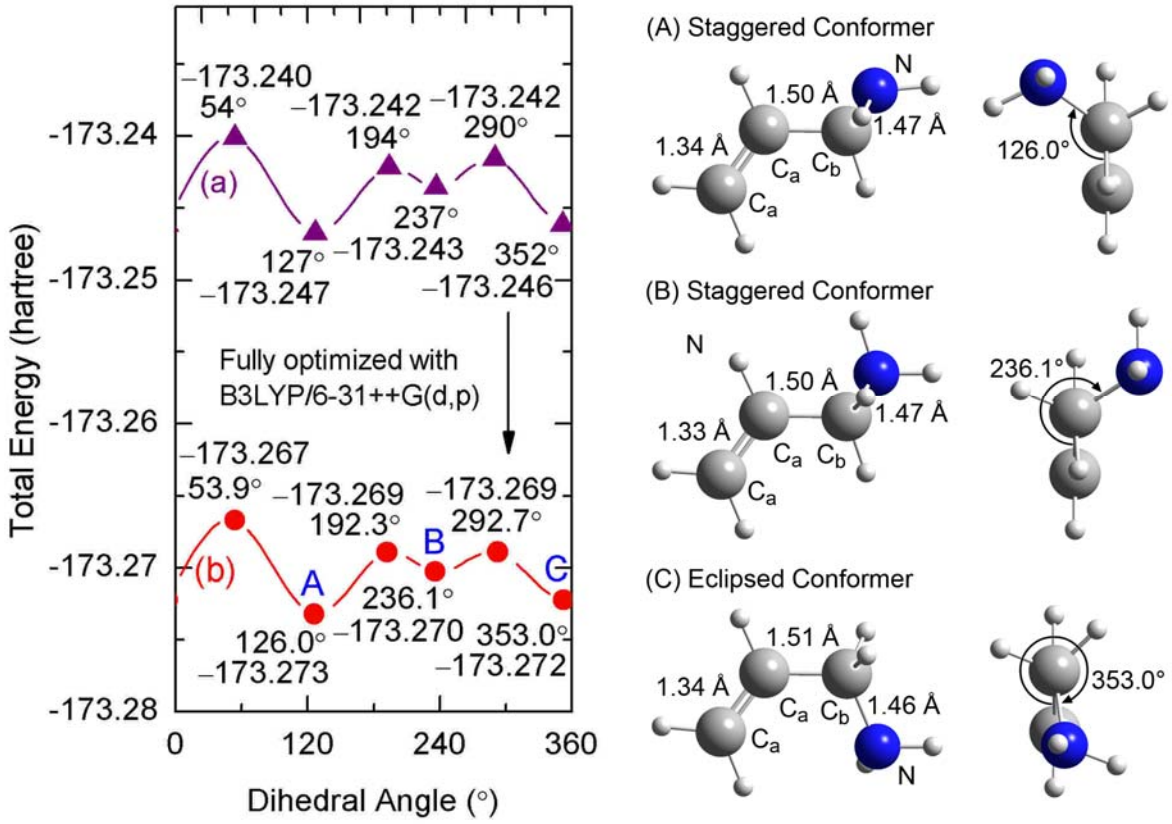

Figure 2.2 Total energies of allylamine conformers (a) obtained with a fixed dihedral angle from 0° to 360°, in steps of 1°, by DFT/B3LYP calculations using a 6-31G(d) basis set, and (b) upon further refinement at the extrema without any geometric constraint by a larger 6-31++G(d,p) basis set (left). The total energies (given in hartree) and the dihedral angles (in degree) for the staggered (A, B) and eclipsed (C) conformers, along with their respective transition states are also indicated. The corresponding equilibrium structures of the conformers obtained by the DFT/B3LYP/6-31++G(d,p) calculation are also shown (right).

Figure 2.3 shows plausible ASCs obtained from geometry optimization of allylamine eclipsed (E) conformer (Figure 2.2, Structure C) and staggered (S) conformer (Figure 2.2, Structure A), respectively, on the double-dimer $Si_{15}H_{16}$ model surface for Si(100)2×1 (Figure 2.1b). Table 2.1 summarizes the corresponding adsorption energies and total energies for the ASCs calculated by the DFT/B3LYP method for four different basis sets. As expected, the total energies of the ASCs obtained by the larger basis set are more negative than those obtained by the smaller basis set. Furthermore, while the adsorption energies do not appear to follow a particular trend with increasing size of the basis set, the 6-31++G(d,p) basis set generally gives the least negative value. ACS E1 (Figure 2.3a) and ASC S1 (Figure 2.3d) correspond to unidentate adstructures resulting from N–H dissociation of E and S conformers, respectively, leading to the formation of Si–N and Si–H bonds on the Si dimer pair. ASC E2 (Figure 2.3b) and ASC S2 (Figure 2.3e) correspond to similar N−H dissociative products with the dissociated H bonded on a neighbouring dimer diagonally across from the Si−N bonding site (cross-dimer). It should be noted that unrestricted B3LYP method has been used to obtain convergence for the open-shell structures of ASCs E2 and S2. Not surprisingly, the adsorption energies for N−H dissociative products are found to be quite similar to one another, with ΔE for ASC E1 (−218.47 kJ mol^{-1}) [S1 (−213.80 kJ mol^{-1})] more negative than that for ASC E2 (−194.95 kJ mol^{-1}) [S2 (−209.71 kJ mol^{-1})], which could be qualitatively attributed to extra energy required for H migration from one dimer to another. Furthermore, ASC E3 (Figure 2.3c) and ASC S3 (Figure 2.3f) correspond to the respective bidentate adstructures resulting from [2+2] C=C cycloaddition reaction of the ethenyl group of the E and S conformers. The dative bonding between N and the electron-deficient down-atom site of the Si dimer leads to the attachment of allylamine to Si through N followed by N–H dissociation to eventually form ASC E1 (S1). Generally, the reduction of the π bond (of Si dimer) and the subsequent formation of two Si−C bonds in the cycloaddition reaction has been generally found to produce a less stable adstructure than the corresponding N−H dissociation reaction. In the present case, we also observe a less stable [2+2] C=C cycloaddition product for ASC E3 (ΔE = −169.50 kJ mol^{-1}) than ASC E1. However, a more stable cycloaddition product is found for ASC S3 (ΔE = −231.72 kJ mol^{-1}) than ASC S1, which is likely due to the formation of dative bonding between N and Si through the N electron lone-pair brought about by the proximity of the amino group to the neighboring Si dimer. The remaining ASC E4 or S4 (Figure 2.3g) involves double interactions of both amino and ethenyl

groups of either the E or S conformer with the two Si dimer pairs to produce essentially the same [N, C, C] tridentate adstructure. The adsorption energies for the tridentate ASCs (−337.78 kJ mol^{-1} for E4 and −335.14 kJ mol^{-1} for S4) are found to be the most negative among all the ASCs, which suggests that the tridentate ASCs are the most thermodynamically stable adstructures. Despite the most negative values found for the tridentate ASCs, we do not expect these to play a major role, because of the high activation energy needed for multiple bond dissociations (such as N–H and C=C).

It is also of interest to note that the bond lengths for the unidentate ASCs (E1, E2, S1, S2) are found to be essentially unchanged (within 0.01 Å) from those of the free conformers (Figure 2.1), and the Si−N bond length (1.75 Å) is also identical for all the unidentate ASCs as well as the tridentate ASCs. For the cycloaddition products, the Si−C bond length (1.95 Å) is essentially the same for both E3 and S3, while the corresponding C=C bond length has changed from 1.34 Å to that of the C−C value (1.58 Å), with the other C−C and C−N bond lengths remaining unchanged, upon [2+2] cycloaddition. Furthermore, with the exception of ASC S1 (with a dihedral angle of 131.2°), the other ASCs S2 (85.9°) and S3 (48.2°), as originated from the staggered conformer (126.0°), have evidently rearranged to the eclipsed form. Such a structural rearrangement is expected to have a higher activation barrier (and therefore less likely to occur) than those for ASCs E1 (352.8°), E2 (352.3°), and E3 (294.4°) as originated from the eclipsed conformer (353.0°).

By using a double-dimer $Si_{15}H_{16}$ cluster to model the substrate surface, we have provided a more comprehensive picture of the adsorption phenomena involving allylamine than the recent computational work involving the single-dimer Si_9H_{12} cluster reported by Prayongpan and Greenlief.[32] In particular, the present calculation reveals the additional adstructures resulting from different conformers, cross-dimer H migration, and multiple interactions with two dimer pairs such as ASC S3 and the [N, C, C] tridentate ASCs. More importantly, the buckling effect of the double-dimer has been fully taken into account, thereby providing an improved and more realistic picture of the ASC geometries.

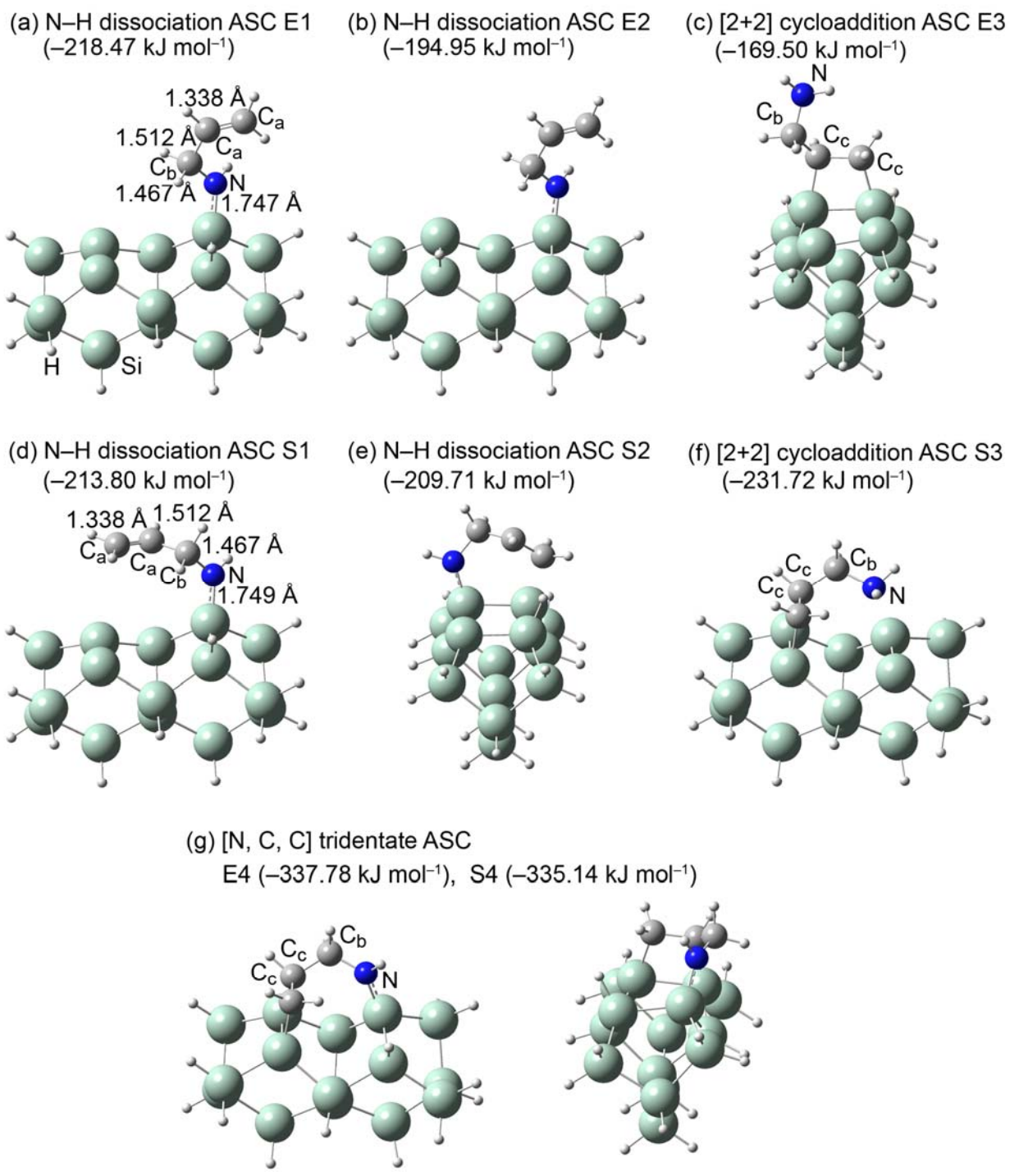

Figure 2.3 Optimized geometries of the adsorbate-substrate configurations (ASCs) for eclipsed (a, b, c, g) and staggered conformers (d, e, f, g) of allylamine on a model Si(100)2×1 surface: (a, b, d, e) N−H dissociation, (c, f) [2+2] C=C cycloaddition, and (g) [N, C, C] tridentate products. The corresponding adsorption energies calculated with the 6-31++G(d,p) basis set are given in parentheses.

Table 2.1 Adsorption energies (in kJ mol^{-1}), where applicable, and total energies (in hartree), given in square parentheses, of the double-dimer $Si_{15}H_{16}$ cluster, free allylamine staggered (S) and eclipsed (E) conformers, and different adsorbate-substrate configurations (ASCs) obtained by DFT/B3LYP calculations with four different basis sets.

Adsorption Energy (kJ mol^{-1}) [Total Energy (hartree)]		Basis Set			
		6-31G(d)	6-31+G(d)	6-31++G(d)	6-31++G(d,p)
$Si_{15}H_{16}$ cluster		[–4352.059071]	[–4352.071932]	[–4352.073387]	[–4352.091204]
Allylamine Conformers with Dihedral Angle	126.0° (S)	[−173.246768]	[−173.259134]	[−173.259364]	[−173.273235]
	236.1°	[−173.243553]	[−173.256035]	[−173.256309]	[−173.270268]
	353.0° (E)	[−173.246158]	[−173.258024]	[−173.258229]	[−173.272228]
ASC E1		–232.426903 [–4525.393756]	–223.194018 [–4525.414967]	–223.351836 [–4525.416687]	–218.467199 [–4525.446641]
ASC E2*		–208.870287 [–4525.384783]	–199.721391 [–4525.406027]	–199.812732 [–4525.407722]	–194.952013 [–4525.437685]
ASC E3		–176.925802 [–4525.372616]	–170.436827 [–4525.394873]	–170.721300 –4525.396641	–169.496215 [–4525.427989]
ASC E4		–357.911757 [–4525.441550]	–343.308043 [–4525.460716]	–343.396943 [–4525.462410]	–337.775590 [–4525.492083]
ASC S1		–231.644951 [–4525.414263]	–218.431728 [–4525.414263]	–218.559800 [–4525.415996]	–213.795804 [–4525.445868]
ASC S2*		–228.503776 [–4525.392871]	–215.065496 [–4525.412981]	–214.939892 [–4525.414618]	–209.710053 [–4525.444312]
ASC S3		–253.479344 [–4525.402384]	–234.443786 [–4525.420361]	–234.506536 [–4525.422070]	–231.716837 [–4525.452694]
ASC S4		–356.311173 [–4525.441550]	–340.394316 [–4525.460716]	–340.418497 [–4525.462410]	–335.137697 [–4525.492084]

* The unrestricted B3LYP functional has been used to take into account of the unpaired electrons of these ASCs.

2.2.2 XPS study of the allylamine adsorption on Si(100)2×1 at room temperature

The XPS spectra of allylamine on Si(100)2×1 have been collected for a number of room-temperature exposures (0.5 L, 2.5 L, 5 L, 10 L, 20 L, 50 L, 100 L, and 200 L), and the similarities in the spectral profiles suggest that the predominant adspecies are the same over the range of studied exposure. In Figure 2.4, we show representative N 1s and C 1s spectra for a low (2.5 L) and a saturation exposure (100 L). Evidently, except for the lower overall intensities, the shapes of both the N 1s and C 1s spectra are essentially unchanged from the low to saturation exposure. The single broad N 1s feature at 398.9 eV BE (with 1.9 eV FWHM) (Figure 2.4a, 2.4b) can be attributed to Si–N(H)−C≮, in good accord with earlier studies that reported N 1s BE at 398.4-399.1 eV for N−H dissociation products.[35−40] It should be noted the N 1s BEs for *tert*-butylamine, diethylamine, and methylethylamine,[35] dimethylamine and trimethylamine,[38] 1,4-phenylenediamine[39] and other alkylamines[40] physisorbed on Si(100)2×1 or dative bonded to the surface through the electron lone-pair have been reported at 399.5-402.3 eV.[35−40] The present N 1s assignment is also in good agreement with the N 1s BE (399.1 eV) for glycine on Si(111)7×7 upon dissociative N−H adsorption.[41] Based on the present assignment, we can rule out the [2+2] C=C cycloaddition ASCs E3 and S3 (Figure 2.3) as the plausible adsorption products, because of the lack of N 1s feature at a higher BE associated with the terminal amino group (399.5-402.3 eV BE).[35−40]

The C 1s spectra (Figure 2.4c, 2.4d) are fitted with two broad peaks at 284.6 eV and 286.2 eV BE (with 1.7 eV FWHM). Previous studies showed that the C 1s BEs for C–N (285.9-286.2 eV) and C=C bonds (284.2-285.0 eV) are generally higher than that Si–C (284.3-283.2 eV).[16,35,36,38,40,42,43] The observed C 1s features at 284.6 eV (C_a) and 286.1 eV (C_b) can therefore be attributed to the ethenyl C (C=C) and methylene C in the C–N bond, respectively. Furthermore, the approximate relative intensity ratio of 2 to 1 found for C_a 1s and C_b 1s is in good accord with the stoichiometric ratio of the ethenyl to methylene C atoms, further supporting our present assignment. The absence of any discernible feature below 284.3 eV BE confirms that the formation of Si–C bonds, as a result of [2+2] C=C cycloaddition of the ethenyl group, is unlikely and therefore can be used to exclude multi-dentate ASCs (E3, S3, E4, and S4, Figure 2.3). This observation is in marked contrast to the formation of a Si−C bond (via saturation of C=C to form a unidentate adstructure) found for allylamine on Si(111)[17] and Si quantum dots.[31]

Our XPS data therefore definitively identify the presence of the unidentate N−H dissociation products (ASCs E1, E2, S1, and S2), despite their less negative ΔEs than those of the multi-dentate ASCs (Table 2.1), which suggests that the formation of these unidentate adspecies is kinetically controlled.

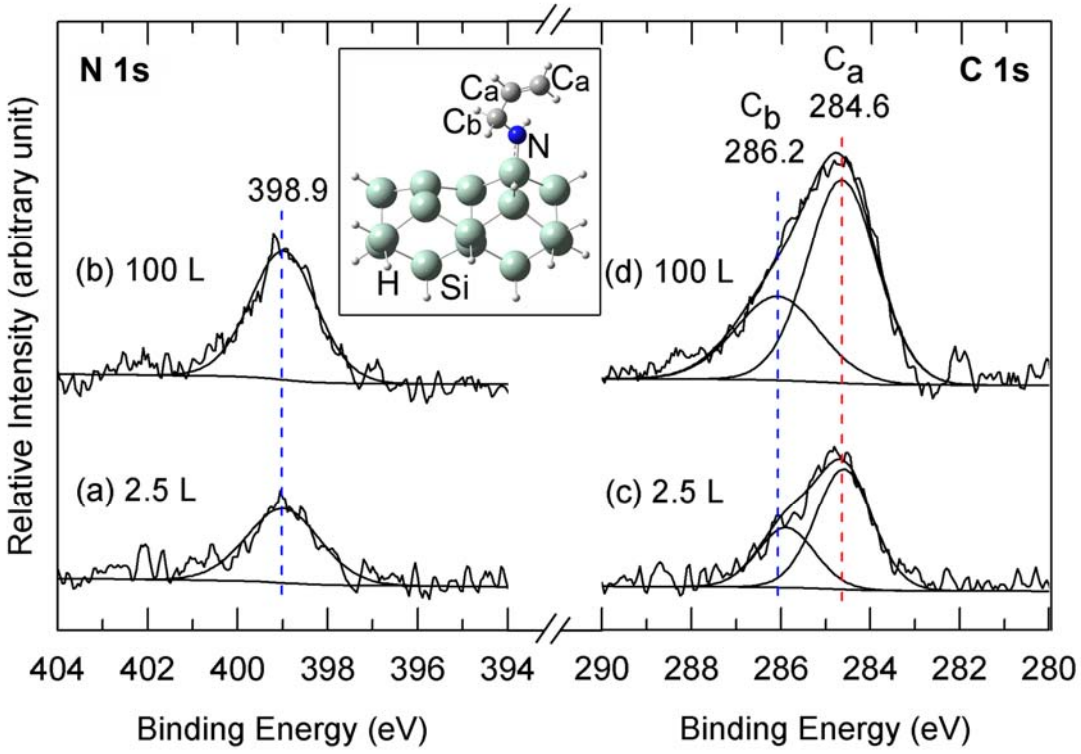

Figure 2.4 XPS spectra of C 1s (right) and N 1s regions (left) for (a, c) a low (2.5 L) and (b, d) a saturation (100 L) exposures of allylamine on Si(100)2×1 at room temperature. The inset shows a plausible N−H dissociative adstructure with the ethenyl C_a and methylene C_b atoms appropriately identified.

2.2.3 Temperature-dependent XPS and TDS studies of thermal evolution products

Figure 2.5 shows the XPS spectra of N 1s and C 1s regions for a saturation (100 L) room-temperature exposure of allylamine on Si(100)2×1 surface collected upon flash-annealing to different temperatures. The corresponding intensities of individual fitted N 1s and C 1s components, relative to the intensity of the Si 2p peak, are also shown as a function of flash-annealing temperature. The N 1s feature for Si−N(H)−C≮ at 398.9 eV is found to be remarkably stable, with essentially no reduction in the intensity, up to 565 K (Figure 2.5a). From 650 K to 825 K, the N 1s feature for Si−N(H)−C≮ has almost completely diminished, while a new feature at 397.7 eV BE emerges and becomes a dominant feature. The intensity of the latter feature remains effectively unchanged upon further flash-annealing to 1090 K. The N 1s feature at a lower BE can be assigned to Si−NH, present either as a radical or bridge-bonded to a second Si atom as Si–N(H)–Si, resulting from C−N bond cleavage of the unidentate N−H dissociation adspecies (ASC E1). Elimination or replacement of C with an electronegativity (χ) of 2.5 (Pauling scale)[44] with a better electron donor such as Si (χ = 1.8) is expected to increase the partial negative charge of N (χ = 3.0), which in turn causes the corresponding N 1s feature to appear at a lower BE.

The present assignment for similarly adsorbed NH fragments is also consistent with the BEs (397.2-397.8 eV) for alkylamines and other amino-containing species adsorbed on Si(100) reported previously.[35−40] It is of interest to note that only a relatively minor reduction (24%) in the overall intensity of N 1s features at 650-740 K is observed (Figure 2.5b), which indicates predominant dissociative conversion of unidentate N−H dissociation adspecies into NH-containing fragments on the surface. Furthermore, the lack of relevant N-containing desorption fragments at 650-740 K as illustrated by our TDS data below rules out the desorption of any N-containing species from the surface and suggests that the observed reduction corresponds to diffusion of dissociated N (or NH) fragments into the bulk.

Like the N 1s spectrum, the corresponding C 1s spectral envelope remains unchanged until the flash-annealing temperature of 565 K (Figure 2.5c) is reached. Between 565 K and 650 K (Figure 2.5c), the methylene C_b 1s peak at 286.2 eV is found to undergo a marked reduction and becomes totally diminished at 740 K (Figure 2.5c). As expected, the temperature evolution

of C_b 1s therefore parallels that of the N 1s feature at 398.9 eV, both of which mark the C−N bond cleavage at 565-740 K. In contrast to the C_b 1s feature, the intensity of the ethenyl C_a 1s feature at 284.6 eV has remained unchanged up to the annealing temperature of 740 K, above which dramatic intensity reduction is observed. This reduction in intensity continues to 825 K and is complete at 910 K (Figure 2.5d). This indicates that above 740 K, the dissociated propenyl species ($–CH_2CH=CH_2$) stays on the surface and undergoes further dissociation into smaller fragments (e.g. $−CH_2$, $−CH=CH_2$) on the surface and/or desorption. Starting at 740 K and becoming more notable at 825 K, the emergence of a new C 1s feature at 283.2 eV, commonly attributable to SiC, [16,35,36,38,40] is clearly evident (Figure 2.5g). The growth of the SiC feature is complete at 910 K, above which no significant change is found (to 1090 K). The growth evolution of the SiC feature is consistent with the proposed thermal dissociation of smaller C-containing fragments into CH_n and finally to C on the surface above 740 K. In contrast to the minor reduction in the total N 1s intensity, a considerable loss in the total C 1s intensity (>43%) is found over the flash-annealing temperature range. This larger intensity C 1s reduction indicates that a significant amount of C has been removed from the surface through the thermal desorption of C-containing adspecies.

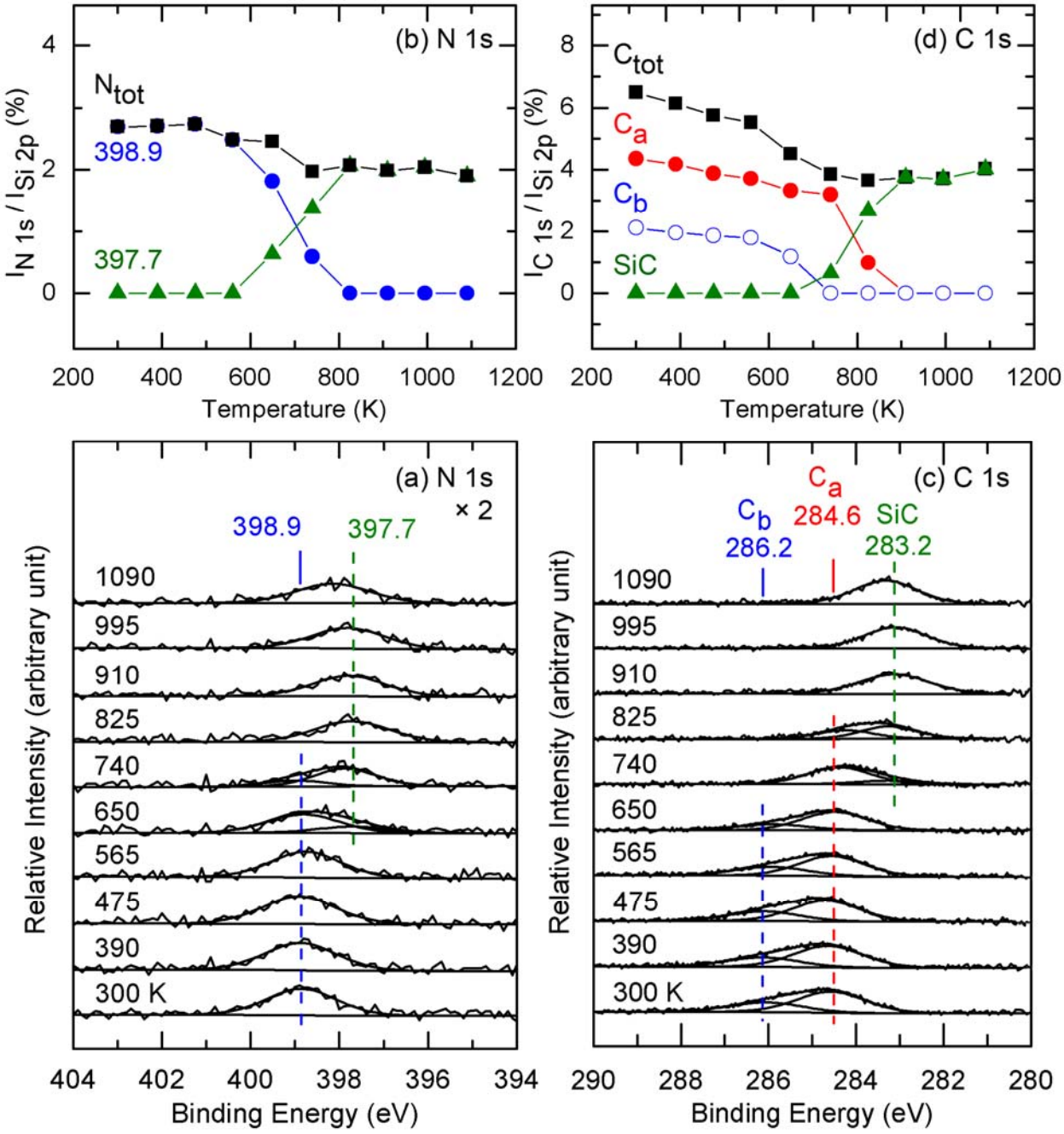

Figure 2.5 Temperature-dependent XPS spectra of (a) N 1s region and (c) C 1s region for a saturated exposure (100 L) of allylamine on Si(100)2×1 at 300 K, and upon sequential flash-annealing to 390 K, 475 K, 565 K, 650 K, 740 K, 825 K, 910 K, 995 K and 1090 K. Corresponding temperature profiles of the intensities of (b) N 1s ($I_{N\ 1s}$) and (d) C 1s ($I_{C\ 1s}$) for Si−N(H)−C≮ at 398.9 eV, Si_xN at 397.7 eV, SiC at 283.2 eV, C_a at 284.6 eV and C_b at 286.2 eV, along with their total intensities N 1s (N_{tot}) and C 1s (C_{tot}), all with respect to Si 2p ($I_{Si\ 2p}$).

In order to determine the desorption products thermally evolved from the adspecies remaining on the surface (as inferred from Figure 2.5), TDS experiments were performed. Figure 2.6 shows the TDS profiles of selected mass fragments of m/z 2, 26, 27, 28, 39, 41, and 42 for a room-temperature saturation exposure (100 L) of allylamine on Si(100)2×1. It should be noted that we have also monitored other mass fragments including m/z 17, 30, 31, 56 and 57 but found no detectable intensity. The lack of m/z 56 ($C_3H_5NH^+$) and m/z 57 ($C_3H_5NH_2^+$) signals, corresponding respectively to the base mass and parent mass of allylamine, indicates that the unidentate N−H dissociation adspecies does not desorb molecularly from the surface.[25] Furthermore, the absence of detectable TDS signals for m/z 30 ($CH_2NH_2^+$) and m/z 31 ($CH_3NH_2^+$), corresponding to the base mass of both methylamine and ethylamine and to the parent mass of methylamine, respectively, and for m/z 17 (NH_3^+), corresponding to the parent (and base) mass of ammonia, shows that N-containing adspecies do not desorb from the surface. This observation therefore confirms our earlier proposal that N fragments likely diffuse into the bulk (Figure 2.5d). For m/z 2 (Figure 2.6a), the large desorption feature observed at 780 K can be attributed to the recombinative desorption of H_2 from silicon monohydrides.[45]

For the remaining TDS profiles in Figure 2.6, a common desorption feature at 580 K has been found for m/z 26, 27, 28, 39, 41 and 42, suggesting a common source. Given that the cracking pattern of propene ($CH_3CH=CH_2$) contains m/z 26 ($C_2H_2^+$), m/z 27 ($C_2H_3^+$), m/z 39 ($C_3H_3^+$), m/z 40 ($C_3H_4^+$), m/z 41 ($C_3H_5^+$, base mass) and m/z 42 ($C_3H_6^+$, parent mass),[25] the TDS feature at 580 K could correspond to recombinative desorption of propene, arising from a propenyl radical ($•CH_2CH=CH_2$) with hydrogen, upon C−N bond cleavage observed at 565-650 K in Figure 2.5. The TDS feature of m/z 28 ($C_2H_4^+$, parent and base masses of ethylene) found at 580 K suggests desorption of ethylene, the cracking pattern of which also includes m/z 27 ($C_2H_3^+$) and m/z 26 ($C_2H_2^+$). The additional desorption intensities found for m/z 27 and m/z 26 not accountable from desorption from propene could therefore be attributed to ethylene desorption at 580 K. In addition, an additional TDS feature at 700 K is also observed for m/z 26 (Figure 2.6b) and not for other mass fragments, which corresponds to desorption of acetylene (with m/z 26 as its parent and base masses), generally found at a similar temperature as reported in earlier studies.[15,46]

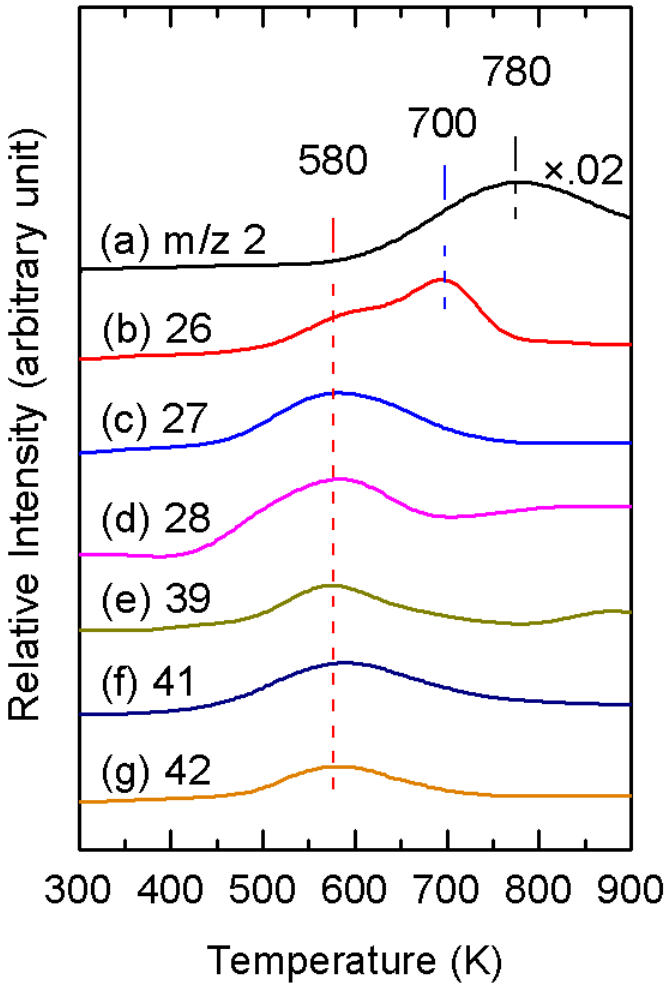

Figure 2.6 TDS profiles for selected fragments of m/z (a) 2, (b) 26, (c) 27, (d) 28, (e) 39, (f) 41, and (g) 42 for a saturation (100 L) exposure of allylamine on Si(100)2×1 at room temperature.

Figure 2.7 summarizes the schematic pathways proposed for the thermal evolution of unidentate N–H dissociation adspecies (e.g., ASC E1). In particular, the unidentate adspecies (Structure I) undergoes N−C bond cleavage (Structure II), producing the propenyl radical ($•CH_2−CH=CH_2$, Structure IIa, IIc) that either recombines with H and desorbs as propene (pathway b) at 490-685 K (Structure IIb) or stays on the surface with the formation of Si−C bond (pathway c). The propenyl adspecies further dissociates via C−C bond breakage (Structure IId), producing methyl radical (attached to the surface through a Si−C bond) and ethenyl radical ($CH_2=CH•$, Structure IIe) that desorbs as acetylene at 700 K (Structure IIf). Both pathways (a and b) result in the formation of Si−N(H)−Si that remains stable on the surface (up to our maximum attainable temperature of 1090 K). The unidentate adspecies (Structure I) could also evolve through (pathway d) with C−C bond cleavage (Structure III) to form ethenyl radical and ($•CH_2−NH−Si$) adspecies (Structure IV). The ethenyl radical could recombine with hydrogen and desorb as ethylene (pathway e) at 490-685 K (Structure IVd) or dehydrogenate as acetylene (pathway f), at 635-755 K (IVb), while the C−N bond cleavage of the remaining methylene amine adspecies could lead to the formation of methylene and methyl adspecies (with Si−C bond formation), respectively, along with Si−N(H)−Si. Given that hydrogen abstraction involves the breakage of Si−H bond (with a bond dissociation energy of 293 kJ mol^{-1}) [47] to produce ethylene while dehydrogenation involves dissociation of C−H bond (399 kJ mol^{-1}) to produce acetylene, it is therefore not surprising that the desorption maximum of m/z 26 for acetylene occurs at a higher temperature (700 K) than those of m/z 26, 27, and 28 for ethylene (580 K). Furthermore, the similar desorption maxima of m/z 26, 27, 28, 39, 41 and 42 found for propene and ethylene (both at 580 K) are consistent with the similar bond dissociation energies of C–N (356 kJ mol^{-1}) and C–C bonds (385 kJ mol^{-1}) required, respectively, in the formation of propenyl (pathway a) and ethenyl adspecies (pathway e). It should also be noted that the ethenyl radical produced through pathways c (Structure IIe) and e (Structure IVc) could also stay on the surface and undergo total decomposition to form smaller hydrocarbon fragments that give rise to the SiC C 1s features observed above 700 K (Structure IIg).

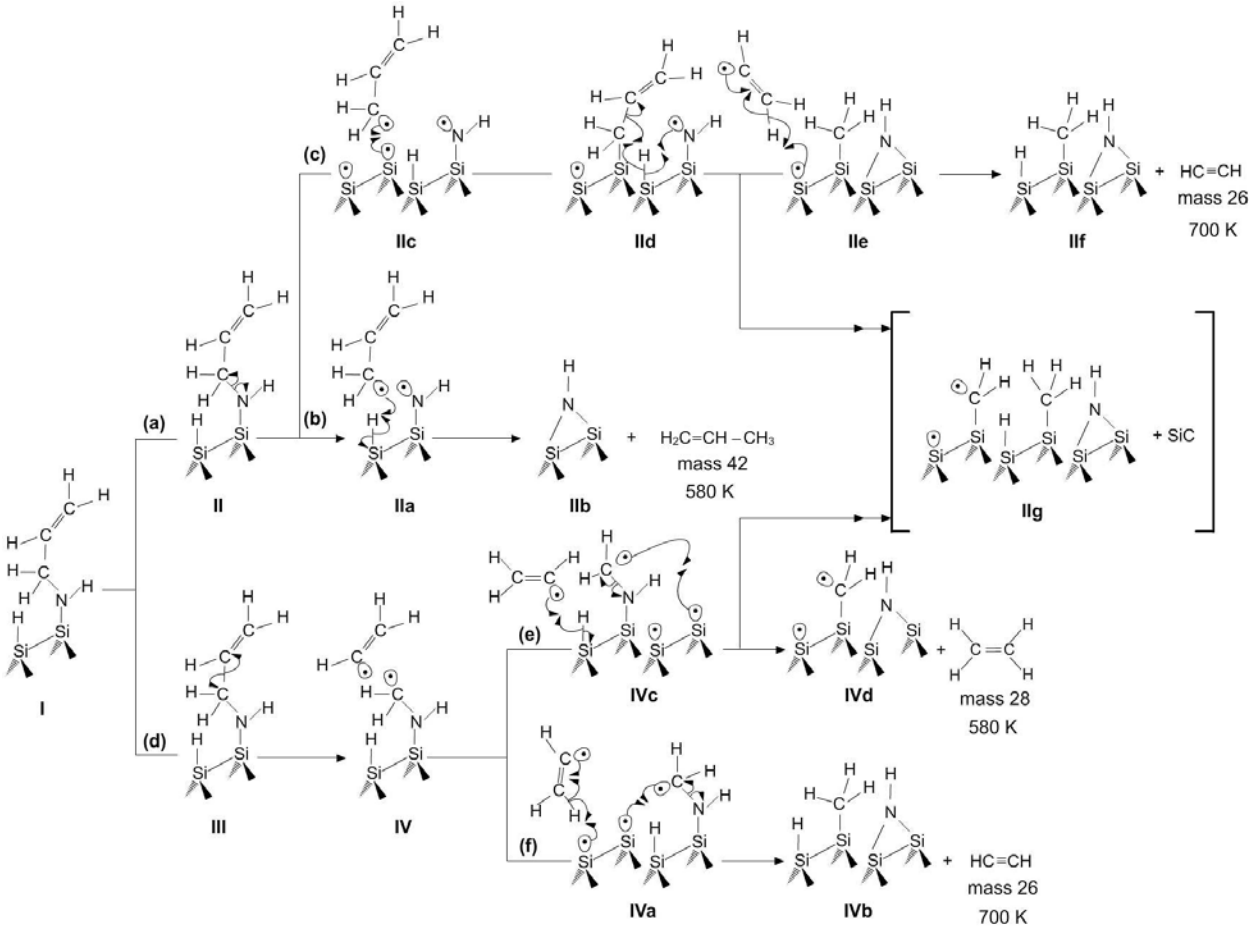

Figure 2.7 Schematic model for thermal evolution of an unidentate N–H dissociation adspecies (Structure I), depicting the possible pathways for the formation of Si−N(H)−Si, and propene, ethylene and acetylene, along with surface C-containing fragments (e.g., CH_2, CH_4).

2.3 Concluding Remarks

In the present work, we have carried out temperature-dependent XPS and TDS experiments on the room-temperature adsorption of allylamine on Si(100)2×1. Detailed DFT calculations, involving both the eclipsed and staggered conformers of allylamine on a model surface based on the double-dimer $Si_{15}H_{16}$ cluster, have also been employed to interpret our data. Our XPS results show that room-temperature adsorption of allylamine on Si(100)2×1 leads to a unidentate N–H dissociation adspecies, instead of the bidentate [2+2] C=C cycloaddition or [N, C, C] tridentate adspecies. This result is in good accord with the previous work on the adsorption of the amino-containing molecules on Si(100), in which N–H dissociative adsorption through the amino group is found to be the primary process.[35−40] In our earlier work on ethenyl-containing bifunctional molecules (allyl alcohol, allyl aldehyde,[15] and acrylic acid)[16] on Si(100)2×1, we show that adsorption proceeds through surface reactions of the hydroxyl,[15] carbonyl,[15] and carboxyl[16] groups, with the ethenyl group remaining intact. The present work also shows that the amino group is more reactive than the ethenyl group and that N−H dissociative adsorption is the preferred route. The nature of the surface bonding for allyamine on Si(100)2×1 is, however, in marked contrast to that found for the adsorption of allylamine on Si(111)[17] and Si quantum dots,[31] which show that an unidentate adspecies through saturating one of the ethenyl C atoms with the amino group intact. This difference suggests that the surface structure itself [i.e. (100) vs (111)] plays an important role in the adsorption of bifunctional molecules.

In addition to the formation of propene desorbate, our TDS data on allylamine also show common desorbates, such as ethylene and acetylene, arising from thermal evolution of the ethenyl group, that are also found for allyl alcohol, allyl aldehyde,[15] and acrylic acid on Si(100).[16] The formation of Si−N(H) and/or Si−N above 650 K is also confirmed with the presence of the respective N 1s features in our temperature-dependent XPS study. Surface functionalization of Si(100)2×1 by allylamine therefore offers a number of interesting control opportunities, by first converting the double-bond of a Si dimer of the 2×1 surface to a C=C double bond of the "dangling" ethenyl group after N−H dissociative adsorption, which effectively replaces silicon chemistry by organic chemistry to better serve the role of an organic linker molecule. By annealing the functionalized surface to 825 K, the organic moiety is

desorbed and the surface is transformed to a N or NH terminated Si surface, in fact converting a hydrophobic surface to a hydrophilic surface. Such a conversion can be easily achieved by controlling the annealing temperature.

Finally, our DFT calculations based on the double-dimer cluster have significantly extended the calculation of Prayongpan and Greenlief (based on the single-dimer cluster)[32] and confirm that the unidentate N−H dissociation adspecies as the preferred adstructure model. However, the use of the double-dimer cluster to model the 2×1 surface has allowed us to uncover new [N, C, C] tridentate ASCs (with ΔE = –335.14-(–337.77) eV), which are considerably more stable than the N−H dissociation ASCs (with ΔE = –194.95-(–218.47) eV), in contrast to the [2+2] cycloaddition ASCs (with ΔE = –169.50-(–231.72) eV) being only slightly more stable. Despite this considerably more stable tridentate ASCs, our experimental results implicate the unidentate N−H dissociation adspecies as the only viable product, which suggests that the formation of such an adstructure is kinetically favored on the Si(100)2×1 surface. This latter result shows that a sufficiently large cluster is necessary to model the 2×1 surface in order to provide a more comprehensive picture and new insights to the intricate silicon surface chemistry of bifunctional organic molecules.

Chapter 3

Competitive bonding of amino and hydroxyl groups in ethanolamine on Si(100)2×1: Temperature-dependent X-ray photoemission and thermal desorption studies of thermal surface chemistry of a double chelating agent

3.1 Introduction

Organic functionalization of a Si(100) surface has attracted a lot of recent attention not just in the semiconductor industry but also in emerging applications, including nanomedicine and molecular electronics.[1−6] These organic adsorbates are essential and versatile in introducing a variety of new functionalities, including optical, electronic, chemical or biological activity on Si surfaces.[3,7,8] In the asymmetric buckled dimer model for the Si(100)2×1 surface,[9,10] one of the two dangling bonds of a surface atom combines with one other dangling bond of a neighbouring atom, forming a strong σ bond, while the remaining dangling bonds of the dimer pair produces a weak π bond. The asymmetric charge distribution of the down-atom and the up-atom of the buckled dimer produces an electrophilic-nucleophilic pair, causing remarkably different site-specific reactivity.[9,11] Among the organic molecules commonly used for functionalization, bifunctional molecules are particularly interesting, because one functional group can be used to anchor the molecule to a selected centers on the surface, while the other functional group serves as new reaction site for selective reactions to occur. For example, bifunctional organic molecules have been reported for use as interconnection between two surfaces,[12] and in protein detection,[13] biological nanoprobes,[14] and molecular electronic components.[15]

In order to control the adsorption and the subsequent surface reactions of such complex organic molecules on Si(100)2×1, systematic studies to better understand the competitions among different functional groups in simpler adsorbates would be very useful. We have recently conducted a series of studies involving bifunctional organic molecules on Si(100)2×1 surfaces. By comparing the reactivities of several common functional groups, including halogen atoms (Br,[16] Cl),[17] hydroxyl (OH),[18] carbonyl (C=O),[15] carboxylic (COOH),[19] and more recently amino (NH_2) groups,[20] to a reference group such as ethenyl group (C=C), we obtain insights into factors that control their reactivities on the 2×1 dimer surface. In the present work, we give the first inter-comparison between two of these functional groups, particularly, hydroxyl and amino groups, in a simple bifunctional molecule, ethanolamine ($OH{-}CH_2{-}CH_2{-}NH_2$).[21] Along with

allyl alcohol[18] and allylamine,[20] the study of ethanolamine completes the comparison cycle (among OH, NH_2 and C=C).[18,20] Ethanolamine is a nontoxic, biologically interesting molecule that represents one of the basic building blocks of phospholipids in biological membranes, and it has been used in industrial scrubbers, power plants, pharmaceutical and household products.[22]

To date, several studies on the interactions of molecules containing either the amino group[23−28] or the hydroxyl group[2,29−33] with the Si(100)2×1 surface have been reported. In general, these studies show that the molecules bind to the 2×1 surface through either N−H or O−H dissociation, resulting in the formation of Si−N and Si−O bonds, respectively.[2,23−25,29−32,38−40] In particular, Wu et al.,[23] Cao and Hamers,[24,38,40] Hlil et al.,[25] and Kugler et al.[28] found that different amino-containing molecules (including *tert*-butylamine, diethylamine, and methylethylamine,[23] dimethylamine and trimethylamine,[38] 1,4-phenylenediamine[39] and other alkylamines[40]) bind to the 2×1 surface through N−H dissociative adsorption by using X-ray photoelectron spectroscopy (XPS). Similarly for the hydroxyl-containing molecules (including propanol,[2] methanol,[29,33] ethanol,[30] isopropanol and *tert*-butanol,[31] 2,3-butanediol[32]), Zhang et al.,[2] Shannon and Campion,[29] Eng et al.,[30] Kim et al.,[31] Kim et al.[32] and Casaletto et al.[33] also observed O−H dissociative adsorption on the 2×1 surface by using vibrational and electron-based techniques. In addition, a Fourier Transform Infrared and XPS study on the adsorption of formamide (NH_2CHO) on Si(100)2×1 reported by Bu and Lin[34] showed that formamide adsorbs on the 2×1 surface through the carboxyl O with the NH_2 group intact.

In our recent work on bifunctional organic molecules, we observe N−H and O−H dissociative adsorption of allylamine[20] and allyl alcohol,[18] respectively. These dissociative adsorption processes are favored over the [2+2] C=C cycloaddition, which indicates that the NH_2 and OH groups are more reactive than the ethenyl group on the 2×1 surface. The present work will present the first data on the adsorption of ethanolamine on Si(100)2×1, specifically comparing the reactivities of the NH_2 and OH groups. Using XPS and thermal desorption spectrometry (TDS), we show that the adsorption of ethanolamine involves double dissociation of both the N−H and O−H bonds on the 2×1 surface, producing a unique bridge-like structure [–O–C–C–N(H)–] between two Si dimer atoms. This result suggests that the NH_2 and OH groups are equally reactive on the Si dimer sites. Our temperature-dependent XPS spectra and TDS profiles further reveal the remarkable stabilities of the resulting organized templates of NH

and O terminated Si dimer pairs, and ethylene as the only desorbate. These observations are supported by our Density Functional Theory (DFT) calculations of the relevant adstructures on a double-dimer model surface of a $Si_{15}H_{16}$ cluster.

3.2 Results and Discussion

3.2.1 DFT computational study of adsorbate-substrate configurations

Figure 3.1a shows the total energies for a free ethanolamine molecule optimized with a fixed dihedral angle over 0-360° in steps of 1° by a DFT/B3LYP calculation using a smaller basis set 6-31G(d). Using these approximate structures as our initial guess, the equilibrium geometries of the local extrema are further refined with a larger 6-31++G(d,p) basis set without constraint to a fixed dihedral angle. Based on the calculated energies and frequencies, we identify three local minima at dihedral angles of 65.3°, 177.6° and 285.5° and three respective transition states at 123.4°, 243.8° and 360.0° (each with one negative frequency), all of which separate from one another by approximately 120° (Figure 3.1b). The structures of the two ethanolamine eclipsed conformers with dihedral angles of 65.3° (Figure 3.1, Structure A) and 285.5° (Figure 3.1, Structure C) are complementary to each other. Table 3.1 compares the total energies for the optimized geometries for the three conformers (at the three local minima) for four different basis sets. The total energies of the three conformers are found to be effectively identical within the limitation of the present calculation, i.e. with difference less than 0.005 hartree or 13.13 kJ. The small energy barriers among the local minima, with at most 0.008 hartree or 21.00 kJ, suggest that the three conformers are equally probable at room temperature. Given the similarities in the geometries of the two eclipsed conformers, we therefore choose only one of the eclipsed conformers (Structure A, with a slightly more negative total energy than Structure C), along with the staggered conformer (Structure B) for the adstructure calculations below.

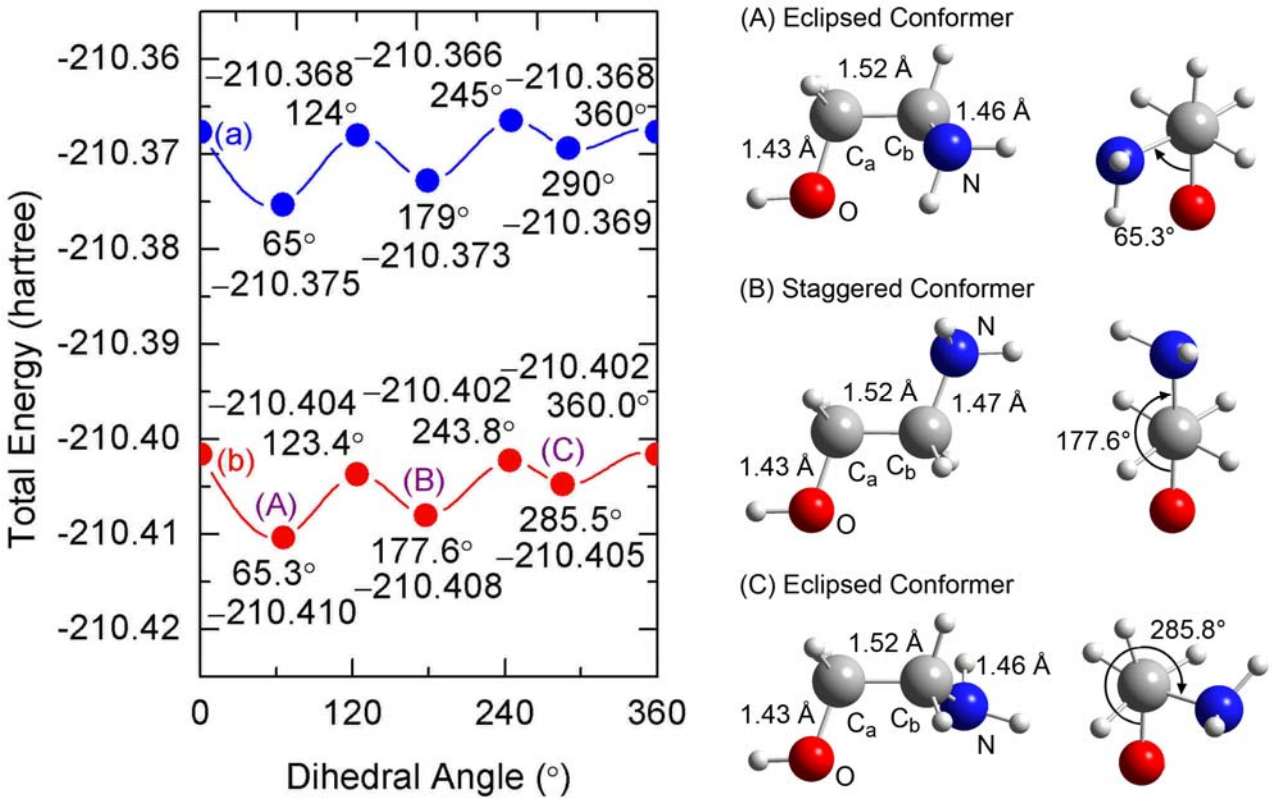

Figure 3.1 Total energy of free ethanolamine conformers (a) obtained over a fixed dihedral angle from 0° to 360°, in steps of 1°, by DFT/B3LYP calculations using a 6-31G(d) basis set, and (b) upon further refinement by a larger 6-31++G(d,p) basis set (left). The total energies (given in hartree) and the dihedral angles (in degree) for the eclipsed (A, C) and staggered (B) conformers, along with their respective transition states are also indicated. The corresponding equilibrium structures of the conformers obtained by DFT/B3LYP/6-31++G(d,p) calculation are also shown (right).

Figure 3.2 shows three different types of plausible ASCs obtained from geometry optimization of ethanolamine eclipsed (E) conformer (Figure 3.1, Structure A) and staggered (S) conformer (Figure 3.1, Structure B) on a double-dimer $Si_{15}H_{16}$ model surface for Si(100)2×1. In particular, single dissociation of the O–H or N–H bond leads to unidentate ASCs through the respective formation of the Si–O and Si–H bonds (Figure 3.2a, 3.2b, 3.2e, 3.2f) or Si–N and Si–H bonds on a Si dimer pair (Figure 3.2c, 3.2d, 3.2g, 3.2h). Double dissociation of the O–H and N–H bonds could give rise to the corresponding bidentate ASCs (Figure 3.2 i-k). It should be noted that unrestricted B3LYP method has been used in order to obtain convergence for the open-shell structures of ASCs E3, E4, S3 and S4. Table 3.1 summarizes the corresponding adsorption energies and total energies for the ASCs calculated by the DFT/B3LYP method for the four different basis sets. Not surprisingly, the total energies of the ASCs obtained by the larger basis sets are more negative than those obtained by the smaller basis sets. Although the adsorption energies do not appear to follow a particular trend with increasing size of the basis set, the 6-31++G(d,p) basis set gives the least negative value. Evidently, the adsorption energies for unidentate O–H dissociation ASCs E1 (S1) [–327.52 kJ mol^{-1} (–255.37 kJ mol^{-1})] and E2 (S2) [–322.18 kJ mol^{-1} (–233.65 kJ mol^{-1})] are found to be more negative than the corresponding unidentate N–H dissociation ASCs E3 (S3) [–218.29 kJ mol^{-1} (–217.61 kJ mol^{-1})] and E4 (S4) [–303.44 kJ mol^{-1} (–203.06 kJ mol^{-1})] (Figure 3.2), which suggests that O−H dissociation is more thermodynamically favorable than N−H dissociation. Moreover, the intra-dimer ASCs (E1, S1 and S3) are generally more stable (with more negative ΔEs) than the respective inter-dimer ASCs (E2, S2 and S4) (with less negative ΔEs), except for E3 and E4, which could be qualitatively attributed to additional energy required for H migration to a neighboring dimer in the inter-dimer ASCs. Furthermore, the adsorption energies for eclipsed (E) ASCs are generally more negative than those of the respective staggered (S) ASCs, which suggests that the closer proximity of the unattached functional group in the eclipsed ASCs to the surface facilitates better interaction which tends to stabilize the adstructures.

In the case of [O, N] bidentate ASCs, double O–H and N–H dissociation of both the eclipsed and staggered conformers leads to the most thermodynamically stable adstructures with discernibly similar adsorption energies. The intra-dimer [O, N] bidentate ASCs (ΔE = –442.80-–448.87 kJ mol^{-1}, Figure 3.2i) are only slightly more stable than the corresponding inter-dimer

ASCs (ΔE = –438.86-–448.41 kJ mol^{-1}, Figure 3.2j), while the cross-dimer ASCs gives the least negative ΔEs (–381.22-–411.08 kJ mol^{-1}, Figure 3.2k). It is of interest to note that the intra-dimer [O, N] bidentate ASC (Figure 3.2i) forms a six-member organosilicon ring [Si–O–C–C–N(H)–Si], while the inter-dimer ASC (Figure 3.2j) and cross-dimer ASC (Figure 3.2k) represent a seven-member and a eight-member rings, respectively. In organic chemistry, the reaction pathway is generally faster for closing a six-member ring complex than a seven-member or eight-member ring complex,[35] which suggests that the formation of the intra-dimer ASCs would be faster and therefore kinetically more favorable than the inter-dimer ASCs and cross-dimer ASCs. As we shall show below that these bidentate ethanolamine ASCs, unlike their corresponding multidentate allyl alcohol[18] and allylamine counterparts,[20] appear to be the most likely adstructures with respect to the experimental data, suggesting that the formation of these bidentate ASCs is indeed kinetically favored on Si(100)2×1.

It is also of interest to note that the bond lengths for the unidentate and bidentate O–H dissociation and N–H dissociation ASCs are found to be essentially unchanged (within 0.01 Å) from those of the free conformers. The Si–O (1.69 Å) and Si−N bond lengths (1.75 Å) are also identical for all the unidentate and bidentate ASCs. The most notable structural changes are found in the dihedral angles of unidentate O−H dissociation ASCs E1 (114.9°) and E2 (81.6°) from that of the free E conformer (65.3°). Changes in the dihedral angles for bidentate ASCs (74.5° for E5, 97.1° for E6, and 59.9° for E7) are considerably less pronounced with respect to the free E conformer (65.3°) than the S conformer (177.6°).

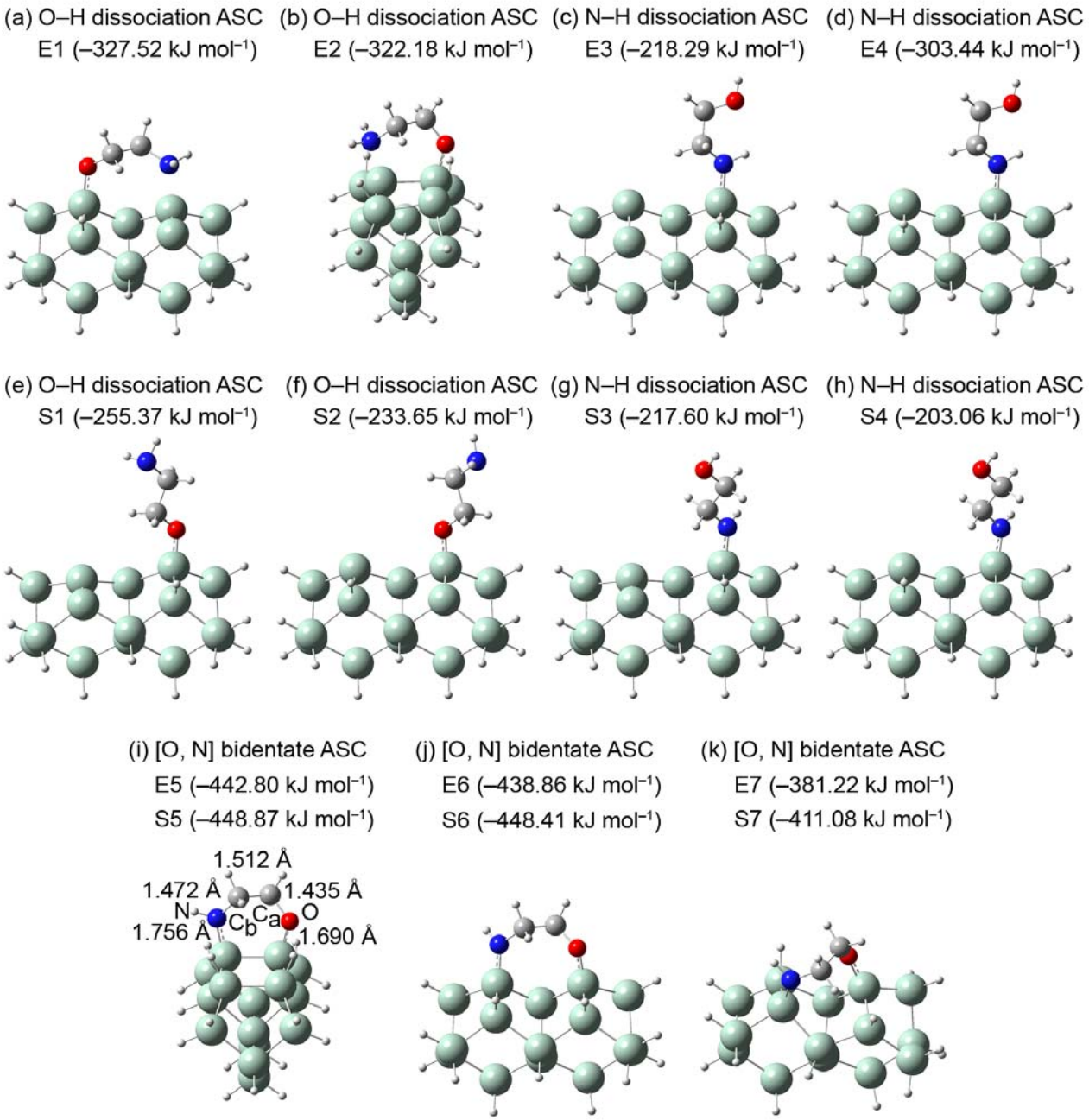

Figure 3.2 Optimized geometries of the adsorbate-substrate configurations (ASCs) for eclipsed (a, b, c, d) and staggered conformers (e, f, g, h) of ethanolamine on a model Si(100)2×1 surface: (a, b, e, f) O−H dissociation, (c, d, g, h) N−H dissociation, and (i) intra-dimer, (j) inter-dimer, and (k) cross-dimer [O, N] bidentate products. The corresponding adsorption energies calculated with the 6-31++G(d,p) basis set are given in parentheses.

Table 3.1 Adsorption energies (in kJ mol^{-1}), where applicable, and total energies (in hartree), given in square parentheses, of the double-dimer $Si_{15}H_{16}$ cluster, free ethanolamine eclipsed (E) and staggered (S) conformers, and different adsorbate-substrate configurations (ASCs) obtained by DFT/B3LYP calculations with different basis sets.

Adsorption Energy (kJ mol^{-1}) [Total Energy (hartree)]		Basis Set			
		6-31G(d)	6-31+G(d)	6-31++G(d)	6-31++G(d,p)
$Si_{15}H_{16}$ cluster[20]		[–4352.059071]	[–4352.071932]	[–4352.073387]	[–4352.091204]
Ethanolamine Conformers with Dihedral Angle	65.3.0° (E)	[–210.375309]	[–210.392562]	[–210.392937]	[–210.410336]
	177.6° (S)	[–210.372779]	[–210.390246]	[–210.390566]	[–210.408011]
	385.8°	[–210.369381]	[–210.386737]	[–210.387117]	[–210.404741]
ASC E1		–368.337014 [–4562.574671]	–342.072562 [–4562.594783]	–342.021903 [–4562.596590]	–327.516081 [–4562.626283]
ASC E2*		–262.356553 [–4562.534560]	–315.119783 [–4562.554656]	–319.602246 [–4562.556364]	–322.177704 [–4562.557345]
ASC E3		–233.255879 [–4562.523222]	–223.357717 [–4562.549567]	–223.306717 [–4562.551374]	–218.287956 [–4562.584680]
ASC E4*		–210.915683 [–4562.514967]	–279.791107 [–4562.541201]	–284.485921 [–4562.542989]	–303.444105 [–4562.550209]
ASC S1		–284.272468 [–4562.540123]	–267.361045 [–4562.564011]	–284.272468 [–4562.565847]	–255.374902 [–4562.596481]
ASC S2*		–262.312681 [–4562.531759]	–198.994259 [–4562.537972]	–199.017311 [–4562.539755]	–233.648365 [–4562.588205]
ASC S3		–231.627229 [–4562.520071]	–222.479672 [–4562.546917]	–222.592647 [–4562.548734]	–217.605089 [–4562.582095]
ASC S4*		–208.014663 [–4562.511078]	–198.994259 [–4562.537972]	–199.017311 [–4562.539755]	–203.059373 [–4562.576555]

Adsorption Energy (kJ mol^{-1}) [Total Energy (hartree)]	Basis Set			
	6-31G(d)	6-31+G(d)	6-31++G(d)	6-31++G(d,p)
ASC E5	–483.561124 [–4562.618558]	–460.351652 [–4562.639833]	–459.870437 [–4562.641476]	–442.797454 [–4562.670191]
ASC E6	–478.964688 [–4562.616807]	–455.775484 [–4562.638090]	–455.665121 [–4562.639874]	–438.856132 [–4562.668690]
ASC E7	–423.310284 [–4562.595610]	–397.990329 [–4562.616081]	–397.757986 [–4562.617819]	–381.223256 [–4562.646739]
ASC S5	–490.194844 [–4562.618554]	–466.427531 [–4562.639831]	–466.084090 [–4562.641475]	–448.874961 [–4562.670181]
ASC S6	–490.802962 [–4562.618786]	–465.463028 [–4562.639464]	–465.410255 [–4562.641218]	–448.411377 [–4562.670004]
ASC S7	–454.794860 [–4562.605071]	–428.058842 [–4562.625218]	–427.836646 [–4562.626907]	–411.082700 [–4562.655787]

* The unrestricted B3LYP functional has been used to take into account of the unpaired electrons in these ASCs.

3.2.2 XPS study of ethanolamine adsorption on Si(100)2×1 at room temperature

The XPS spectra of ethanolamine on Si(100)2×1 have been obtained for a number of room-temperature exposures (0.5 L, 2.5 L, 5 L, 10 L, 20 L, 50 L, 100 L, and 200 L). No discernible difference in the profile shape is found, which indicates that the adspecies are the same over the studied exposure range. Figure 3.3 shows representative O 1s, N 1s and C 1s spectra for a low (5 L) and a saturation exposures (100 L). Evidently, except for the lower overall intensities, the shapes of both the N 1s and C 1s spectra are essentially unchanged from the low exposure to the saturation exposure. Based on the reported literature values for N 1s BEs for the N−H dissociation adspecies (398.5-399.1 eV),[23−25,38−40] $-NH_2$ physisorbed (399.5-400.1 eV) and N dative bonded species (401.1-402.3 eV),[23−25,38−40] all on Si(100)2×1 surfaces, the single N 1s feature observed at 399.1 eV BE (with 1.6 eV FWHM) (Figure 3.3c, 3.3d) can be assigned to Si–N(H)−C≮. The present N 1s assignment is also in excellent agreement with the N 1s BEs for allylamine on Si(100)2×1 (398.9 eV)[20] and glycine on Si(111)7×7 (399.1 eV), for which dissociative N−H adsorption has been demonstrated.[36] The lower N 1s BE with respect to the terminal amino group commonly found at 399.5-402.3 eV BE[23−24,38−40] can therefore be used to rule out the presence of adspecies not involving N−H dissociation on the surface, i.e. unidentate O−H dissociation ASCs E1, E2, S1 and S2 (Figure 3.2). Furthermore, a single, broad O 1s peak (with 1.9 eV FWHM) is observed at 533.1 eV (Figure 3.3a, 3.3b), which is in good accord with the Si−O−C≮ moiety found for allyl alcohol and allyl aldehyde (532.6-532.7 eV)[18] and formamide (533.4 eV)[34] adspecies on Si(100)2×1. The O 1s feature therefore suggests the presence of O−H dissociation adspecies and the formation of Si−O bonds. However, given that the O 1s BE for an OH group is also commonly found in a similar binding energy range, the present spectrum cannot be used to rule out the presence of additional ASCs with the OH intact. In addition, the broad C 1s spectra (Figure 3.3e, 3.3f) can be fitted with two peaks at 284.8 eV and 285.7 eV BE (with 2.2 eV FWHM), which can be attributed to C_b−N and C_a−O bonds, respectively, with a unity intensity ratio expected for the stoichiometric ratio. The observed higher BEs can be used to rule out the presence of Si−C bonds, with BEs commonly found at 283.2-284.3 eV.[24,38,40] However, the observed BEs are somewhat lower than those reported in the literature for C−N (285.9-286.2 eV)[24,38,40] and C−O bonds (285.4-286.9 eV),[18,32,37] which suggests some form of electron delocalization in the adspecies (likely due to the formation of a

six-member ring found in the bidentate ASCs E5 and S5, as discussed further below). The ambiguity in the assignment of ASC using the room-temperature XPS spectra can be eliminated by considering the spectral evolution as a function of temperature discussed below.

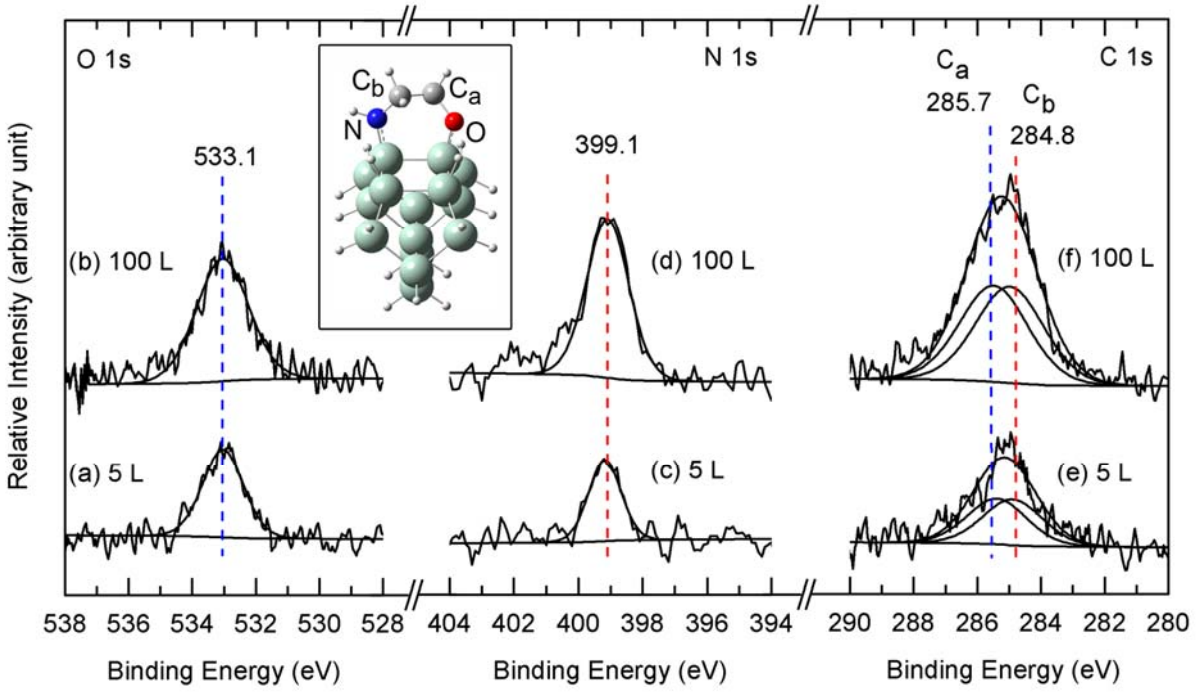

Figure 3.3 XPS spectra of O 1s (right), N 1s (center) and C 1s regions (left) for (a, c, e) a low (5 L) and (b, d, f) a saturation (100 L) exposures of ethanolamine on Si(100)2×1 at room temperature. The inset shows a plausible [O, N] bidentate adstructure with the methylene C atoms bonded to O (C_a) and N (C_b) appropriately identified.

3.2.3 Temperature-dependent XPS and TDS studies of thermal evolution products

XPS spectra of N 1s, C 1s and O 1s regions for a saturation (100 L) exposure of ethanolamine on Si(100)2×1 collected upon flash-annealing to different temperatures are shown in Figure 3.4. The corresponding intensities of individual fitted components, relative to the intensity of the Si 2p peak, are also shown as a function of flash-annealing temperature. Up to the flash-annealing temperature of 595 K, the N 1s feature for Si−N(H)−C< at 399.1 eV is found to be essentially unchanged in both intensity and spectral shape (Figure 3.4c). From 695 K to 890 K, the N 1s feature for Si−N(H)−C< has diminished completely, while a new feature at 397.7 eV BE emerges and becomes the dominant feature. The intensity of the latter feature remains effectively the same upon further flash-annealing to 1190 K. In accord with the N 1s BE for amino-containing molecules (397.2-397.8 eV) on Si(100) reported earlier,[23−25,38−40] the N 1s feature at 397.7 eV can be assigned to Si−NH, present either as a radical or bridge-bonded to a second Si atom as Si–N(H)–Si, resulting from C−N bond cleavage. The overall intensity of N 1s feature remains effectively unchanged up to the highest flash-annealing temperature (Figure 3.4d), which indicates predominant dissociative conversion of the Si−N(H)−C< moiety to Si−NH species (at 695-890 K) on the surface without any relevant N-containing desorbates, as shown by our TDS data below.

The O 1s spectrum (Figure 3.4a) appears to follow similar thermal evolution as the N 1s spectrum (Figure 3.4c). In particular, the O 1s peak at 533.1 eV remains stable in intensity and peak profile up to a flash-annealing temperature of 595 K, and it becomes totally diminished at 890 K while a new emerging feature at 532.0 eV, commonly assigned to Si−O−Si,[18,34] grows in intensity. The intensity of the latter feature remains unchanged up to 1090 K and becomes totally quenched at 1190 K (Figure 3.4b), likely due to diffusion of O into the bulk. Given that the bond dissociation energy follows the order: C−N (356 kJ mol^{-1}) < C−C (385 kJ mol^{-1}) < C−O (395 kJ mol^{-1}),[38] the appearance of Si−O−Si feature at 532.0 eV also marks the on-set of total fragmentation of the adspecies.

Unlike the N 1s and O 1s spectra, the thermal evolution of the corresponding C 1s spectral envelope is more complex. In particular, the C 1s band containing the C_b−N and C_a−O features (at 284.8 eV and 285.7 eV respectively) remains unchanged up to the flash-annealing

temperature of 595 K (Figure 3.4e), above which a discernible reduction in intensity is found. Between 595 K and 795 K (Figure 3.4e), the C 1s band undergoes major reduction in intensity and diminishes completely at 890 K. A new feature at 284.2 eV corresponding to C−C[39,40] emerges at 695 K and remains unchanged in intensity till 890 K, above which its intensity becomes completely reduced (at 995 K). At 795 K, the SiC feature at 283.2 eV[19,23−25,40] emerges and grows in intensity, becoming the dominant C 1s feature up to 1190 K. The 30% loss of total C 1s intensity at 595-795 K indicates desorption of C-containing fragments (likely ethylene as shown in our TDS data below). At 795 K, the remaining adspecies undergoes further dissociation likely first into C−C containing fragments and CH_2 fragments, followed by formation of SiC.

While we can rule out the unidentate O−H dissociation ASCs due to the lack of N 1s feature corresponding to terminal NH_2, we cannot distinguish between unidentate N−H dissociation ASCs (Figure 3.2c, 3.2d, 3.2g, 3.2h) and [O, N] bidentate ASCs (Figure 3.2i, 3.2j, 3.2k), based on the XPS data for the as-deposited samples (Figure 3.3). If the unidentate N−H dissociation ASCs were to occur, thermal evolution of such species would first undergo C−N bond cleavage at 595 K, producing a $-CH_2-CH_2OH$ fragment, which could either desorb or remain on the surface for further reactions. (The breakage of C−N bond is expected before that of C−C or C−O due to its lower bond dissociation energy.) The lack of any reduction in the O 1s intensity (Figure 3.4b) rules out the desorption route. The remaining $-CH_2-CH_2OH$ could only bind to the surface through Si−C bond formation or Si−O bond formation (i.e., involving O−H dissociation), which would give rise to, respectively, a C 1s feature at 283.0 eV or C 1s features at 286.5 eV (corresponding to Si−O−C$\not{-}$) at 695 K. The lack of these C 1s features at 695 K (Figure 3.4e) therefore eliminates the formation of unidentate N−H dissociation ASCs. The temperature-dependent C 1s spectra can be quite effective in identifying that the [O, N] bidentate ASCs are the only plausible ethanolamine adstructures on Si(100)2×1.

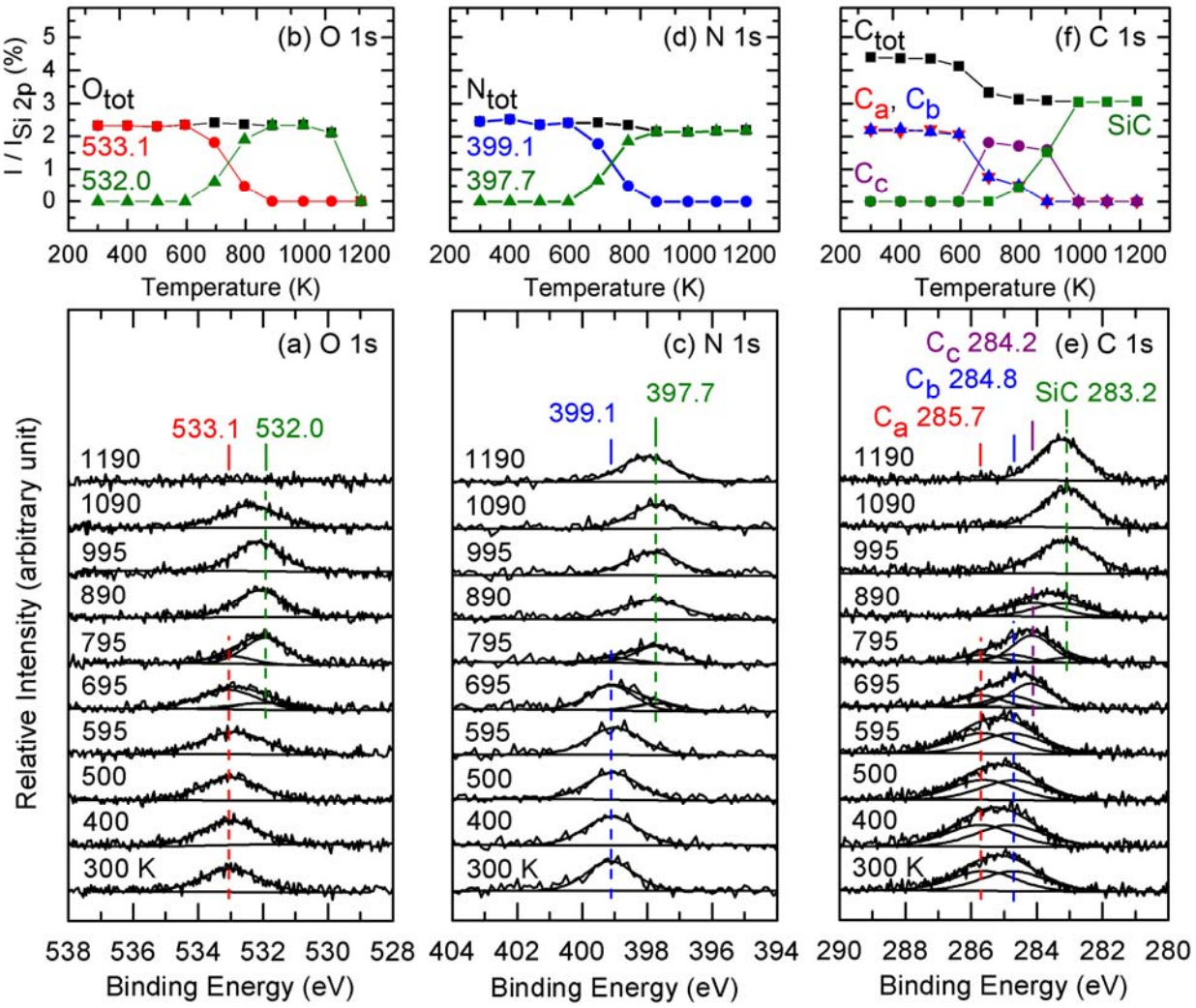

Figure 3.4 Temperature-dependent XPS spectra of (a) O 1s, (b) N 1s and (c) C 1s regions for a saturated exposure (100 L) of ethanolamine on Si(100)2×1 at (a) 300 K, and upon sequential flash-annealing to 400 K, 500 K, 595 K, 695 K, 795 K, 890 K, 995 K, 1090 K and 1190 K. Corresponding temperature profiles of the intensities of the (b) O 1s ($I_{O\ 1s}$)**,** (d) N 1s ($I_{N\ 1s}$**)** and (f) C 1s ($I_{C\ 1s}$) for Si−O–C≮ at 533.1 eV, Si−O−Si at 532.0 eV, Si−N(H)–C≮ at 398.9 eV, Si−N(H) at 397.7 eV, C_a at 285.7 eV, C_b at 284.8 eV, C_c at 284.2 eV, and SiC at 283.2 eV, along with their total intensities O 1s (O_{tot}), N 1s (N_{tot}) and C 1s (C_{tot}), all with respect to Si 2p ($I_{Si\ 2p}$).

To determine the desorption products thermally evolved from the adspecies remaining on the surface (as probed by the temperature-dependent XPS spectra in Figure 3.4), TDS experiments were performed. Figure 3.5 shows the TDS profiles of selected mass fragments of m/z 2, 26, 27, and 28 for a room-temperature saturation exposure (100 L) of ethanolamine on Si(100)2×1. It should be noted that we have also monitored, but found no detectable intensity, for other N-containing mass fragments, including m/z 17 (NH_3^+) and 30 ($CH_2NH_2^+$), corresponding to the parent mass of ammonia and to the base masses of ethanolamine and other fragments such as ethylamine and methylamine, respectively.[21] The lack of TDS signals from these fragments indicates that no N-containing species desorbs from the surface and that the N surface content is preserved. This result is in excellent accord with the effective constant total N 1s XPS intensity found up to the maximum flash-annealing temperature (1190 K) shown in Figure 3.4d, which confirms that the ethanolamine adspecies (with the N 1s feature at 399.1 eV BE) predominantly converts to Si–N(H)–Si (with N 1s feature at 397.7 eV BE) upon annealing (above 595 K). We also do not detect any TDS signals for m/z 31 (CH_2OH^+), which represents the O-containing mass fragment from ethanol and methyl alcohol.[21] The lack of any detectable TDS signals from O-containing fragments indicates O-containing species, like N-containing species, do not desorb from the surface up to the maximum desorption temperature used in the experiment (1190 K). This result is also in excellent agreement with the total O 1s XPS signal remaining unchanged up to 1090 K (Figure 3.4b), above which O diffusion into the bulk occurs. Finally, the lack of TDS signals for m/z 30 ($C_2H_6^+$) and m/z 25 (C_2H^+) can be used to exclude the formation of ethane and acetylene, respectively.[21]

Of the mass fragments that we obtain TDS profiles, the large desorption feature for m/z 2 observed at 780 K (Figure 3.5a) can be attributed to the recombinative desorption of H_2 from silicon monohydrides.[41] The remaining TDS feature for m/z 28, along with those TDS peaks for m/z 27 and m/z 26 at approximately half of its intensity (all at 615 K), corresponds to molecular desorption of ethylene, in excellent accord with the relative intensities of m/z 28 ($C_2H_4^+$, parent and base mass), m/z 27 ($C_2H_3^+$) and m/z 26 ($C_2H_2^+$) found in the cracking pattern of ethylene.[21] The desorption of ethylene therefore corresponds to the observed loss of C 1s intensities at 284.8 eV and 285.7 eV BE, between 595-695 K shown Figure 3.4f, which in turn confirms our earlier hypothesis that part of the adspecies desorbs as ethylene.

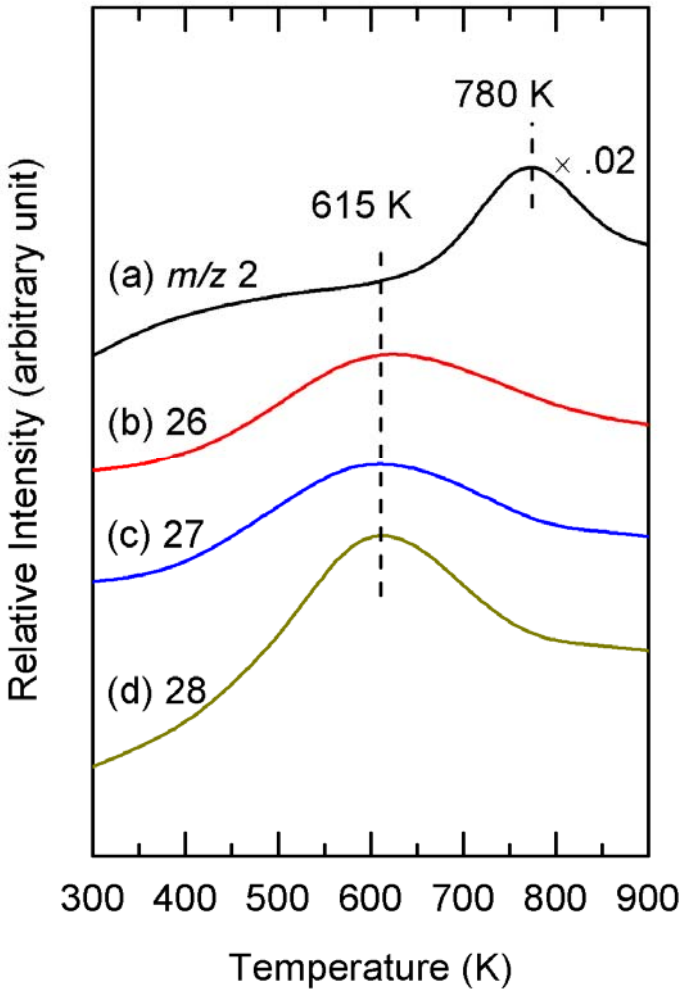

Figure 3.5 TDS profiles for selected mass fragments of m/z (a) 2, (b) 26, (c) 27, and (d) 28 for a saturation (100 L) exposure of ethanolamine on Si(100)2×1 at room temperature.

The formation of ethylene can be easily envisioned from the intra-dimer [O, N] bidentate ASC (Figure 3.2i) in a schematic pathway shown in Figure 3.6. In particular, the intra-dimer [O, N] bidentate ASC first undergoes a C–N bond cleavage to form Si–O–CH_2–CH_2• and Si–N(H)• radicals (Step a). The resulting Si–O–CH_2–CH_2• radical then undergoes a C–O bond cleavage, producing two other radicals, Si–O• and •CH_2–CH_2• (Step b), the latter of which becomes molecular ethylene CH_2=CH_2 (Step c). The remaining Si–N(H)• and Si–O• species further react with a neighboring Si atom, forming Si–N(H)–Si and Si–O–Si, while the Si monohydrides recombine to produce H_2 (Step d).

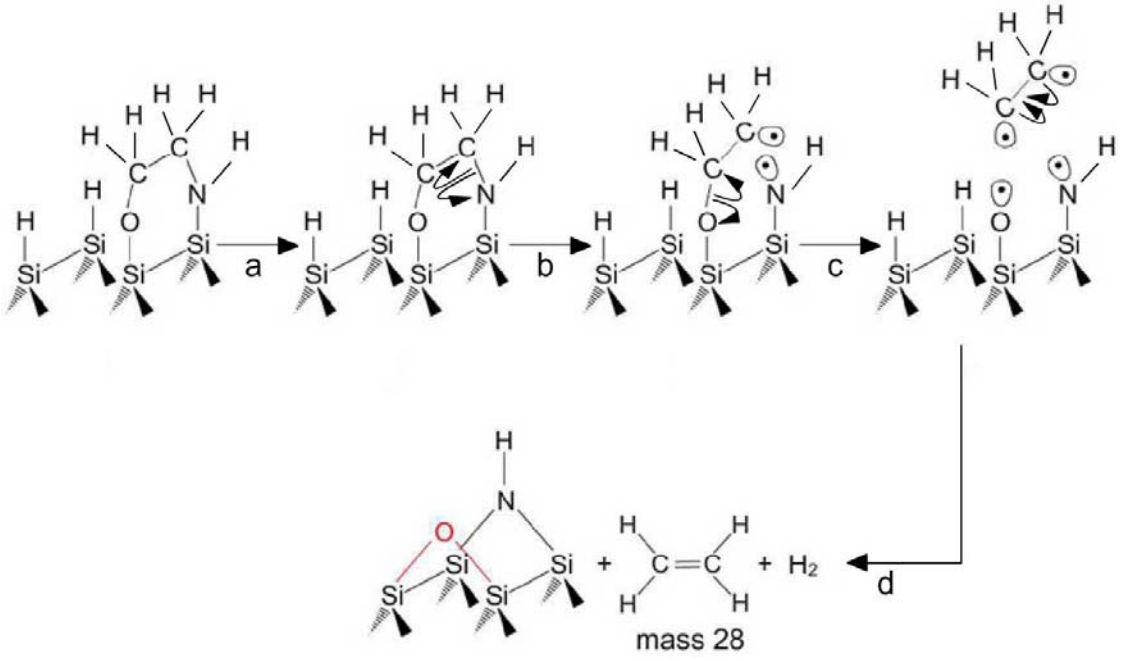

Figure 3.6 Schematic model for thermal evolution of an intra-dimer [O, N] bidentate adsorbate-substrate configuration (ASC), depicting a possible pathway for the formation of ethylene and H_2 as desorption products, along with Si–N(H)–Si and Si–O–Si as the surface species.

3.3 Concluding Remarks

In the present work, we have carried out temperature-dependent XPS and TDS experiments on the room-temperature adsorption of ethanolamine on Si(100)2×1. Detailed DFT calculations, involving both the eclipsed and staggered conformers of ethanolamine on a model surface based on the double-dimer $Si_{15}H_{16}$ cluster, have also been employed to interpret our data. Our XPS data show that room-temperature adsorption of ethanolamine on Si(100)2×1 leads to [O, N] bidentate adspecies, instead of the unidentate N–H and O–H dissociation adstructures. This result is in good accord with the previous work on the adsorption of the amino-containing and hydroxyl-containing molecules on Si(100), in which N–H dissociative adsorption through the amino group[23−24,38−40] and O−H dissociative adsorption through the hydroxyl group are found to be the primary processes, respectively.[2,29−33] In our earlier work on amino-containing molecule (allylamine),[20] we showed that the adsorption occurs by the cleavage of the N−H bond and the formation of Si−N bond. For O-containing molecules (allyl alcohol, allyl aldehyde,[18] acetic acid[42] and acrylic acid and propanic acids)[19] on Si(100)2×1, we show that adsorption proceeds through surface reactions of the hydroxyl,[18] carbonyl,[18] and carboxyl[19] groups, by forming O–Si bonds, with the ethenyl group remaining intact. The present work also shows that both the amino and the hydroxyl group react with the 2×1 surface through double N−H and O−H dissociation, respectively, forming N−Si and O−Si on the surface. The geometry of the molecule, specially the two ethanyl carbon atoms, enables the molecule to rearrange on the surface and bind through both of its ends forming a bridge of Si–O–C–C–N(H)–Si. The formation of a six-membered ring structure is in marked contrast to that found for formamide, which binds to the surface by forming Si−O bond, leaving the NH_2 group intact.[34] This difference could be attributed to the overall length of the respective adspecies. The formation of ethylene as the sole desorption product and the absence of N- or O-containing species up to temperature of 1190 K, indicate the high stability of the adsorbate on the surface, specially the Si−N and the Si−O species.

The formation of Si−N(H), Si−N and Si−O above 595 K is also confirmed by the presence of the respective N 1s and O 1s features in our temperature-dependent XPS study. Surface functionalization of Si(100)2×1 by ethanolamine therefore offers a number of interesting control opportunities, by first converting the double-bond of a Si dimer of the 2×1 surface to a

C−C bond of the “bridge” structure, creating a highly stable, passivation surface. The study of the competition between the adsorption of the hydroxyl and amino groups reveals that both are equally likely to occur on the surface. By annealing the functionalized hydrophobic surface to 890 K, the organic moiety is desorbed and the surface is transformed to a unique N- and O-terminated Si, with the atoms interchanged there position in a periodic fashion. This converts the hydrophobic carbon surface to a hydrophilic oxygen and nitrogen mixed surface. Such a conversion can be easily achieved by controlling the annealing temperature.

Finally, our DFT calculations were performed based on the double-dimer cluster, and confirm that the [O, N] bidentate adspecies as the preferred adstructure model with energies (–381.22-–448.87 kJ mol^{-1}) and the inter-dimer [O, N] bidentate with six-member ring complex as the most probable one.

Chapter 4

Nanoscale shape and size control of copper core-shell nanoparticles on H-Si(100) by a one-step electrochemical method: Diffusion-limited progressive growth of cubic, cuboctahedral and octahedral particles

4.1 Introduction

Between the two extremes of a single atom and the bulk, metallic nanoparticles (NPs) have many unique size-dependent properties, including quantum size effects, large surface area to volume ratios, and novel chemistry. As one of the best conductors of both heat and electricity, copper is used as a low-cost, versatile metal in many applications, including catalysis (for, e.g., methanol synthesis from CO_2 and H_2),[1] microelectronics (e.g., printed circuit boards, and wiring),[2] and fuel cells (e.g. by combining with other metals such as Pt to enhance the overall efficiency).[3] In addition, the oxides of copper, Cu_2O and CuO, also have numerous useful properties for catalysis,[1] fuel cells,[3] solar cells,[4] gas sensing,[5–7] and selective biofiltering for neutralizing and deactivating viruses.[8,9] To synthesize Cu NPs with well-defined morphology and chemical composition, both physical methods (including chemical vapour deposition,[10] and laser ablation)[11] and chemical methods (including sol-gel hydrothermal[12] and electrochemical deposition) [13] have been used. Indeed, the formation of Cu NPs and clusters on different substrates using a variety of different methods has been reported extensively in literature, and these substrates include organic and polymer surfaces,[14–23,35] metallic surfaces,[24,25] Si(100)[26,27] and Si(111)[28,29] surfaces.

Among the techniques used to grow Cu NPs, electrochemical deposition represents a low-cost, flexible, scalable method extensively used for growing NPs with definite morphology and chemical composition on a variety of substrates, including low-heat tolerant materials (e.g. plastics and polymers).[30] For example, Oskam et al. studied the nucleation and growth mechanism of Cu on n-type Si from sulfate solution, and they found that Cu undergoes progressive nucleation growth on the Si surface, forming islands according to the Wolmer-Weber model.[31] Grujicic and Pesic studied the nucleation of Cu on a glassy carbon substrate also in a sulfate solution, and they found that the pH, concentration of the copper electrolyte, deposition potential, temperature, and supporting electrolyte all influence the nucleation and growth of the NPs differently.[32] Ko et al. produced a triangular pyramidal Cu NPs on gold by using an organic capping reagent that limits the growth of the (111) plane,[34] while Li et al.

produced octahedral particles on gold surface.[25] In our previous studies, we studied the deposition of cubic Cu NPs on polypyrrole films electrochemically deposited on either a gold electrode,[22,23] or a gold film sputter-coated on p-type Si(100).[35] In these experiments, we found that the thickness of the polypyrrole film can be used to control the size and number density of the cubic Cu NPs.

For supported NPs, the morphology, number density, and chemical composition all play important roles in their reactivity and selectivity. Depending on the intended application of these NPs, a number of physical and chemical techniques have been developed to control different aspects of their properties.[23,29–35] One particularly important property is the NP shape, because the shape of the NP determines how many facets of specific orientation are exposed and therefore available for surface reactions. Given that some planes are more active than the others towards specific chemical reactions,[34] the shape of the NP can have a significant effect on its reactivity and selectivity. Cu NPs are found to exhibit several shapes including asymmetric triangular pyramidal shape with four (111) facets,[34] cubic with six (100) facets,[22] cuboctahedral with eight (111) and six (100) facets[36] and octahedral with eight (111) facets.[24] Since the surface energy of the solid is anisotropic, the shape of a NP is derived by exposing the limiting planes with the lowest free energies at specific concentration and temperature, while the other non-limiting planes grow faster and are not exposed.[37] Controlling factors that affect the growth kinetics of specific planes will therefore allow us to control the shape of the NP.

In the present work, we investigate the growth of Cu NPs electrochemically deposited on a H-terminated p-type Si(100) substrate. The chemical composition and the crystal structure of these Cu core-shell NPs have been characterized by depth-profiling X-ray photoelectron spectroscopy (XPS) and glancing-incidence X-ray diffraction (GIXRD). By varying the Cu electrolyte concentration and deposition time, Cu NPs with three well-defined shapes can be obtained with an average size range of 5-400 nm and a range of number densities.[35] The shape evolution as a function of electrolyte concentration can be qualitatively understood in terms of the interplay between the growth kinetics along different facet planes and the supersaturation factor.[37]

4.2 Results and Discussion

4.2.1 Shape control of Cu NPs electrodeposited on H-Si(100)

The deposition of metal NPs onto a support from a solution involves nucleation, followed by diffusion-limited growth, both of which affect the particle size distribution and number density.[31] The nature of both the metal and the support determine not only whether nucleation will be progressive or instantaneous but also whether the growth will follow the Frank-van der Merwe (layer-by-layer) or Volmer-Weber (island) or Stranski-Krastanov (mixed layer and island) growth mode.[21] It is well known that the nucleation of Cu on Si single crystals (both n-type and p-type) is progressive,[31] which is reflected by increasing number density with deposition time.[30,31] Cu NPs follow the Volmer-Weber growth mode due to the weak interaction between Cu and Si,[31] which results in increasing average particle size with deposition time. During the deposition process, the shape of the NP is known to be determined by the limiting planes with slower growth rates, which are the (100) and (111) planes for Cu.[37] The difference in the growth rates between the limiting planes causes specific facets to be exposed, producing the shape of the NP.[37] By choosing appropriate kinetic conditions that affect the growth rates of these limiting planes, it is possible to control the shape of the Cu NPs.

Figure 4.1 shows the SEM images of Cu NPs of specific shapes, obtained by electrodeposition at three different $CuSO_4 \cdot 5H_2O$ concentrations with appropriately chosen deposition time. At 10 mM [$CuSO_4 \cdot 5H_2O$], well-defined cubic Cu NPs of average size 100 nm were obtained (Figure 4.1a), while the shape of the Cu NPs becomes cuboctahedral with an average size of 150 nm at 100 mM (Figure 4.1b), and octahedral with an average size of 200 nm at 200 mM (Figure 4.1c). It should be noted that the deposition time does not affect the shape of the resulting NPs and is chosen here to provide better illustration of the homogeneous deposition at selected [$CuSO_4 \cdot 5H_2O$]. Furthermore, a continuous evolution in the shape of the NPs among these three observed shapes occurs among the key [$CuSO_4 \cdot 5H_2O$] concentrations at which the NPs of particular shapes are formed. For example, between 10 mM and 50 mM [$CuSO_4 \cdot 5H_2O$], NPs of truncated cuboctahedral shapes evolve from a primarily cubic shape at 10 mM to a largely cuboctahedral shape at 50 mM, resulting in a mixture of truncated cubic and cuboctahedral shaped NPs at different stages of growth.

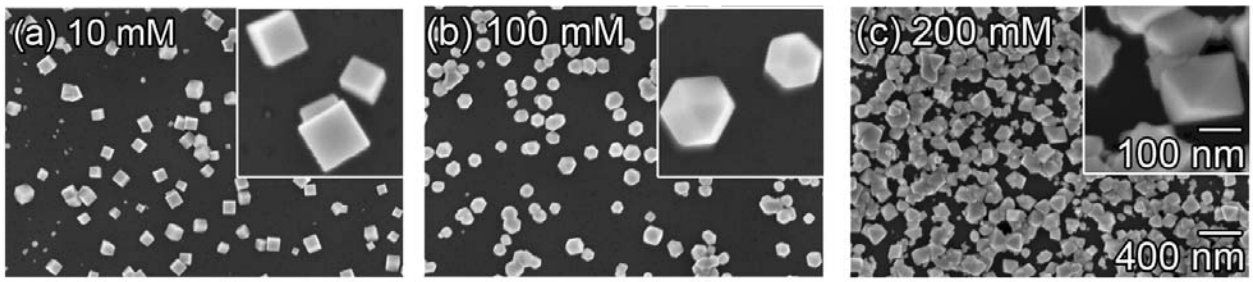

Figure 4.1 SEM images of Cu nanoparticles electrodeposited on H-Si(100) at –1.0 V in an aqueous solution of 10 mM [$NaClO_4$] and [$CuSO_4 \cdot 5H_2O$] of (a) 10 mM for 4 s, (b) 100 mM for 1 s and (c) 200 mM for 3 s, illustrating the cubic, cuboctahedral, and octahedral shapes of the nanoparticles, respectively.

In general, particles tend to grow in the directions of planes with a high surface free energy, in order to reduce the surface free energy for the NP by eliminating these planes.[37] The growth rate in the [110] direction for a NP is usually fast, because the (110) plane has the highest free energy.[37] The change in shape at different [$CuSO_4 \cdot 5H_2O$] concentrations is the result of changes in the growth rates in the [111] and [100] directions. At a low concentration (5-10 mM [$CuSO_4 \cdot 5H_2O$]), the growth rate of the emerging particle in the [111] direction is faster than that in the [100] direction, resulting in the exposure of the (100) facets. Since a face-centered cubic crystal has six (100) facets, the Cu NPs therefore appear cubic on average in this concentration range. By increasing the concentration to 50 mM, the growth rate in the [111] direction slows down and becomes comparable with that in the [100] direction. In this case, the (111) facets start to appear, along with the (100) facets. The cubic shape, with six (100) facets, first changes to truncated octahedron with six octagonal (100) facets and eight triangular (111) facets, and then to cuboctahedral with six square (100) facets and eight triangular (111) facets. At still higher concentrations to 200 mM, the growth rate of the NPs in the [100] direction exceeds that in the [111] direction, and the (111) facets become dominant. The particles become first truncated octahedral with (100) facets at the corners and (111) facets at the edges, then change to octahedral with eight (111) facets. Figure 4.2 summarizes the growth evolution of different shapes of NPs depending on the relative growth rates along the [100] and [111] directions.

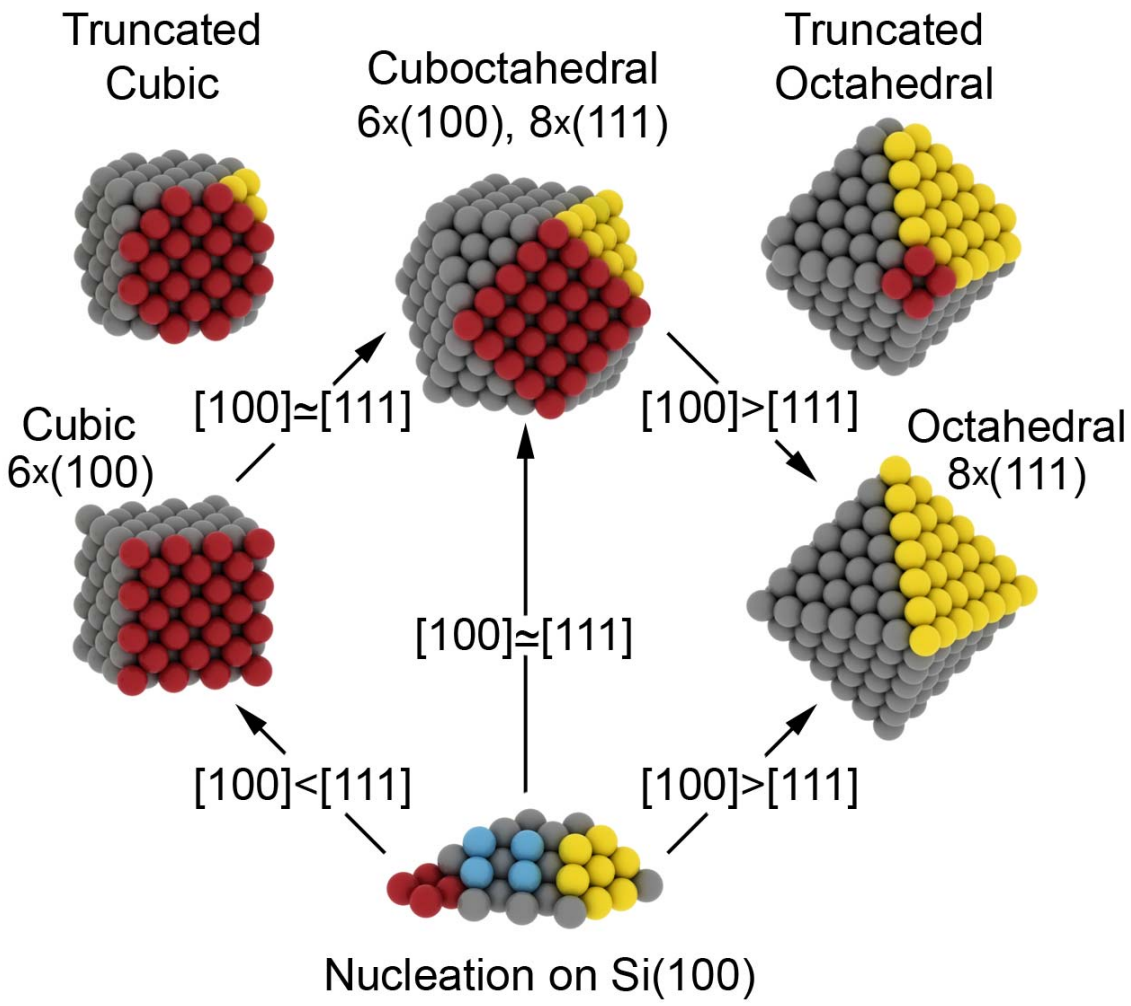

Figure 4.2 Schematic diagram of the shape evolution of Cu nanoparticles at different relative growth rates along the [100] and [111] directions.

4.2.2 Size and number density of Cu nanoparticles of specific shapes

For NPs of a particular shape obtained in a specific [$CuSO_4 \cdot 5H_2O$] range, it is possible to control the size distribution and number density by varying the deposition time. Figure 4.3 shows that both the average size and the number density of the cubic NPs obtained at 5 mM [$CuSO_4 \cdot 5H_2O$] increase with increasing deposition time. From 0.1 s to 0.5 s deposition time, the NPs increase in size from 20 nm with a wide size range of 0-40 nm (Figure 4.3a) to 30 nm with a range of 10-50 nm (Figure 4.3b). Increasing the deposition time to 1.0 s and 2.0 s causes the average size to increase to 30 nm and 40 nm, respectively, with a size range of 5-60 nm and 10-70 nm (Figure 4.3c, 4.3d). Above 2.0 s deposition time (Figure 4.3e, 4.3f), the average size remains effectively unchanged as the particle approaches the average optimal size of 40 nm. The corresponding size distribution evidently becomes narrower, i.e. the particles become more uniform in size (from 15-65 nm for 3.0 s to 25-65 nm for 4.0 s). Further increase in the deposition time causes the particles to cluster and coalescence producing a thin film (not shown). As shown in Figure 4.4, similar dependence of the particle size on the deposition time can also be observed for NPs with different shapes obtained at different [$CuSO_4 \cdot 5H_2O$], i.e. among cubic (10 mM), cuboctahedral (50 mM) and octahedral shapes (200 mM) NPs. In addition, the number density of NPs is also found to increase with increasing deposition time, as shown for cubic NPs in Figure 4.3. For a longer deposition time, the number density will increase until the NPs start to coalescence to bigger NPs, as found in Ostwald ripening (and eventually to form a film). These changes are illustrated for cuboctahedral NPs in Figure 4.5, and they are consistent with progressive nucleation of the Cu NP growth on H-Si(100).

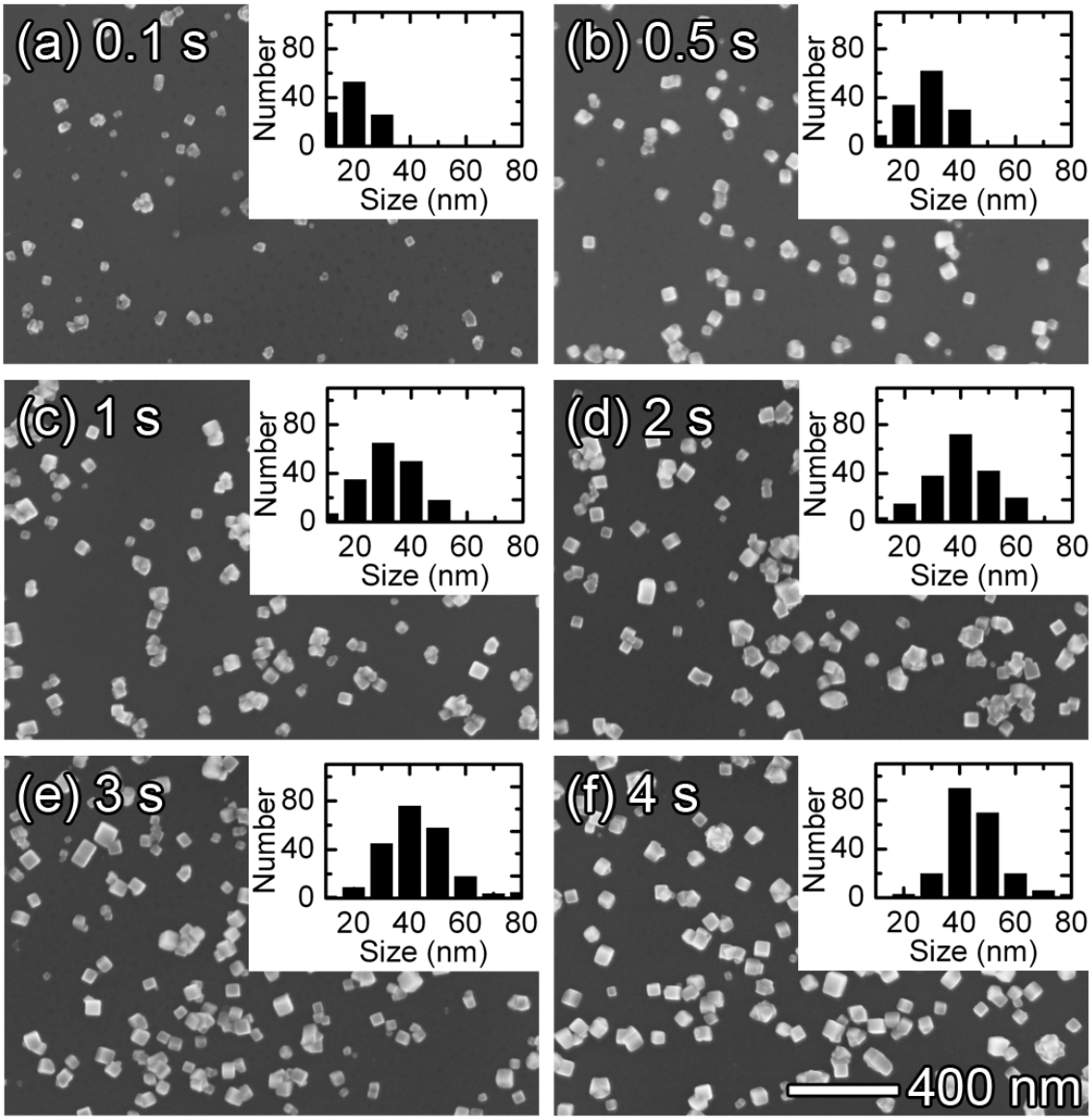

Figure 4.3 SEM images of Cu nanoparticles electrodeposited on H-Si(100) at –1.0 V in an aqueous solution of 5 mM [$CuSO_4 \cdot 5H_2O$] (and 10 mM [$NaClO_4$]) for deposition times of (a) 0.1 s, (b) 0.5 s, (c) 1 s, (d) 2 s, (e) 3 s, and (f) 4 s.

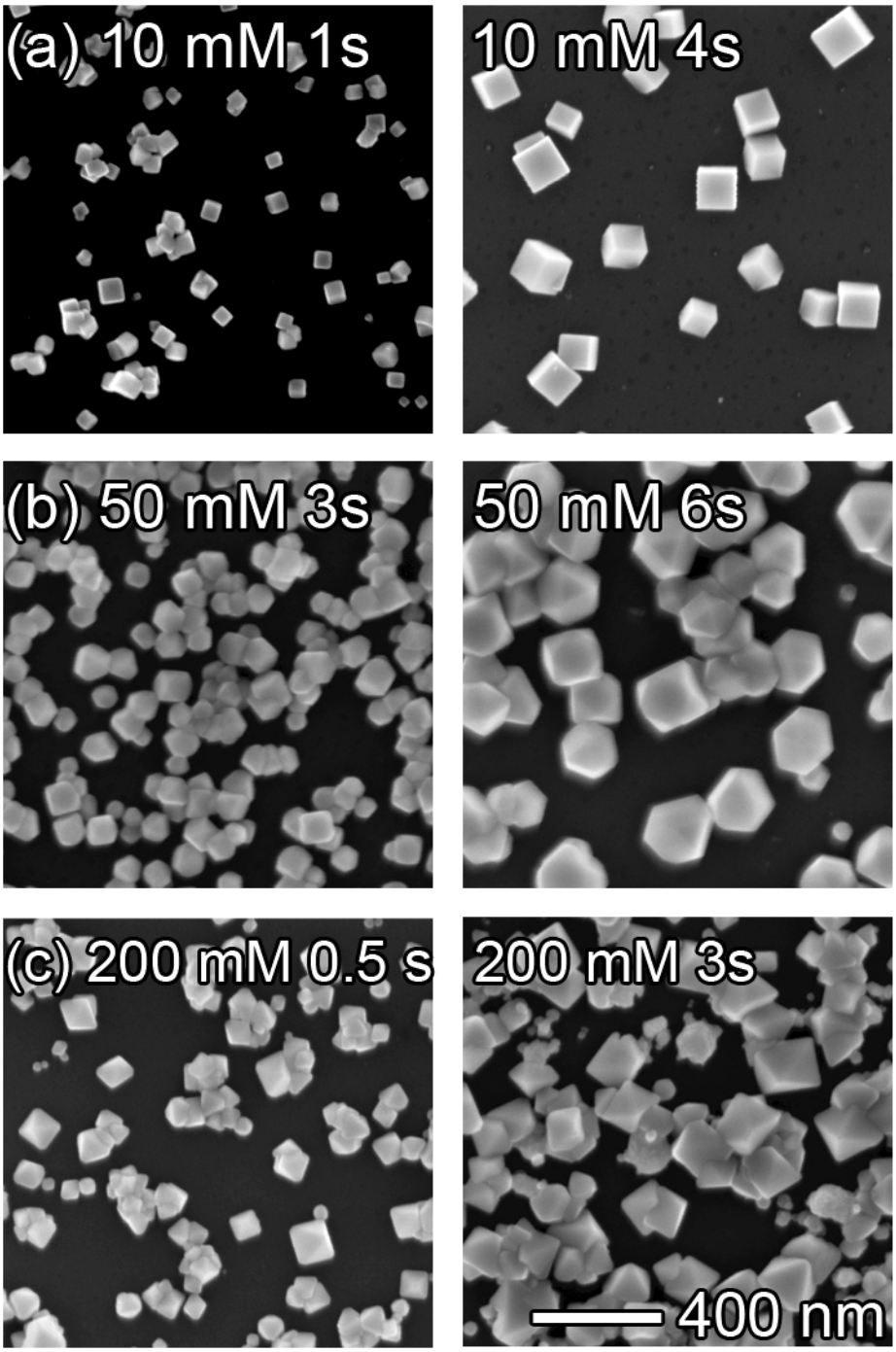

Figure 4.4 SEM images of Cu nanoparticles electrodeposited on H-Si(100) at –1.0 V in an aqueous solution of (a) 10 mM, (b) 50 mM and (c) 200 mM [$CuSO_4 \cdot 5H_2O$] (and 10 mM [$NaClO_4$]), each for two different deposition times.

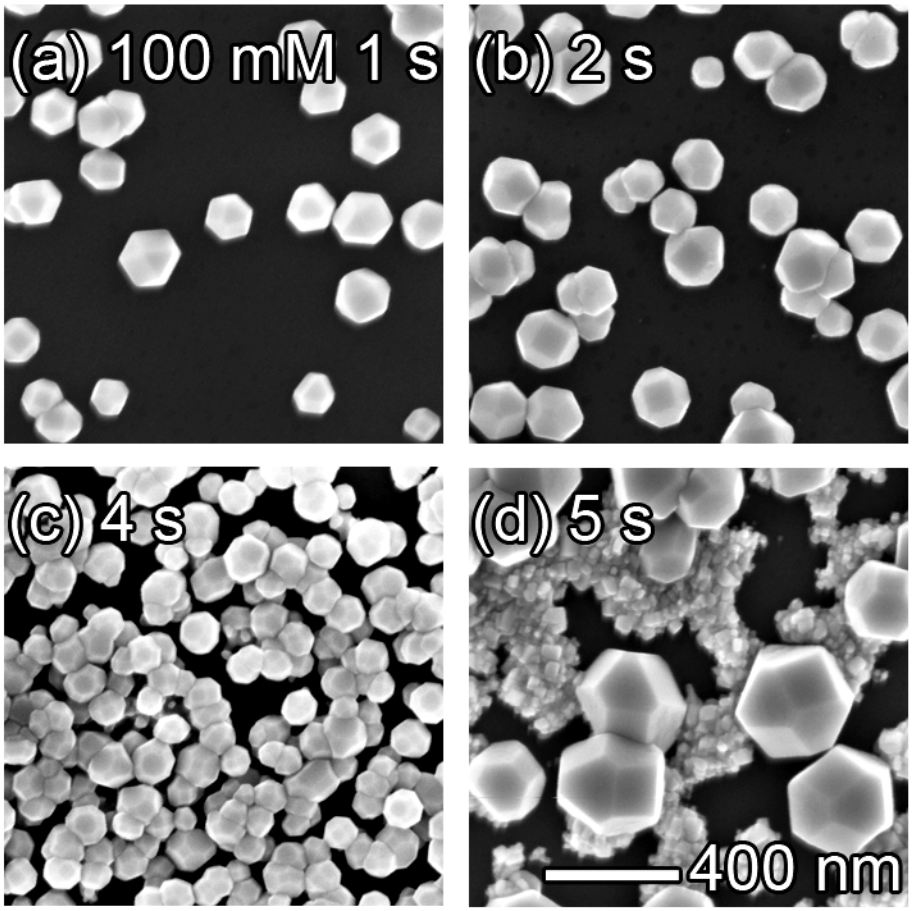

Figure 4.5 SEM images of Cu nanoparticles electrodeposited on H-Si(100) at –1.0 V in an aqueous solution of 100 mM [$CuSO_4 \cdot 5H_2O$] (and 10 mM [$NaClO_4$]) for deposition times of (a) 1 s, (b) 2 s, (c) 4 s, and (d) 5 s.

The dependence of the NP size can be understood in terms of the supersaturation factor, which is defined as the ratio of the actual pressure experienced by the growing particle at a particular size to that at the optimum size at specific concentration and temperature.[37] If the supersaturation factor is greater than 1, the NP will continue to grow until it reaches the optimum size with a unity factor, at which point the particle stops to grow. By increasing the deposition time, the amount of charge transfer increases, increasing the particle size, which in turn causes the surface area to increase and the pressure to decrease. As a result, the supersaturation factor

decreases and becomes closer to one, with the particle size approaching the optimum size for that concentration. Because the nucleation process of Cu NPs on the Si surface is progressive, new nucleation sites are created continuously (as long as there is open space on the substrate), increasing the number density, during the electrodeposition process. The NPs that nucleate first will therefore have the largest size and they will reach the optimum size first and stop growing. As the deposition continues, nucleation of the NPs will eventually cover the entire surface, saturating the number density and limiting further creation of new particles. The size distribution will become narrower if sufficient deposition time is allowed for all the nucleated particles to grow bigger and reach the optimum size, as illustrated in Figure 4.3. When most of the particles reach the optimum size at a specific concentration, further deposition will cause the particles to coalescence, producing Oswald ripening and/or film formation, as shown in Figure 4.5.

4.2.3 Crystal structure and chemical composition

Figure 4.6 shows a typical GIXRD pattern for cuboctahedral Cu NPs obtained at 100 mM [$CuSO_4 \cdot 5H_2O$] for 1 s (Figure 4.5a). The prominent peaks at 29.56°, 36.42°, 42.30°, 61.35° and 73.53° correspond, respectively, to the (110), (111), (200), (220) and (311) of simple cubic Cu_2O (with space group Pn–3m, JCPDS 00-005-0667),[38] while the weaker features at 43.30° and 50.43° can be assigned, respectively, to (111) and (200) of face-centered cubic Cu (with space group Fm–3m, JCPDS 00-004-0836).[38] GIXRD measurements have also been obtained for Cu NPs of cubic and octahedral shapes and are found to give similar results (not shown), which confirm similar crystal structures for the Cu NPs of different shapes. Other features found in the 53-58° range can be attributed to the Si substrate and associated amorphous Si oxides.

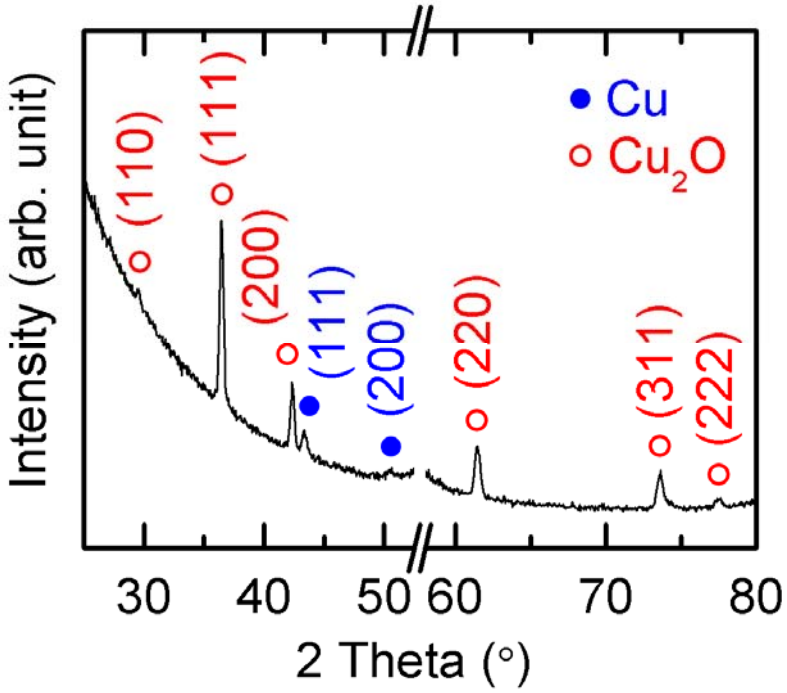

Figure 4.6 Glancing-incidence XRD pattern of cuboctahedral Cu nanoparticles electrodeposited on H-Si(100) at –1.0 V in an aqueous solution of 100 mM [$CuSO_4 \cdot 5H_2O$] (and 10 mM [$NaClO_4$]) for 1 s deposition time.

Figure 4.7 shows typical XPS spectra for Cu $2p_{3/2}$ and O 1s regions at different sputtering times for cubic Cu nanoparticles obtained at 10 mM [$CuSO_4 \cdot 5H_2O$] for 4 s (Figure 4.4a). For the as-deposited sample, the peak at 932.6 eV can be attributed to Cu_2O, in accord with the literature data.[39,40] The presence of a very weak but discernible Cu $2p_{3/2}$ peak at 934.0 eV (Figure 4.7) and its satellite peak at 942.0 eV (not shown) can be assigned to CuO.[41] This layer is evidently removed after a short sputtering of 30-60 s, which indicates the presence of a thin layer of CuO. The marked increase in the intensity of the Cu_2O feature at 932.6 eV after 30 s of sputtering could be due to removal of a carbonaceous layer often found in sample handling under ambient conditions. The spectrum remains unchanged after further sputtering for 240 s, above which peak broadening and intensity reduction are observed. After 500 s of sputtering, we observe the emergence of additional intensity at 932.9 eV (i.e., 0.3 eV higher in binding energy than the Cu_2O feature), corresponding to metallic Cu.[39,40] The presence of the metallic Cu feature is better illustrated in the corresponding Cu LMM Auger spectra (Figure 4.7, inset). In particular,

the metallic Cu Auger feature at 918.0 eV kinetic energy[39,40] is clearly evident after sputtering for just 60 s and this metallic feature becomes more intense with further sputtering while the corresponding Cu_2O Auger feature at 916.0 eV kinetic energy[39,40] weakens. The Cu Auger spectra therefore confirm that the Cu nanoparticle consists of a metallic Cu core and a Cu_2O shell with a thin outerlayer of CuO as indicated in the XPS spectra.

The corresponding O 1s spectrum for the as-deposited sample shows two peaks at 532.4 eV and 530.3 eV, attributed to amorphous silicon oxide (SiO_x) and Cu oxides (Cu_2O/CuO), respectively.[42−44] The presence of the strong SiO_x O 1s feature is due to in-solution oxidation of the Si surface not covered by the Cu NPs during the electrodeposition process. After 30 s of sputtering, the SiO_x feature is significantly reduced, making the Cu-oxide feature at 530.3 eV more evident. Further sputtering reduces the intensities of both features, with complete removal of the Cu-oxide features after 500 s. The remaining intensity at 532.4 eV corresponds to oxygen inside the bulk Si. It should be noted that after the complete removal of the Cu-oxide O 1s feature at 530.3 eV, considerable intensity for the Cu $2p_{3/2}$ feature at 932.9 eV is clearly observed. This marks the complete removal of the Cu_2O shell, and the presence of Cu NPs with just the metallic Cu core. It should also be noted that the small shift in Cu $2p_{3/2}$ binding energy found for the metallic Cu core could also indicate a quantum size effect. In particular, the depth-profiling XPS measurement for a Cu film on Si(100) by Pazti et al.[17] shows that the Cu $2p_{3/2}$ peak broadens and shifts by 0.4 eV, which they attributed to a quantum size effect. In a separate study, we also observe a similar binding energy shift with increasing sputtering (i.e. decreasing particle size) and these results will be discussed elsewhere.[45] Finally, we also find similar depth profiles for cuboctahedral and octahedral Cu NPs obtained with different deposition conditions, which confirms the "universal" core-shell nature of these electrochemically deposited Cu NPs.

On the basis of the GIXRD and depth-profiling XPS data, we propose a general core-shell model, shown in Figure 4.8, for the Cu NPs of different shapes and crystal structures electrodeposited on H-Si(100).

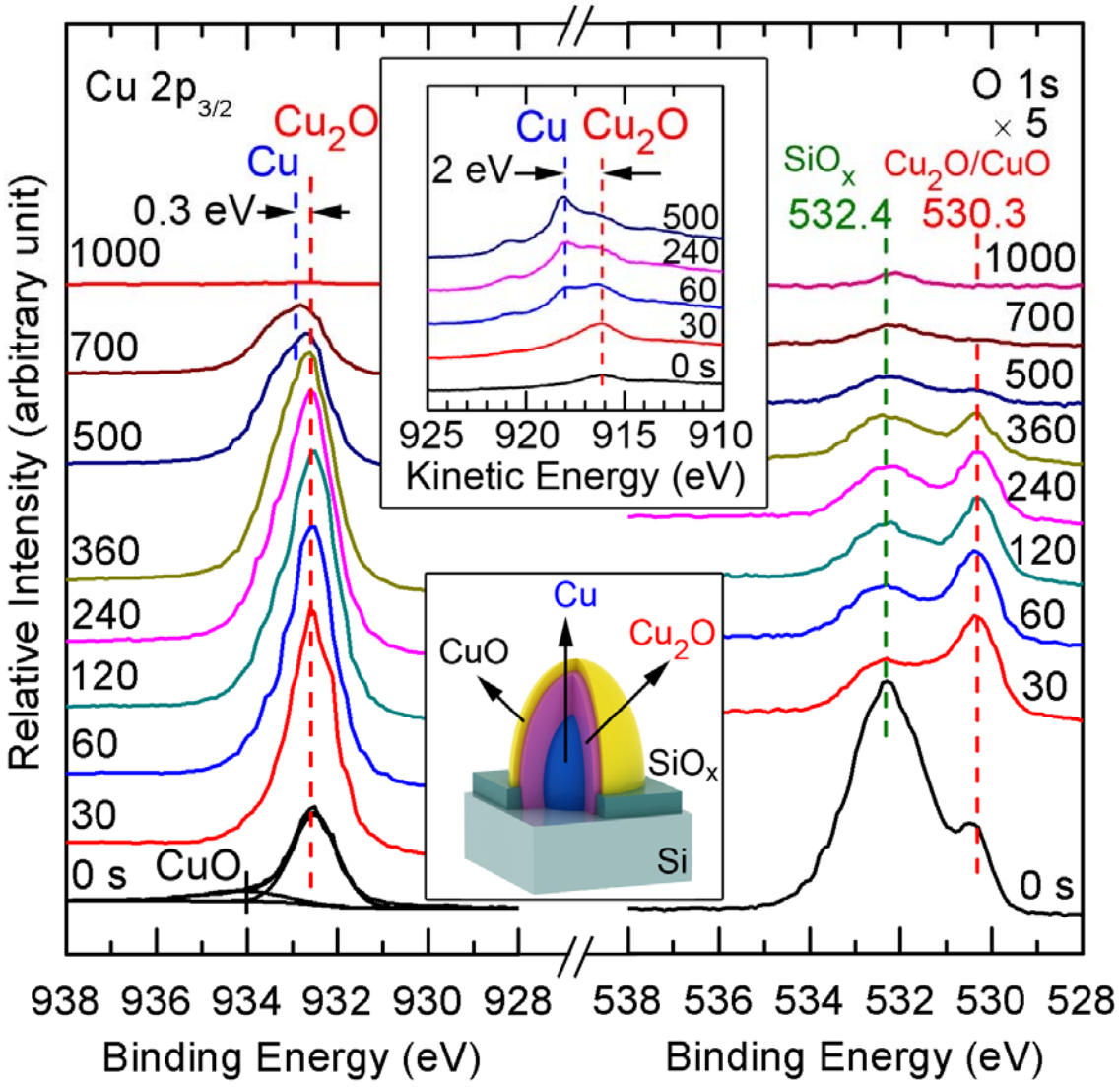

Figure 4.7 XPS spectra of Cu $2p_{3/2}$ and O 1s regions of cubic Cu nanoparticles electrodeposited on H-Si(100) at –1.0 V in an aqueous solution of 10 mM [$CuSO_4 \cdot 5H_2O$] (and 10 mM [$NaClO_4$]) for 4 s deposition time, and upon sputtering for selected times. The insets show the corresponding Cu LMM Auger features, and a schematic model of the core-shell Cu nanoparticle.

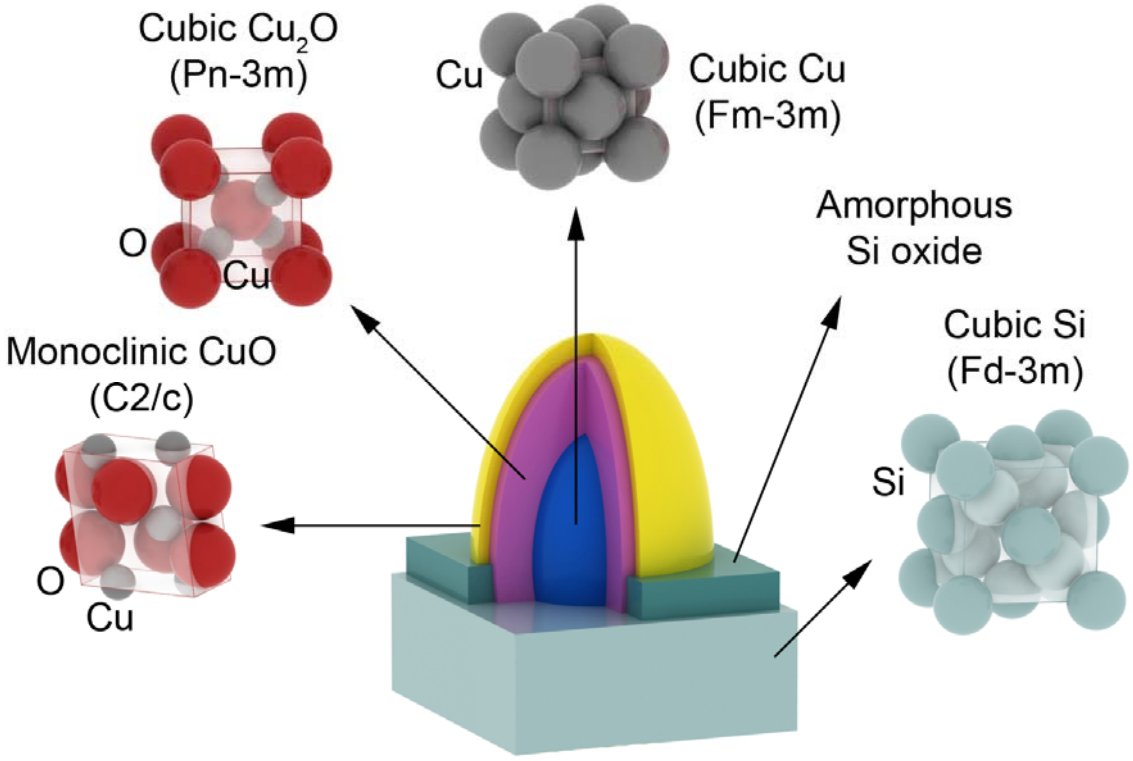

Figure 4.8 A schematic model for Cu nanoparticles electrodeposited on Si(100), depicting the metallic Cu core and Cu_2O shell with a CuO outerlayer. This model is based on the crystallographic data of Refs. [46, 47, 48, 49].

4.3 Concluding Remarks

The present work shows that Cu NPs of cubic, cuboctahedral, octahedral shapes can be obtained by a one-step electrochemical method using the [$CuSO_4 \cdot 5H_2O$] concentration as the control parameter. In particular, cubic NPs with six (100) facets, cuboctahedral NPs with six (100) facets and eight (111) facets, and octahedral NPs with eight (111) facets can be obtained with 5-10 mM, 50-100 mM, and 200 mM [$CuSO_4 \cdot 5H_2O$], respectively. A continuous evolution in the shape with truncated crystal structures among these three primary shapes can also be observed at intermediate [$CuSO_4 \cdot 5H_2O$] concentrations. Furthermore, the size and number density of these Cu NPs with specific shapes can also be easily controlled by the deposition time at selected [$CuSO_4 \cdot 5H_2O$] concentrations. Evolution of the average size and distribution, up to a critical dimension, can be understood in terms of the supersaturation factor in the diffusion-limited progressive growth model. Using GIXRD and depth-profiling XPS, we also determine that these Cu NPs, regardless of shapes, consist of a crystalline metallic Cu core and a Cu_2O shell with a thin CuO outerlayer. The ability to control the relative populations of different (100) and (111) facets over a full range of Cu NPs of different shapes supported on Si(100) provides new opportunity to develop site-specific surface chemistry in emerging applications.

Chapter 5
Summary and Outlook

In the present work, we have carried out two studies: a surface science study on the biofunctionalization of allylamine and ethanolamine on Si(100)2×1, and a materials science study for the synthesis Cu nanoparticles (NPs) with controllable shapes on Si(100) by a one-step, electrochemical method. The main objectives of these projects were to inter-compare the relative reactivities of ethenyl, amino and hydroxyl groups in bifunctional organic molecules adsorbed on the 2×1 surface, and to control the relative amount of different exposed surfaces of the resulted nanoparticles by controlling their shapes. in order to prepare them for future surface functionalization studies.

In the first study, temperature-dependent XPS and TDS experiments on the room-temperature adsorption of allylamine and ethanolamine on Si(100)2×1 were conducted, along with detailed DFT calculations, involving the conformers of both molecules on a model surface based on the double-dimer $Si_{15}H_{16}$ cluster. Along with earlier work on allyl alcohol, we characterized the relative reactivities among the ethenyl, hydroxyl and amino groups in bifunctional organic molecules adsorbed on Si(100)2×1. The corresponding XPS spectra revealed that amino and hydroxyl groups are more reactive on the 2×1 surface than the ethenyl group which remains intact, as indicated by the N−H and O−H dissociative unidentate adstructures, respectively, for allylamine and allyl alcohol. Between the hydroxyl and the amino groups, the results of the adsorption of ethanolamine revealed no notable difference in the relative reactivity as ethanolamine adsorbs through both N−H and O−H dissociation, forming a bridge-like adstructure. In the DFT calculations, we presented new systematic approaches in constructing both the Si double-dimer cluster and the different conformers of the free molecules, in order to improve the accuracy of calculated adstructures. Our DFT calculations supported the XPS results and showed the different plausible pathways as the molecule adsorbs onto the surface, providing qualitative insights into the thermodynamics and kinetics of adsorption on the surface. The thermal evolution study illustrated the strengths of the Si−N and Si−O bonds, as no N- or O-containing desorbates from the surface and only propene, ethylene and acetylene for allylamine and ethylene for ethanolamine were found.

In the second study, we showed that Cu NPs of cubic, cuboctahedral, octahedral shapes can be obtained by a one-step electrochemical method using the [$CuSO_4 \cdot 5H_2O$] concentration as the primary control parameter. In particular, cubic NPs with six (100) facets, cuboctahedral NPs with six (100) facets and eight (111) facets, and octahedral NPs with eight (111) facets could be obtained with 5-10 mM, 50-100 mV, and 200 mM [$CuSO_4 \cdot 5H_2O$], respectively. Furthermore, the size and number density of these Cu NPs with specific shapes could also be easily controlled by the deposition time at selected [$CuSO_4 \cdot 5H_2O$] concentrations. These results would allow us to develop well defined nanoparticles with controlled shapes and sizes that govern the relative amounts of (100) and (111) surfaces, in addition to their surface coverages through manipulation of their number density. A detailed analysis of the crystal structure and chemical composition of these Cu NPs was also made by using GIXRD and depth-profiling XPS, respectively. These results showed that Cu NPs, regardless of shapes, consisted of a crystalline metallic Cu core and a Cu_2O shell with a thin CuO outerlayer.

The next stage to go beyond the present work will involve two more projects: biofunctionalization of the two Cu single-crystal surfaces, particularly the (111) and (100) surfaces, with allylamine and ethanolamine; and, finally, biofunctionalization of the Cu NPs of controlled shapes as deposited on Si(100) by these molecules. The latter project will combine all the results of the previous projects to develop a deeper understanding of the nature of adsorption on the surfaces of these fascinating metallic nanoparticles. These studies will facilitate further insights into new phenomena associated with the reactions of the nanoparticles and the effects of their shape and size on the reactivity of the surface.

References

Chapter 1

[1] S. Carniato, J. Gallet, F. Rochet, G. Dufour and F. Bournel, Phys. Rev. B 76 (2007) 085321.

[2] L. Zhang, A. J. Carmen, S. Casey, J. Phys. Chem. B 107 (2003) 8424.

[3] S. Bent, J. Phys. Chem. B 106 (2006) 2830.

[4] H. Nakatsuji, Z. Hu, Int. J. Quantum Chem. 77 (2000) 341.

[5] M. Stutzmann, J.A. Garrido, M. Eickhoff, M. S. Brandt, Phys. Status Solidi A 14 (2006) 3424.

[6] J. Iijima, J. Lim, S. Hong, S. Suzuki, K. Mimura, M. Issiki, Appl. Surf. Sci. 253 (2006) 2825.

[7] J. Lee, J. Choi, S. Kang, J. Lee, Y. Tak, J. Lee, Electrochim. Acta 52 (2007) 2272.

[8] K. Akimoto, S. Ishizuka, M. Yanagita, Y. Nawa, G. Paul, T. Sakurai, Sol. Energy 80 (2006) 715.

[9] J. Tamaki, K. Shimanoe, Y. Yamada, Y. Yamamoto, N. Miura, N. Yamazoe, Sens. Actuators B 49 (1998) 121.

[10] X. Miao, R. Yuan, Y. Chai, Y. Shi, Y. Yuan, J. Electroanal. Chem. 612 (2008) 157.

[11] T. Ishihara, M. Higuchi, T. Takagi, M. Ito, H. Nishiguchia, Y. Takitaa, J. Mater. Chem. 8 (1998) 2037.

[12] G Borkow, R. Sidwell, D. Smee, D. Barnard, J. Morrey, H. Lara-Villegas, Y. Shemer-Avni, J. Gabbay, Antimicrob. Agents Chemother. (2007) 2605.

[13] G. Borkow, H. Lara, C. Covington, A. Nyamathi, J. Gabbay, Antimicrob. Agents Chemother. (2008) 518.

[14] X. Wang, R. Zhang, T Niehaus, T. Frauenheim, J. Phys. Chem. C 111 (2007) 2394.

[15] Z. Zhu, A. Srivastava, R. M. Osgood Jr, J. Phys. Chem. B 107 (2003) 13939.

[16] J. Zhu, M. Yudasaka, M. Zhang, D. Kasuya, S. Iijima, Nano Lett. 3 (2003) 9.

[17] M. Voue, E. Goormaghtigh, F. Homble, J. Marchand-Brynaert, J. Conti, S. Devouge, J. De Coninck, Langmuir 23 (2007) 949.

[18] O. Veiseh, C. Sun, J. Gunn, N. Kohler, P. Gabikian, D. Lee, N. Bhattarai, R. Ellenbogen, R. Sze, A. Hallahan, J. Olson, M. Zhang, Nano Lett. 5 (2005) 6.

[19] H. Haick, D. Cahen, Acc. Chem. Res. 41 (2008) 359.

[20] G. Celotti, D. Nobili, P. Ostoja, J. Mater. Sci. 9 (1974) 821.

[21] C. Duke, Chem. Rev. 96(4) (1996) 1237.

[22] W. Kern, D. A. Puotinen, RCA Rev. 31 (1970) 187.

[23] J. Li, Y. Qu, K. Han, G. He, Surf. Sci. 586 (2005) 45.

[24] J. Yoshinobu, Prog. Surf. Sci. 77 (2004) 37.

[25] R. A. Wolkow, Phys. Rev. Lett. 68 (1992) 2636.

[26] T. R. Leftwich, A. V. Teplyakov, Surf. Sci. Rep. 63 (2008) 1.

[27] X. Lu, M. C. Lin, Int. Rev. Phys. Chem. 21 (2002) 137.

[28] M. A. Filler, S. F. Bent, Prog. Surf. Sci. 73 (2003) 1.

[29] S. F. Bent, Surf. Sci. 500 (2002) 879.

[30] F. A. Carey, "Organic Chemistry", 3rd Edition, McGraw-Hill, Toronto, 1996.

[31] J. B. Wu, Y. Yang, Y. F. Lin, H. T. Chiu, J. Phys. Chem. B 108 (2004) 1677

[32] X. Cao, R. Hamers, J. Phys. Chem. B. 106 (2002) 1840.

[33] E. K. Hlil, L. Kubler, J. L. Bischoff, D. Bolmont, Phys. Rev. B 35 (1987) 5913.

[34] X. Cao, R. Hamers, J. Vac. Sci. Technol. B 20 (2002) 4.

[35] X. Cao, R. Hamers, J. Am. Chem. Soc. 123 (2001) 10988.

[36] Th. Kugler, U. Thibaut, M. Abraham, G. Folkers, W. Gopel, Surf. Sci. 260 (1992) 64.

[37] C. Shannon, A. Campion, Surf. Sci. 227 (1990) 219.

[38] J. Eng Jr., K. Raghavachari, L. M. Struck, Y. J. Chabal, B. E. Bent, G. W. Flynn, S. B. Christman, E. E. Chaban, G. P. Williams, K. Radermacher, S. Mantl, J. Chem. Phys. 106 (1997) 9889.

[39] J. Kim, K. Kim, K. Yong, J. Vac. Sci. Technol. A 20 (2002) 1582.

[40] J. W. Kim, M. Carbone, M. Tallarida, J. H. Dil, K. Horn, M. P. Casaletto, R. Flammini, M. N. Piancastelli, Surf. Sci. 559 (2004) 179.

[41] M. P. Casaletto, R. Zanoni, M. Carbone, M. N. Piancastelli, L. Aballe, K. Weiss, K. Horn, Surf. Sci. 505 (2002) 251.

[42] M. Ebrahimi, J. M. Chong, K. T. Leung, (2009) submitted.

[43] G. Oskam, J. Long, A. Natarajan, P. Searson, J. Phys. D 31 (1998) 1927.

[44] Y. C. Liu, K. H. Yang, M. D. Ger, Synth. Met. 126 (2002) 337.

[45] M. R. Guascito, P. Boffi, C. Malitesta, L. Sabbatini, P. G. Zambonin, Mater. Chem. Phys. 44 (1996) 17.

[46] N. Cioffi, L. Torsi, I. Losito, C. D. Franco, I. D. Bari, L. Chiavarone, G. Scamarcio, V. Tsakova, L. Sabbatini, P. Zambonin, J. Mater. Chem. 11 (2001) 1434.

[47] Z. Pászti, G. Petö, Z. E. Horváth, A. Karacs, J. Phys. Chem. B 101 (1997) 2109.

[48] L. Makhloufi, H. Hammache, B. Saidani, N. Akilal, Y. Maloum, J. Appl. Electrochem. 30 (2000) 1143.

[49] V. Tsakova, D. Borissov, B. Ranguelov, C. Stromberg, J.W. Schultze, Electrochim. Acta 46

(2001) 4213.

[50] V. Tsakova, D. Borissov, Electrochem. Comm. 2 (2000) 511.

[51] C. Ji, G. Oskam, P.C. Searson, Surf. Sci. 492 (2001) 115.

[52] D. K. Sarkar, X. J. Zhou, A. Tannous, M. Louie, K. T. Leung, Solid State Comm. 125 (2003) 365.

[53] D. K. Sarkar, X. J. Zhou, A. Tannous, K. T. Leung, J. Phys. Chem. B 107 (2003) 2879.

[54] S. C. Tang, X. K. Meng, S. Vongehr, Electrochem. Comm. 11 (2009) 867.

[55] C. Li, K. L. Shuford, Q.-H. Park, W. Cai, Y. Li, E. J. Lee, S. O. Cho, Angew. Chem. Int. Ed. 46 (2007) 3264.

[56] M. R. Khelladi, L. Mentar, A. Azizi, A. Sahari, A. Kahoul, Mater. Chem. Phys. 115 (2009) 385

[57] W. Shao, G. Pattanaik, G. Zangari, J. Electrochem. Soc. 154 (2007) D339.

[58] A. Radisic, A. C. West, P. C. Searson, J. Electrochem. Soc. 149 (2002) C94.

[59] C. Ji, G. Oskam, P. C. Searson, J. Electrochem. Soc. 148 (2001) C746.

[60] W. Ko, W. Chen, S. Tzeng, S. Gwo, K. Lin, Chem. Mater. 18 (2006) 6097.

[61] I. Lisiecki, J. Phys. Chem. B 109 (2005) 12231.

[62] G. Attard, C. Barnes, "Surfaces", Oxford University Press, Oxford 1998.

[63] J. F. Watts and J. Wolstenholme, An Introduction to Surface Analysis by XPS and AES, John Wiley & Sons Ltd, Chichester, 2003.

[64] G. A. Somorjai, "Introduction to Surface Chemistry and Analysis", John Wiley & Sons Ltd, New York, 1994.

[65] D. Briggs, M. P. Seah, "Practical Surface Analysis", volume 1, 2nd Edition, John Wiley & Sons Ltd, Chichester, 1990.

[66] J. Goldstein, D. Newbury, P. Echlin, D. Joy, C. Fiori, E. Lifshin, "Scanning Electron Microscopy and X-Ray Microanalysis", Plenum Press, New York, 1981.

[67] G. Stout, L. Jensen, "X-ray Structure Determination", 2nd edition Wiley & Sons Ltd, Chichester, 1989.

[68] X. J. Zhou, Q. Li, K. T. Leung, J. Phys. Chem. B 110 (2006) 5602.

[69] M. Ebrahimi, J. F. Rios, K. T. Leung, J. Phys. Chem. C 113 (2009) 281.

[70] Q. Li, T. Leung, Surf. Sci. 479 (2001) 69.

[71] C. C. Cheng, J. T. Yates Jr., Phys. Rev. B 43 (1991) 4041.

[72] X. J. Zhou, A. Harmer, N. Heinig, K. T. Leung, Langmuir 20 (2004) 5109.

[73] W. Kohn, L. J. Sham, Phys. Rev. 140 (1965) A1133.

[74] M. J. Frisch, G. W. Trucks, H. B. Schlegel, G. E. Scuseria, M. A. Robb, J. R. Cheeseman, J. A. Montgomery Jr., T. Vreven, K. N. Kudin, J. C. Burant, J. M. Millam, S. S. Iyengar, J.

Tomasi, V. Barone, B. Mennucci, M. Cossi, G. Scalmani, N. Rega, G. A. Petersson, H. Nakatsuji, M. Hada, M. Ehara, K. Toyota, R. Fukuda, J. Hasegawa, M. Ishida, T. Nakajima, Y. Honda, O. Kitao, H. Nakai, M. Klene, X. Li, J. E. Knox, H. P. Hratchian, J. B. Cross, V. Bakken, C. Adamo, J. Jaramillo, R. Gomperts, R. E. Stratmann, O. Yazyev, A. J. Austin, R. Cammi, C. Pomelli, J. W. Ochterski, P. Y. Ayala, K. Morokuma, G. A. Voth, P. Salvador, J. J. Dannenberg, V. G. Zakrzewski, S. Dapprich, A. D. Daniels, M. C. Strain, O. Farkas, D. K. Malick, A. D. Rabuck, K. Raghavachari, J. B. Foresman, J. V. Ortiz, Q. Cui, A. G. Baboul, S. Clifford, J. Cioslowski, B. B, Stefanov, G. Liu, A. Liashenko, P. Piskorz, I. Komaromi, R. L. Martin, D. J. Fox, T. Keith, M. A. Al-Laham, C. Y. Peng, A. Nanayakkara, M. Challacombe, P. M. W. Gill, B. Johnson, W. Chen, M. W. Wong, C. Gonzalez, J. A. Pople, Gaussian 03, Gaussian, Inc., Wallingford, CT, 2005.

[75] A. D. Becke, J. Chem. Phys. 98 (1993) 5648.

[76] C. Lee, W. Yang, R. G. Parr, Phys. Rev. B 37 (1988) 785.

[77] V. Krishnamurthy, I. L. Kamel, Polym. Chem. 27 (1989) 1211.

[78] X. J. Zhou, K. T. Leung, Surf. Sci. 600 (2006) 468.

[79] P. Prayongpan, C. Greenlief, Surf. Sci. 603 (2009) 1055.

[80] R. Felici, I. Robinson, C. Ottaviani, P. Imperatori, P. Eng and P. Perfetti, Surf. Sci. 375 (1997) 55.

[81] X. Lu, X. Xu, N. Wang, Q. Zhang and M. Lin, J. Phys. Chem. B 105 (2001) 10069.

[82] C. Mui, M. Filler, S. Bent, C. Musgrave, J. Phys. Chem. B 107 (2003) 12256.

[83] H. Santos, M. Ramos, J. Ferreira Gomes, C. R. Chimie 8 (2005) 1461.

[84] M. Ebrahimi, K.T. Leung, Surf. Sci. 603 (2009) 1203.

Chapter 2

[1] S. Bent, J. Phys. Chem. B 106 (2006) 2830.

[2] X. Wang, R. Zhang, T. Niehaus, T. Frauenheim, J. Phys. Chem. C 111 (2007) 2394.

[3] J. Yoshinobu, Prog. Surf. Sci. 77 (2004) 37.

[4] J. Li, Y. Qu, K. Han, G. He, Surf. Sci. 586 (2005) 45.

[5] C. Duke, Chem. Rev. 96 (1996) 1237.

[6] N. Sheppard, Ann. Rev. Phys. Chem. 39 (1988) 589.

[7] S. Barlow, R. Raval, Surf. Sci. Rep. 50 (2003) 201.

[8] Z. Ma, F. Zaera, Surf. Sci. Rep. 61 (2006) 229.

[9] J. Zhu, M. Yudasaka, M. Zhang, D. Kasuya, S. Iijima, Nano. Lett. 3 (2003) 9.

[10] M. Voue, E. Goormaghtigh, F. Homble, J. Marchand-Brynaert, J. Conti, S. Devouge, J. De Coninck, Langmuir 23 (2007) 949.

[11] O. Veiseh, C. Sun, J. Gunn, N. Kohler, P. Gabikian, D. Lee, N. Bhattarai, R. Ellenbogen, R. Sze, A. Hallahan, J. Olson, M. Zhang, Nano. Lett. 5 (2005) 6.

[12] H. Haick, D. Cahen, Acc. Chem. Res. 41 (2008) 359.

[13] X. J. Zhou, Q. Li, Z. H. He, X. Yang, K. T. Leung, Surf. Sci. 543 (2003) L668.

[14] X. J. Zhou, K. T. Leung, Surf. Sci. 600 (2006) 468.

[15] M. Ebrahimi, K. T. Leung, Surf. Sci. 603 (2009) 1203.

[16] M. Ebrahimi, J. M. Chong, K.T. Leung, (2009) submitted.

[17] T. Yamada, Curr. Appl. Phys. 6S1 (2006) 26.

[18] V. Krishnamurthy, I. L. Kamel, Polym. Chem. 27 (1989) 1211.

[19] M. Lejeune, F. Brétagnol, G. Ceccone, P. Colpo, F. Rossi, Surf. Coat. Technol. 200 (2006) 5902..

[20] A. Harsch, J. Calderon, R.B. Timmons, G.W. Gross, J. Neurosci. Methods 98 (2000) 135.

[21] G. Chen, W. Zhao, S. Chen, M Zhou, W. Feng, W. Gu and S Yang, Appl. Phys. Lett 89 (2006) 121501.

[22] Z. Zhang, W. Knoll, R. Forch, Surf. Coat. Technol. 200 (2005) 993.

[23] Q. Chen, R. Forch, W. Knoll, Chem. Mater. 16 (2004) 614.

[24] A. L. Hook, H. Thissen, J. Quinton, N. H. Voelcker, Surf. Sci. 602 (2008) 1883.

[25] NIST Mass Spec Data Center, S.E. Stein (director), "Mass Spectra" in NIST Chemistry WebBook, NIST Standard Reference Database Number 69, edited by P.J. Linstrom and W.G. Mallard, June 2005, National Institute of Standards and Technology, Gaithersburg (http://webbook.nist.gov).

[26] J. M. El Khoury, D. Caruntu, C. J. O' Connor, K. Jeong, S. Z. D. Cheng, J. Hu, J. Nanopart. Res. 9 (2007) 959.

[27] M. Morra, C. Cassinelli, A. Carpi, R. Giardino, M. Fini, Biomed. Pharm. 60 (2006) 365.

[28] J. D. Whittle, R. D. Short, C. W. I. Douglas, J. Davies, Chem. Mater. 12 (2000) 2664.

[29] L. Tang, Y. Wu , R. Timmons , J. Biomed. Mater. Res. 42 (1998) 156.

[30] M. Tatoulian, F. Brétagnol, F. Arefi-Khonsari, J. Amouroux, O. Bouloussa, F. Rondelez, A. John Paul, R. Mitchell, Plasma Processes Polym. 2 (2004) 38.

[31] J. Warner, A. Hoshino, K. Yamamoto, R. Tilly, Angew. Chem. Int. Ed. 44 (2005) 4550.

[32] P. Prayongpan, C. Greenlief, Surf. Sci. 603 (2009) 1055.

[33] R. Felici, I. Robinson, C. Ottaviani, P. Imperatori, P. Eng, P. Perfetti, Surf. Sci. 375 (1997) 55.

[34] H. Santos, M. Ramos, J. Ferreira Gomes, C. R. Chimie 8 (2005) 1461.

[35] J. B. Wu, Y. Yang, Y. F. Lin, H. T. Chiu, J. Phys. Chem. B 108 (2004) 1677.

[36] X. Cao, R. Hamers, J. Phys. Chem. B. 106 (2002) 1840.

[37] E. K. Hlil, L. Kubler, J. L. Bischoff, D. Bolmont, Phys. Rev. B 35 (1987) 5913.

[38] X. Cao, R. Hamers, J. Am. Chem. Soc. 123 (2001) 10988.

[39] Th. Kugler, U. Thibaut, M. Abraham, G. Folkers, W. Gopel, Surf. Sci. 260 (1992) 64.

[40] X. Cao, R. Hamers, J. Vac. Sci. Techol. B 20 (2002) 4.

[41] L. Zhang, A. Chatterjee, M. Ebrahimi, K. T. Leung, J. Chem. Phys 130 (2009) 121103.

[42] M. Ikeda, T. Maruoka, N. Nagashima, Surf. Sci. 416 (1998) 240.

[43] H. Liu, R. J. Hamers, Surf. Sci. 416 (1998) 354.

[44] F. A. Carey, "Organic Chemistry", 3rd Edition, McGraw-Hill, Toronto, 1996.

[45] C. C. Cheng, J. T. Yates Jr., Phys. Rev. B 43 (1991) 4041.

[46] X. J. Zhou, Q. Li, K. T. Leung, J. Phys. Chem. B 110 (2006) 5602.

[47] "Bond Dissociation Energies" by Y.-R. Luo, in CRC Handbook of Chemistry and Physics, 88th Edition (Internet Version 2008), edited by D. R. Lide, CRC Press/Taylor and Francis, Boca Raton.

Chapter 3

[1] S. Carniato, J. Gallet, F. Rochet, G. Dufour, F. Bournel, Phys. Rev. B 76 (2007) 085321.

[2] L. Zhang, A. J. Carmen, S. Casey, J. Phys. Chem. B 107 (2003) 8424.

[3] S. Bent, J. Phys. Chem. B 106 (2006) 2830.

[4] N. Sheppard, Ann. Rev. Phys. Chem. 39 (1988) 589.

[5] S. Barlow, R. Raval, Surf. Sci. Rep. 50 (2003) 201.

[6] Z. Ma, F. Zaera, Surf. Sci. Rep. 61 (2006) 229.

[7] X. Wang, R. Zhang, T. Niehaus, T. Frauenheim, J. Phys. Chem. C 111 (2007) 2394.

[8] Z. Zhu, A. Srivastava, R. M. Osgood Jr, J. Phys. Chem. B 107 (2003) 13939.

[9] J. Yoshinobu, Prog. Surf. Sci. 77 (2004) 37.

[10] J. Li, Y. Qu, K. Han, G. He, Surf. Sci. 586 (2005) 45.

[11] C. Duke, Chem. Rev. 96(4) (1996) 1237.

[12] J. Zhu, M. Yudasaka, M. Zhang, D. Kasuya, S. Iijima, Nano Lett. 3 (2003) 9.

[13] M. Voue, E. Goormaghtigh, F. Homble, J. Marchand-Brynaert, J. Conti, S. Devouge, J. De Coninck, Langmuir 23 (2007) 949.

[14] O. Veiseh, C. Sun, J. Gunn, N. Kohler, P. Gabikian, D. Lee, N. Bhattarai, R. Ellenbogen, R. Sze, A. Hallahan, J. Olson, M. Zhang, Nano Lett. 5 (2005) 6.

[15] H. Haick, D. Cahen, Acc. Chem. Res. 41 (2008) 359.

[16] X. J. Zhou, Q. Li, Z. H. He, X. Yang, K. T. Leung, Surf. Sci. 543 (2003) L668.

[17] X. J. Zhou, K.T. Leung, Surf. Sci. 600 (2006) 468.

[18] M. Ebrahimi, T. Leung, Surf. Sci., 603 (2009) 1203.

[19] M. Ebrahimi, J. M. Chong, K. T. Leung, (2009) submitted.

[20] A. Radi, Ch 2. Master Thesis, University of Waterloo (2009).

[21] NIST Mass Spec Data Center, S.E. Stein (director), "Mass Spectra" in NIST Chemistry WebBook, NIST Standard Reference Database Number 69, edited by P.J. Linstrom and W.G. Mallard, June 2005, National Institute of Standards and Technology, Gaithersburg (http://webbook.nist.gov).

[22] C. Reinemann, R. Stoltenburg, B. Strehlitz, Anal. Chem. 81 (2009) 3973.

[23] J. B. Wu, Y. Yang, Y. F. Lin, H. T. Chiu, J. Phys. Chem. B 108 (2004) 1677.

[24] X. Cao, R. Hamers, J. Phys. Chem. B. 106 (2002) 1840.

[25] E. K. Hlil, L. Kubler, J. L. Bischoff, D. Bolmont, Phys. Rev. B 35 (1987) 5913.

[26] X. Cao, R. Hamers, J. Vac. Sci. Technol. B 20 (2002) 4.

[27] X. Cao, R. Hamers, J. Am. Chem. Soc. 123 (2001) 10988.

[28] Th. Kugler, U. Thibaut, M. Abraham, G. Folkers, W. Gopel, Surf. Sci. 260 (1992) 64.

[29] C. Shannon, A. Campion, Surf. Sci. 227 (1990) 219.

[30] J. Eng Jr., K. Raghavachari, L. M. Struck, Y. J. Chabal, B. E. Bent, G. W. Flynn, S. B. Christman, E. E. Chaban, G. P. Williams, K. Radermacher, S. Mantl, J. Chem. Phys. 106 (1997) 9889.

[31] J. Kim, K. Kim, K. Yong, J. Vac. Sci. Technol A 20 (2002) 1582.

[32] J. W. Kim, M. Carbone, M. Tallarida, J. H. Dil, K. Horn, M. P. Casaletto, R. Flammini, M. N. Piancastelli, Surf. Sci. 559 (2004) 179.

[33] M. P. Casaletto, R. Zanoni, M. Carbone, M. N. Piancastelli, L. Aballe, K. Weiss, K. Horn, Surf. Sci. 505 (2002) 251.

[34] Y. Bu, M. C. Lin, Langmuir 10 (1994) 3621.

[35] Bernard Miller, "Advanced Organic Chemistry: Reactions and Mechanisms", Prentice-Hall, New Jersey, 1998.

[36] L. Zhang, A. Chatterjee, M. Ebrahimi, K. T. Leung, J. Chem. Phys 130 (2009) 121103.

[37] J. L. Armstrong, J. M. White, M. Langell, J. Vac. Sci. Technol. A 16 (1997) 123.

[38] "Bond Dissociation Energies" by Y.-R. Luo, in: D.R. Lide (Ed.), CRC Handbook of Chemistry and Physics, 88th ed. (Internet Version 2008), CRC Press/Taylor and Francis, Boca Raton.

[39] H. Liu, R. J. Hamers, Surf. Sci. 416 (1998) 354.

[40] J. S. Hovis, R. J. Hamers, J. Phys. Chem. B 101 (1997) 9581.

[41] C. C. Cheng, J. T. Yates Jr., Phys. Rev. B 43 (1991) 4041.

[42] M. Ebrahimi, J. F. Rios, K. T. Leung, J. Phys. Chem. C 113 (2009) 281.

Chapter 4

[1] H. Nakatsuji, Z. Hu, Int. J. Quant. Chem. 77 (2000) 341.

[2] J. Iijima, J. Lim, S. Hong, S. Suzuki, K. Mimura, M. Issiki, Appl. Surf. Sci 253 (2006) 2825.

[3] J. Lee, J. Choi, S. Kang, J. Lee, Y. Tak, J. Lee, Electrochim. Acta 52 (2007) 2272.

[4] K. Akimoto, S. Ishizuka, M. Yanagita, Y. Nawa, G. Paul, T. Sakurai, Sol. Energy 80 (2006) 715.

[5] J. Tamaki, K. Shimanoe, Y. Yamada, Y. Yamamoto, N. Miura, N. Yamazoe, Sensor Actuators, B 49 (1998) 121.

[6] X. Miao, R. Yuan, Y. Chai, Y. Shi, Y. Yuan, J. Electroanal. Chem. 612 (2008) 157.

[7] T. Ishihara, M. Higuchi, T. Takagi, M. Ito, H. Nishiguchia, Y. Takitaa, J. Mater. Chem. 8 (1998) 2037.

[8] G. Borkow, R. Sidwell, D. Smee, D. Barnard, J. Morrey, H. Lara-Villegas, Y. Shemer-Avni, J. Gabbay, Antimicrob. Agents Chemother. (2007) 2605.

[9] G. Borkow, H. Lara, C. Covington, A. Nyamathi, J. Gabbay, Antimicrob. Agents Chemother. (2008) 518.

[10] D. Barreca, A. Gasparotto, C. Maccato, E. Tondello, O.I. Lebedev, G. V. Tendeloo, Cryst. Growth Des. 9 (2009) 52470.

[11] Z. Pászti, G. Petö, Z. E. Horváth, A. Karacs, Appl. Surf. Sci. 168 (2000) 114.

[12] C. J. G. van der Grift, A. Mulder, J. W. Geus, Colloids Surf., B 53 (1991) 223.

[13] N. Radwan, M. El-Shall, H. Hassan, Appl. Catal., A 331 (2007) 8.

[14] Y. C. Liu, K. H. Yang, M. D. Ger, Synth. Met. 126 (2002) 337.

[15] M. R. Guascito, P. Boffi, C. Malitesta, L. Sabbatini, P. G. Zambonin, Mater. Chem. Phys. 44 (1996) 17.

[16] N. Cioffi, L. Torsi, I. Losito, C. D. Franco, I. D. Bari, L. Chiavarone, G. Scamarcio, V. Tsakova, L. Sabbatini, P. Zambonin, J. Mater. Chem. 11 (2001) 1434.

[17] Z. Pászti, G. Petö, Z. E. Horváth, A. Karacs, J. Phys. Chem. B 101 (1997) 2109.

[18] L. Makhloufi, H. Hammache, B. Saidani, N. Akilal, Y. Maloum, J. Appl. Electrochem. 30 (2000) 1143.

[19] V. Tsakova, D. Borissov, B. Ranguelov, C. Stromberg, J.W. Schultze, Electrochim. Acta 46 (2001) 4213.

[20] V. Tsakova, D. Borissov, Electrochem. Comm. 2 (2000) 511.

[21] C. Ji, G. Oskam, P.C. Searson, Surf. Sci. 492 (2001) 115.

[22] D. K. Sarkar, X. J. Zhou, A. Tannous, M. Louie, K. T. Leung, Solid State Comm. 125 (2003) 365.

[23] D. K. Sarkar, X. J. Zhou, A. Tannous, K. T. Leung, J. Phys. Chem. B 107 (2003) 2879.

[24] S. C. Tang, X. K. Meng, S. Vongehr, Electrochem. Comm. 11 (2009) 867.

[25] C. Li, K. L. Shuford, Q.-H. Park, W. Cai, Y. Li, E. J. Lee, S. O. Cho, Angew. Chem. Int. Ed. 46 (2007) 3264.

[26] M. R. Khelladi, L. Mentar, A. Azizi, A. Sahari, A. Kahoul, Mater. Chem. Phys. 115 (2009) 385

[27] W. Shao, G. Pattanaik, G. Zangari, J. Electrochem. Soc. 154 (2007) D339.

[28] A. Radisic, A. C. West, P. C. Searson, J. Electrochem. Soc. 149 (2002) C94.

[29] C. Ji, G. Oskam, P. C. Searson, J. Electrochem. Soc. 148 (2001) C746.

[30] D. Feldheim, C. Foss, "Metal Nanoparticles, Synthesis, Characteristics and Applications", New York, Marcel Dekker, 2002.

[31] G. Oskam, J. Long, A. Natarajan, P. Searson, J. Phys. D 31 (1998) 1927.

[32] D. Grujcic, B. Pesic, Electrochim. Acta, 47 (2002) 2901.

[33] A. Singh, K. Luening, S. Brennan, T. Homma, N. Kubo, P. Pianetta, Phys. Scripta. 115 (2005) 714.

[34] W. Ko, W. Chen, S. Tzeng, S. Gwo, K. Lin, Chem. Mater. 18 (2006) 6097.

[35] X. J. Zhou, A. Harmer, N. Heinig, K. T. Leung, Langmuir 20 (2004) 5109.

[36] I. Lisiecki, J. Phys. Chem. B 109 (2005) 12231.

[37] C. Henry, Prog. Surf. Sci. 80 (2005) 92.

[38] PDF-2 Database, International Center for Diffraction Data, (2004).

[39] P. Stefanov T. Marinova, Appl. Surf. Sci. 31 (1988) 445.

[40] G. Panzner, B. Egert, H. Schmidt, Surf. Sci. 151 (1985) 400.

[41] B. Balamurugan, B. R. Mehta, S. M. Shivaprasad, Appl. Phys. Lett. 79 (2001) 19.

[42] Sung, M. M.; Sung, K.; Kim, C. G.; Sun S. Lee, S. S.; Kim, Y. J. Phys. Chem. B 2000, 104, 2273.

[43] T. H. Fleisch, G. J. Mains, J. Appl. Surf. Sci. 1982, 10, 51.

[44] J. Ghisen, L. H. Jjeng, J. van Elp, H. Eskes, J. Westerink, G. A. Sawatzky, Phys. Rev. B 38 (1988) 11322.

[45] Y. Sohn, D. Pradhan, A. Radi, K. T. Leung, (2009) to be submitted.

[46] I. Suh, H. Ohta, Y. Waseda, J. Mater. Sci 23 (1988) 757.

[47] A. Kirfel, K. Eichhorn, Acta Crystallogr., Sect. B: Struct. Sci A 46 (1990) 271.

[48] G. Celotti, D. Nobili, P. Ostoja, J. Mater. Sci. 9 (1974) 821.

[49] N. J. Calos, J. S. Forrester, G. B. Schaffer, J. Solid State Chem. 122 (1996) 273.